A Seismic Investigation into the Thermal and Physical Properties of the Hydrate Bearing Pukeroro Ridge, Hikurangi Margin, New Zealand

Patrick Fletcher

A thesis submitted for the degree of
Master of Science
GEOPHYSICS
at the University of Otago, Dunedin, New Zealand

March 2018

Abstract

Understanding the subsurface dynamics of the world's oceans has become more important over time due to current climate issues, hazard evaluations and an ever-decreasing abundance of resources. Fluid and heat flow processes operating beneath oceans around the world are some of the most significant processes involved with many of the research sectors focused on studying the ocean floors.

Pukeroro Ridge, located east of the lower North Island of New Zealand, recently has been surveyed a number of times, including by a conventional petroleum industry seismic survey in 2009 and a high-resolution seismic survey combined with a heat flow study in 2015. The variety of data types collected in a structurally complex area affected by dynamic subsurface flow provides us with a unique opportunity to (1) investigate the subsurface dynamics of an extensive gas hydrate accumulation, and also (2) evaluate a number of analytical techniques and processes that can be applied in such settings.

Throughout this thesis, high–resolution and conventional seismic data are compared, and a combination of the data sets is used to better characterise subsurface features across Pukeroro Ridge. The bottom simulating reflections (BSR) identified in the seismic data, in combination with the heat flow results, are used to better understand thermal conductivity variations in the area. Additionally, the effectiveness of using the BSR as an isotherm from which we can estimate heat flow along seismic lines, without heat flow measurements, is evaluated.

The high-resolution data were found to have a 2 - 3 m vertical resolution in the 800 m immediately beneath the subsurface. The data identified fine scale bedding and any discontinuities in the reflections, particularly the BSR. The conventional seismic data had a lower resolution; they were able to image features with a vertical length scale of about 10 m. Discontinuities found in the high-resolution data were not evident in the lower resolution data and reflections appeared more continuous and uniform. In contrast, the lower frequencies of the conventional seismic data allowed for increased penetration, enabling imaging at depths of over 3500 m beneath the seafloor. The high-resolution data lost resolution in some

localised regions; this was determined to be because of the short offsets of the data limiting imaging power in region of dipping strata.

The seismic data identified two main lithological units: a bedded unit and a non-bedded unit, of which the constituents were narrowed down to a siltstone/mudstone of Pliocene – Pleistocene age, based on previous research. The seismic data also identified several reverse faults dipping 40-45°W. A section of localised fluid flow was identified based on an amplitude reversal, which is consistent with an appropriate geological interpretation of the feature. Beneath this reversal, a strong BSR was identified which became an integral part of further research.

The method of estimating the thermal conductivity in the subsurface based on using the BSR as an isotherm was deemed to be sufficiently accurate. The results were reasonable based on the lithological units identified. The method highlighted an increase in thermal conductivity associated with increasing pressure as a result of depth. This increase was greater than what would be expected as a result of purely hydrostatic pressure. Thermal conductivities spiked up to 2.1 W/m/K in concurrence with heat flow anomalies, of up to 56 mW/m^2. These highs also coincided with the fluid flow features previously identified during the seismic interpretations. The thermal conductivities also suggest regional fluid migration.

Finally, although the evaluation of the heat flow estimation method was partially successful, it also highlighted several methodological issues. The method appeared effective for stable continuous areas with widespread, uniform lithological units and minimal fluid movement. The method also required a reasonable understanding of the thermal conductivities in the region. The testing highlighted several scenarios where the estimations had a higher level of uncertainty, such as those with localised fluid features or areas with poorly constrained thermal conductivities.

Overall, the research made effective use of the substantial quantity and variability of data available in this unique locality. While the findings allowed for important correlations and a greater understanding, they would benefit from further research, including drilling, which would enable calibration of the thermal conductivity measurements. More heat flow transects would also allow for comparison and investigations into the accuracy of the heat flow estimations undertaken.

Table of Contents

List of Tables

1 Introduction

1.1 Outline

Heat flow is the transfer of heat from the Earth's interior to the surface. This transfer of heat is controlled and influenced by a number of geological properties and as a result there are significant trends and variations across the Earth's surface that can influence the near surface geology (Beardsmore and Cull, 2001; Vedova et al., 2001).

In June 2015, the RV Roger Revelle undertook a research cruise (RR1508) focused on taking heat flow measurements across several transects throughout the central part of the Hikurangi Margin, off the East Coast of New Zealand. As well as 164 heat flow measurements, seismic reflection profiles were acquired along and parallel to the heat flow transects to image the subsurface geology. The seismic data allowed for further interpretation of the region, including the determination of the depth of the bottom simulating reflections (BSRs), which help to characterise the distribution of gas hydrates on the margin.

This thesis focuses on three heat flow deployments that combine to make up a single heat flow transect taken across Pukeroro Ridge. The heat flow transect, containing 34 individual heat probe measurements, was accompanied by five high-resolution seismic lines collected during the same cruise and an additional conventional (industry style) seismic line collected during the earlier PEG09 survey. Using the seismic and heat flow data, along with previous research into the geology of the region and its tectonic regime, several questions have been developed which are addressed in this thesis.

- What are the thermal characteristics of Pukeroro Ridge and how do they vary in the subsurface?
- How is heat flow affected by geological constraints?
    - Do focused fluid flow and varying lithologies affect heat flow?
    - Can modelling be undertaken to relate features to heat flow observations?
- How does heat flow vary in the vicinity of Pukeroro Ridge?
    - Can a scheme be developed to extrapolate the data from heat flow Transect 9 to the surrounding region, making use of the seismic data and interpretations of BSR depth and amplitude characteristics?
- What are the relative merits of high-resolution seismic data and conventional seismic data for studying gas hydrates and associated heat flow?

In this thesis, the unusual occurrence of having high-resolution and conventional seismic data overlapping is used to compare and contrast the two survey types and the corresponding results.

The idea of using the depth of the BSR below the seafloor to estimate temperature gradients in the subsurface is also investigated (Townend, 1997). These estimates, combined with assumptions regarding associated pressures, salinity and gas composition, enable the determination of heat flow. This method also allows for the estimation of heat flow based on purely seismic data with visible BSRs (e.g., Priyanto et al., 2015).

Measurements of heat flow at the surface, as well as BSR-derived thermal gradients, enable investigations of thermal conductivity variations of the subsurface. These variations can be used in combination with the seismic data to try to understand specific subsurface features and shallow fluid migrations.

1.2 Basic Principles of Heat Flow

The Earth, since the formation of our solar system, has been a reservoir of a large amount of energy (heat) resulting from collisions between the growing proto-planet and incoming mass. This energy is combined with heat energy from the radioactive decay of ^{238}U, ^{235}U, ^{232}Th and ^{40}K in the Earth itself (Masters and Constable, 2017). The energy is slowly released from the Earth's surface over time. Heat flow is a measurement of the amount of energy being released as heat at the Earth's surface per unit of time (Stein, 1995).

Due to convection and radiogenic sources of heat, heat flow varies considerably across the Earth. The average heat flow for the continental crust is 65 mW/m^2 compared with a considerably higher 101 mW/m^2 for oceanic crust (Figure 1.1) (Pollack et al., 1993). The difference in heat flow emitted from the different crusts is largely related to crustal thickness. The continental crust is much thicker, acting as a better insulator and keeping the mantle further from the surface. The thinner oceanic crust results in the mantle being closer to the surface and as a result it has a greater heat flow. This can seem counter intuitive due to the higher concentrations of uranium, thorium and potassium present in the granitic continental crust, but the insulation effect outweighs the increased concentration in radioactive materials (Stein, 1995).

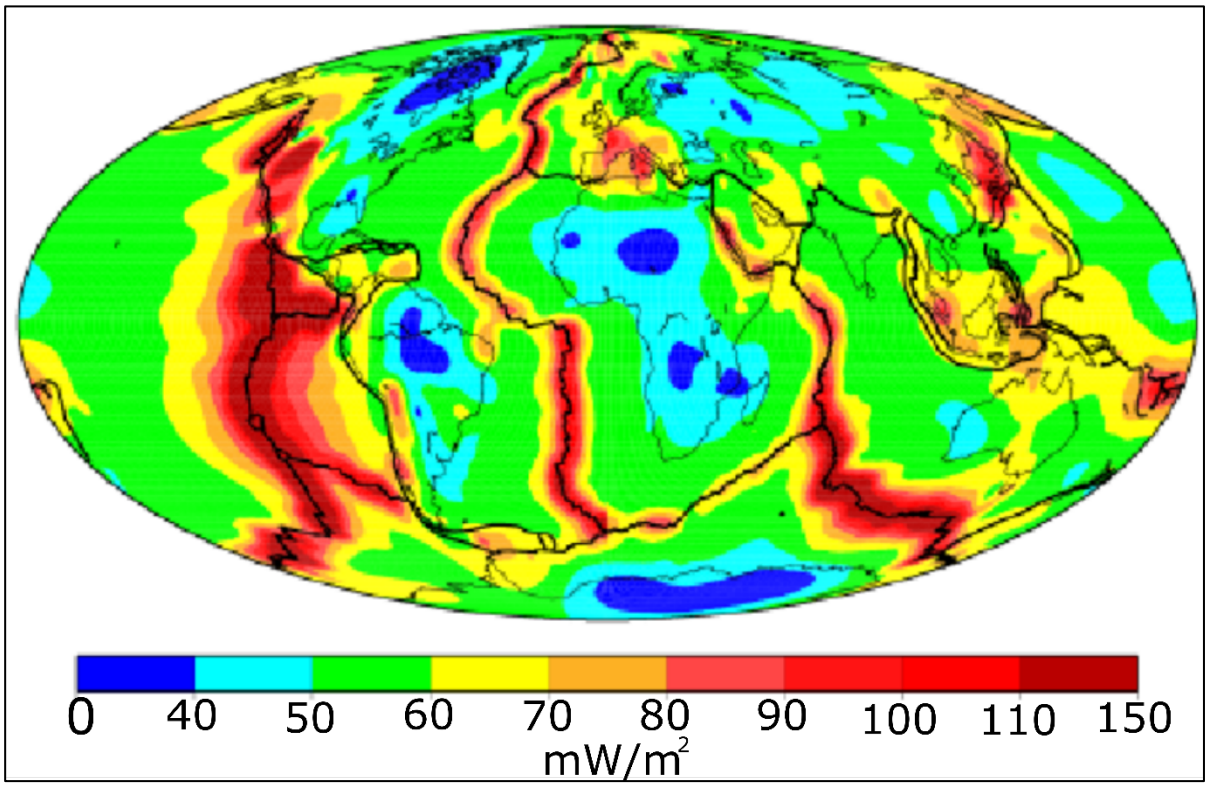

Figure 1.1 *Map showing distribution of heat flow across the globe. From* (Roberto R. Cardoso and Valiya M. Hamza, 2011).

The transfer of heat from the Earth to the atmosphere can occur via three methods of transmission: radiation, convection and conduction. Convection requires the medium to be able to flow, so despite convection being the most efficient method of heat transfer, conduction is the most significant method of heat transmission through the brittle lithosphere to the surface (Masters and Constable, 2017).

Conduction is described by Equation 1.1

$$Q = -K\nabla T \tag{1.1}$$

Where Q = heat flow, K = thermal conductivity, $\nabla = \frac{\partial}{\partial x}, \frac{\partial}{\partial y}, \frac{\partial}{\partial z}$ and T = temperature.

Heat flow measurements on the surface of the Earth can be taken by inserting probes several metres beneath the surface to measure and record temperatures at a range of depths. The temperatures are recorded for the initial insertion, and

the resulting temperature decay following frictional heating is recorded prior to heating. From these measurements background temperature gradients, as well as the rate of cooling, can be calculated. With these calculated temperature gradients and rate of cooling, the heat flow of the location can be calculated in milliwatts per metre squared (mW/m^2) (Bonneville, 2017).

Heat flow, Q, is measured as the product of temperature gradients, T, (°C per km) and thermal conductivity, K, (W/m /K), ($Q = T \bullet K$) (Sass and Beardsmore, 2011). The temperature gradient is the rate of change of the temperature over a distance. The temperature gradient is derived from at least two spot temperature measurements with the difference being divided by the distance to calculate the gradient. The assumption is also made that heat flow is purely vertical. K can be determined in situ; however, more commonly K is a laboratory derived number. With these two values, the heat flow of the location can be calculated (Adkins, 1987).

Heat flow across the surface of tectonic plates is highly variable and is controlled by a number of geological properties including tectonic and crustal characteristics. In oceanic crust, heat flow is greatest near the mid ocean ridges and decreases with distance from these ridges. It is this variation in heat flow that represents a major part of terrestrial convection (Stein, 1995). Heat flow through oceanic crust is also affected by sediment accumulation; areas with high sediment accumulation have decreased heat flow due to hydrothermal circulation (Sclater et al., 1980). Heat flow through continental crust decreases with distance from the plate boundaries due to the crust thickening towards the centre of the plate (Cardoso and Hamza, 2011).

Heat flow is an important focus for research due to the large quantity of energy released. Heat flow energy, for example, is many times larger than energy released by tidal fluxes, seismic energy released by earthquakes and the Earth's magnetic field (Pollack et al., 1993). The amount of energy released has a significant impact on the geological characteristics of the Earth's surface, particularly through controlling pressure and temperature conditions. These conditions control rock and fluid properties, gas hydrate stability zones, as well as the deformation properties of the lithosphere (Vedova et al., 2001).

1.3 Basic Principles of Seismic Imaging

Seismic imaging is a geophysical method that makes use of changes in seismic impedance through the subsurface, which is defined as the product of P-wave velocity (V_p) and density (ρ) in the medium. Seismic velocity is in turn controlled by the physical properties of the material that the sound is travelling through, see Equation 1.2

$$v_P \sqrt{\frac{K + \left(\frac{4}{3\mu}\right)}{\rho}} \tag{1.2}$$

$v_P = P - wave\ velocity, K = bulk\ modulus, \mu = shear\ modulus, \rho = density$

The technique is used in both terrestrial and oceanic settings to image the subsurface. In marine seismic imaging, air guns are generally used as sound sources. The sources emit sound waves that travel down to the seafloor and the subsurface, then reflect back off changes in impedance (Figure 1.2). These reflections and their amplitude and phase characteristics are recorded by pressure sensors (hydrophones) floating near the sea surface. The reflections are sent back to the computers as electrical pulses where they are digitised, recorded and analysed (Scales, 2017).

During marine seismic data acquisition, the sound source produces compressional or P-waves. These P-waves travel through the surface and reflect when they reach impedance contrasts. Only P-waves are recorded in marine surveys, as shear or S-waves cannot propagate through liquids (Ikelle and Amundsen, 2005).

For reflections to occur there needs to be an impedance contrast and a minimum width of interference. From these reflections; amplitude, phase, polarity, arrival time and velocities can be found (Nanda, 2016). Using these properties an accurate image representing the subsurface can be produced.

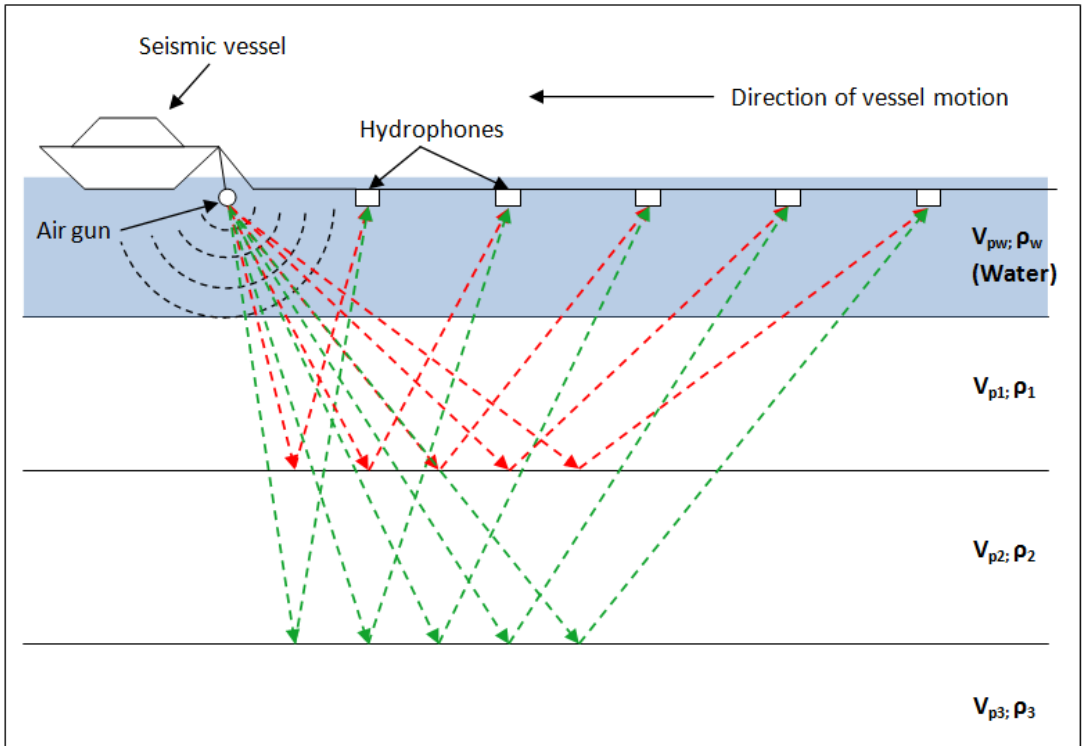

Figure 1.2 *Cartoon showing the travel paths of seismic sound waves down through the water and subsurface during a seismic survey. Vpx = the velocity of the P-wave through the specific unit (Nwhit, 2012).*

When the sound waves intercept a change in impedance at an angle that is not beyond that of the critical angle, a portion of the energy is refracted and passes through the boundary, while another portion is reflected and returned to the surface at the incident angle. As the transmitted soundwaves are now within a solid medium, both S and P, refracted and reflected waves are produced, each at their own angles due to the differing velocities between S and P waves. It is these reflected P-waves that travel from the subsurface up to the geophones where they are recorded (Figure 1.3) (Ikelle and Amundsen, 2005).

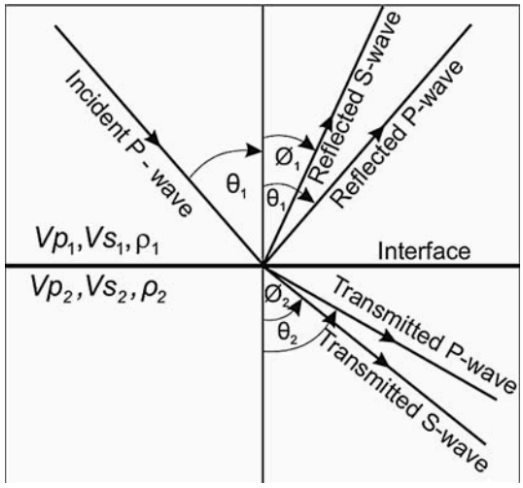

Figure 1.3 *Showing the various seismic responses between seismic waves and across a velocity contrast (Sain, 2011).*

Once these data have been recorded and collated, a series of seismic processing steps are undertaken to filter and refine the data, increase the resolution, correcting artefacts and ultimately trying to produce a realistic image of the subsurface (Figure 1.4).

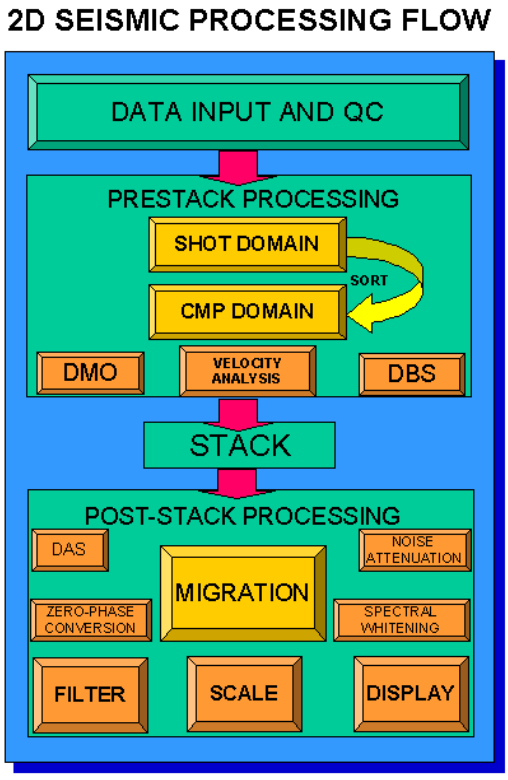

Figure 1.4 *A standardised processing flow showing the main and most common steps involved in processing seismic data (XSGEO, 1999a).*

1.4 Basic Principles of Gas Hydrates

Gas hydrates are naturally occurring solid lattices of water molecules surrounding a single gas molecule which stabilizes the lattice structure (Sloan, 2003). The ratio of solid to gas is on average 160:1 (Hunt, 1979).

Gas hydrates are found in three structure types (I, II, H) (Figure 1.5). The structure formed is controlled by the gas molecule present in the clathrate. Methane (CH_4) results in structure I. If larger hydrocarbon molecules are present, structure II (C_1 - C_4) and structure H (C_1, C_5 – C_8) can be produced. Naturally occurring structure H is rare. There are only two known occurrences which are associated with thermogenic hydrocarbon gas and oil venting/seeping (Riedel et al., 2010).

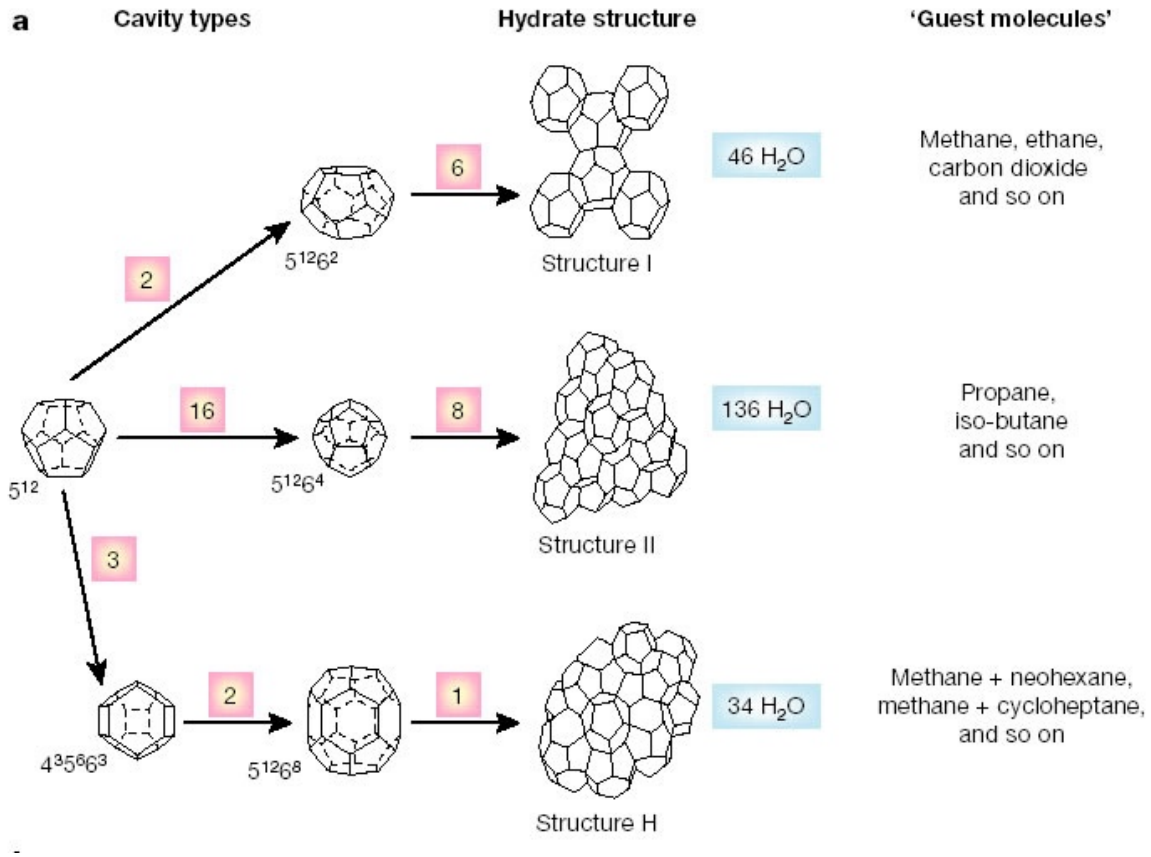

Figure 1.5. *The three different structures of hydrates and their associated gas compositions with their carbon to hydrogen ratios(Sloan, 2003).*

Gas hydrates are found naturally in a very specific set of pressure and temperature conditions, where the geothermal gradient is within the gas hydrate stability zone. Gas hydrates require

low-temperature high-pressure environments as well as a source of methane. These conditions exist naturally in two instances: one in permafrost, the other on continental slopes, generally exceeding 500 m water depth (Figure 1.6 and 1.7) (Kvenvolden, 1993).

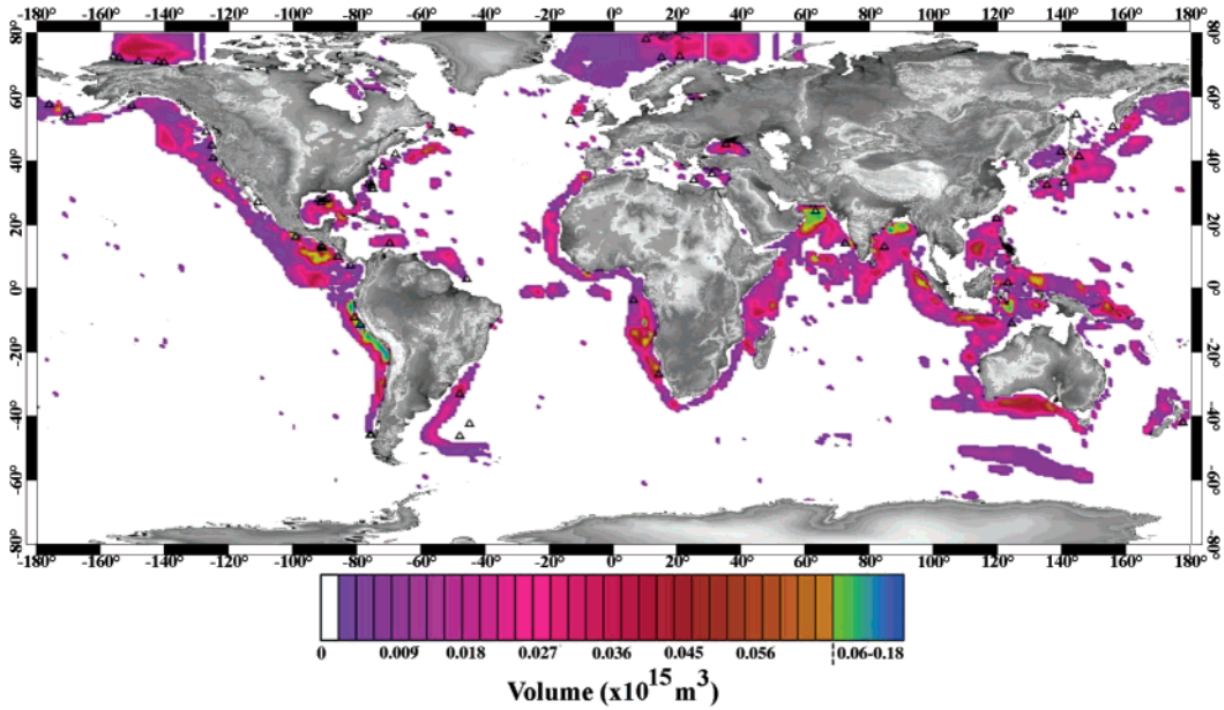

Figure 1.6 *Distribution of gas hydrates across the globe and their associated volumes (Klauda and Sandler, 2005).*

.

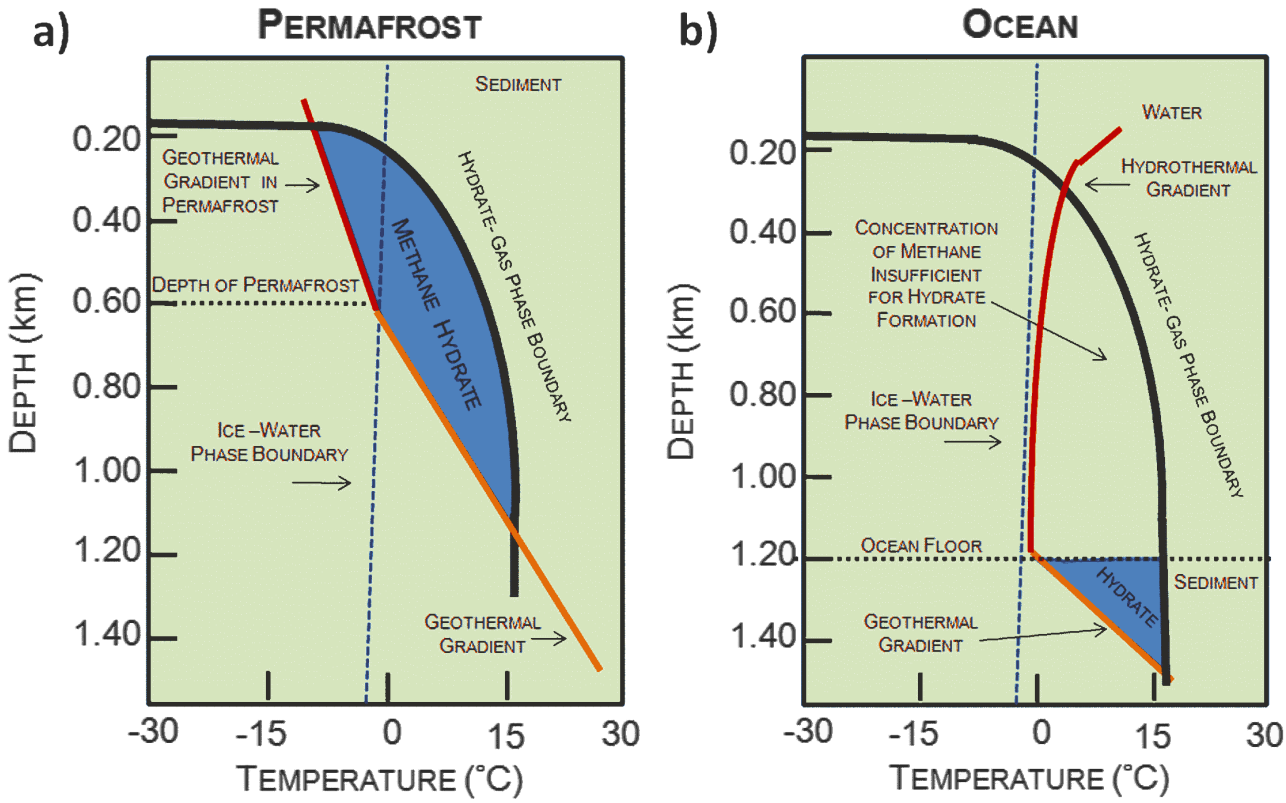

Figure 1.7 *Example gas hydrate stability curves in both permafrost and marine settings with geothermal gradients annotated in red (Harrison, 2010).*

Gas hydrates are an extensive reservoir for methane in terms of the global system, with current estimates suggesting volumes of $10^{14} – 10^{15}$ m^3, an order of magnitude larger than the current estimated oil reserves. This immense methane potential has both climatic and economic implications. The technology to successfully extract gas hydrates as a fuel source has not yet been developed to a level that is both economic and environmentally sustainable, although production tests are advanced in several locations around the world, including offshore Japan and China (Konno et al., 2017). If such techniques were to be successfully developed then gas hydrates might play a very important role as a methane resource in the future. As well as its abundance, methane is also a cleaner fuel to burn (compared to oil and coal) and is the preferred fossil fuel used in the petrochemical industry (Sloan, 2003). These factors together create a real economic opportunity.

Gas hydrate as a methane reservoir also holds significance in climatic studies. Research has shown that changing climatic conditions in the past must have resulted in a disruption of gas hydrate stability fields that would have led to the mass release of methane. This release

would not only contribute to global warming, but it also undermines the structural integrity of continental slopes. Evidence suggests that such events have resulted in major submarine slips. These historic events supports the theory that the current trend of global warming could produce similar events in the future due to mass methane release (Kvenvolden, 1993).

1.5 Geological Setting

The Pegasus Basin is found on the active continental shelf margin off the east coast of the lower North Island and upper South Island of New Zealand. The location is strongly controlled by the tectonic regime of the Hikurangi Margin, with the faults resulting in a range of ridges and valleys across the region. The region is in close proximity to Wellington, the capital city of New Zealand. The presence of gas hydrates is well mapped throughout the region as are the structural features associated with the subduction zone and marginal accretion.

The Hikurangi Margin is where the eastern extent of the continental crust of Zealandia meets the subducting Pacific Plate. The margin is made up of thrusted imbricated frontal wedges adjacent to a backstop of Mesozoic Torlesse Terrane greywackes (Crutchley et al., 2015).

The majority of fluid flow is presumed to occur along the thrust faults of this region. The flow is mostly found in the outer regions of the accretionary margin and the basal decollement of the trench. These regions fill with fluid sourced from the compression of subducted and accreted sediments and smectite dehydration (Kroeger et al., 2015).

The wedge has been separated into three components (Barnes et al., 2010): 1. Late Cretaceous and Paleogene rocks preceding the formation of the Hikurangi subduction zone, 2. an accumulation of late Cenozoic trench fill turbidites, and 3. an overlying sequence of Miocene to recent depositional sediments.

The sediment supply for the region originates from the fluvial outputs at the top of the South Island which are transported northward by longshore drift to the vicinity of the Kaikoura Canyon (Lewis and Pantin, 2002). The sediment is predominantly clastic, ranging from mud to sand in size. These organic-rich clastic sediments are broken down and used in the

microbial production of hydrocarbons which feed the reservoirs in the region (Kroeger et al., 2015).

The Pacific Plate subducts beneath the Australian Plate at a gentle dip of roughly 4°. The plates meet at an oblique angle, at a rate varying between 41 and 45 mm/yr, decreasing southward along the margin (Baker, 2016).

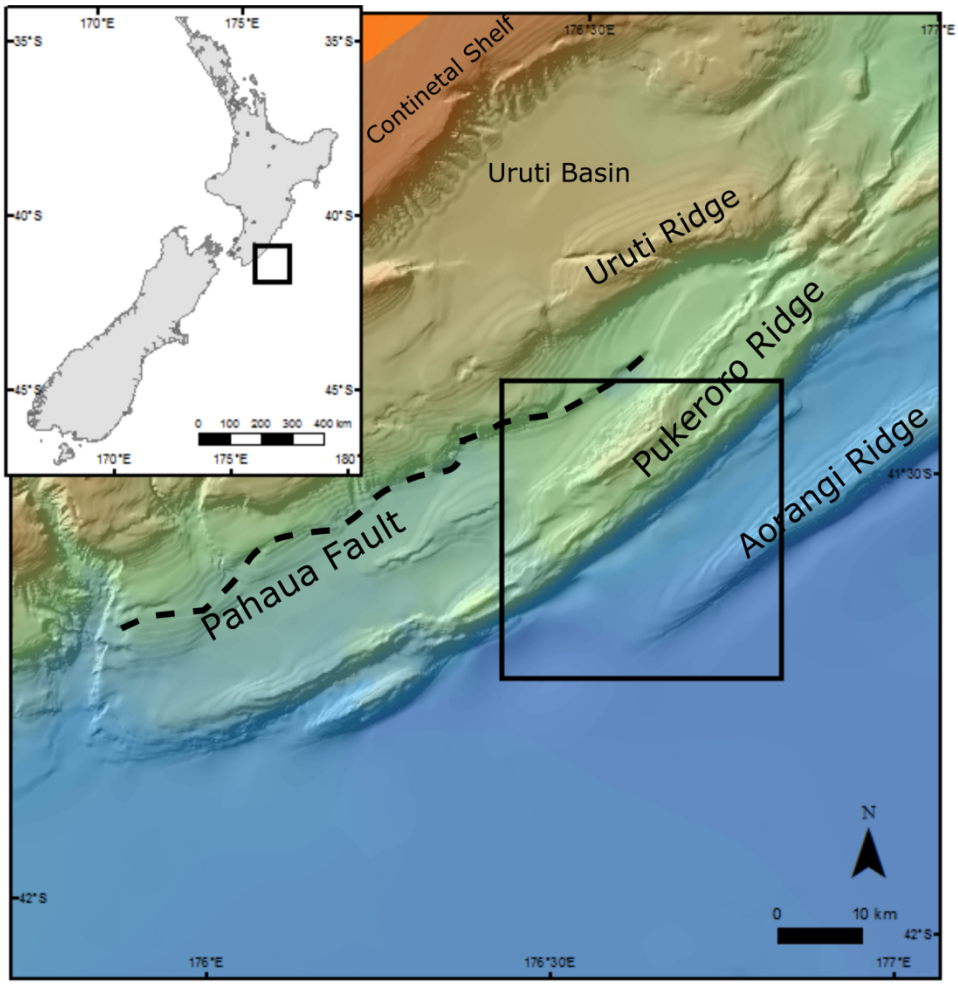

Figure 1.8 Locality map of showing Pukeroro Ridge and the surrounding geologic and bathymetric features.

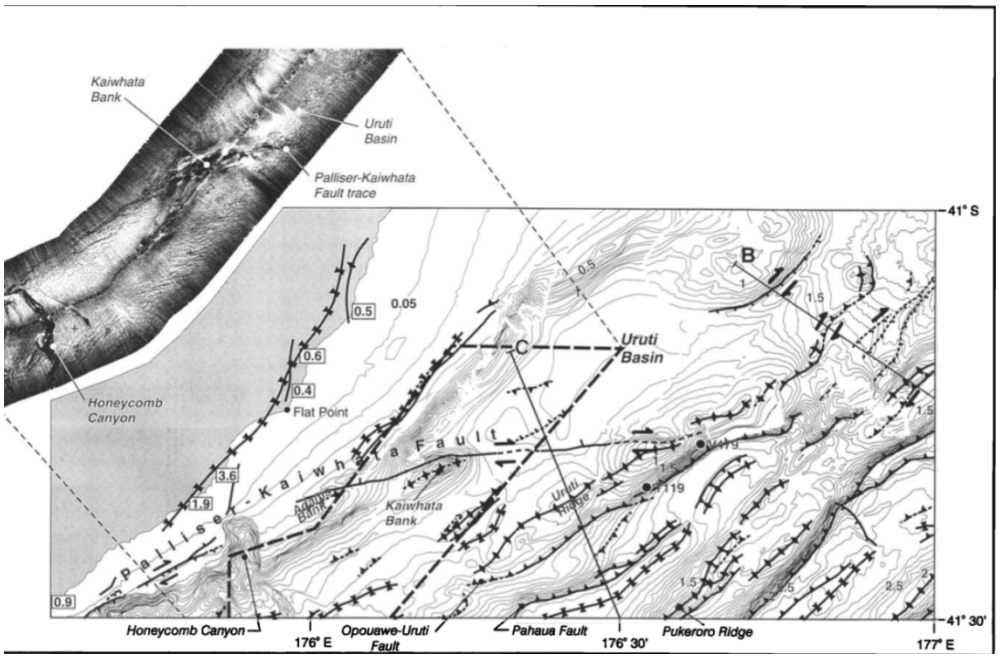

Figure 1.9 A map of all the known and significant faults surrounding the Pukeroro Ridge locality (Barnes et al., 1998).

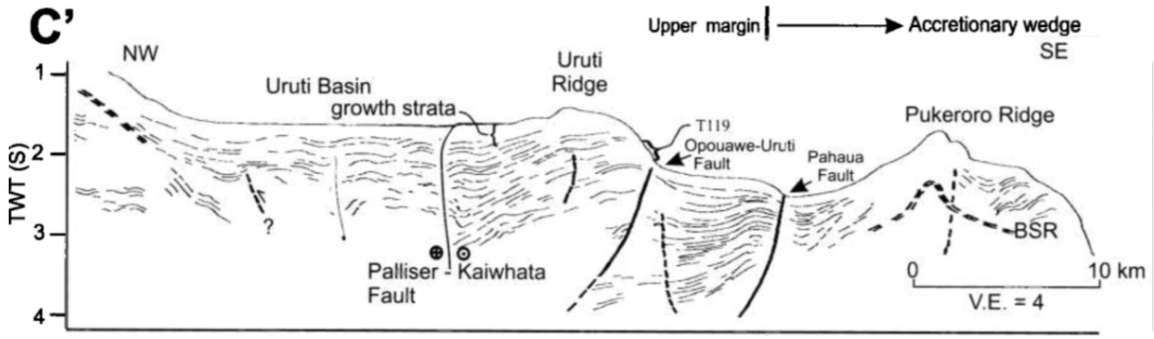

Figure 1.10 A cartoon cross section running along the transect marked as C in Figure 1.8. The cross-section highlights the structural features beneath Pukeroro Ridge (Barnes et al., 1998)

This research is focused along the southwestern portion of Pukeroro Ridge, located in the northern regions of the Pegasus Basin at roughly 41°33'S, 176°31'E, with water depths between 1500 and 2000 mbsl (Figure 1.11) (Crutchley et al., 2015). The ridge has formed through deformation of the frontal accretionary wedge produced by the Hikurangi subduction zone. The area is in the vicinity of the Pahaua Fault which lies to the north-east of Pukeroro

Ridge (Figure 1.11 and 1.9). As well as the major Pahaua Fault, the locality also contains a large number of anticlinal ridges cored by blind thrusts that can be imaged with the seismic data (Barnes et al., 2010).

The highly-faulted nature of the seafloor causes variability in fluid flow and gas hydrate stability which affects the overall heat flow of the region.

Figure 1.11 Locality map of showing Pukeroro Ridge and the surrounding geologic and bathymetric features.

1.6 Gas Hydrates in the Hikurangi Margin

Gas hydrates in the Hikurangi Margin extend over a 50,000 km^2 area and are contained within buried channel systems and permeable layers that stretch from the gas hydrate stability field, or possibly on the edges of gas chimneys (Baker, 2016; Crutchley et al, 2015; Fohrmann and Pecher, 2012; Fraser, 2017). Approximately 10% of the Hikurangi Margin is suggested to contain gas hydrate, equating to 20,000 km^3 of gas based on an average 2% pore saturation (Fohrmann and Pecher, 2012)

The base of gas hydrate saturated sediments often produces a BSR (bottom simulating reflection) in seismic data. At the base of gas hydrate stability, there exists a change in impedance, resulting from the phase boundary between gas hydrate and methane gas found within the pore space of sedimentary units (Chi et al., 1998). The BSR typically mirrors the shape of the seafloor due to its depth being controlled by temperature and pressure (*Figure 1.12*). This BSR is often imaged in seismic data (Andreassen et al., 1995). The BSR seen in the RR1508 data is used to estimate the heat flow where no heat flow data were collected.

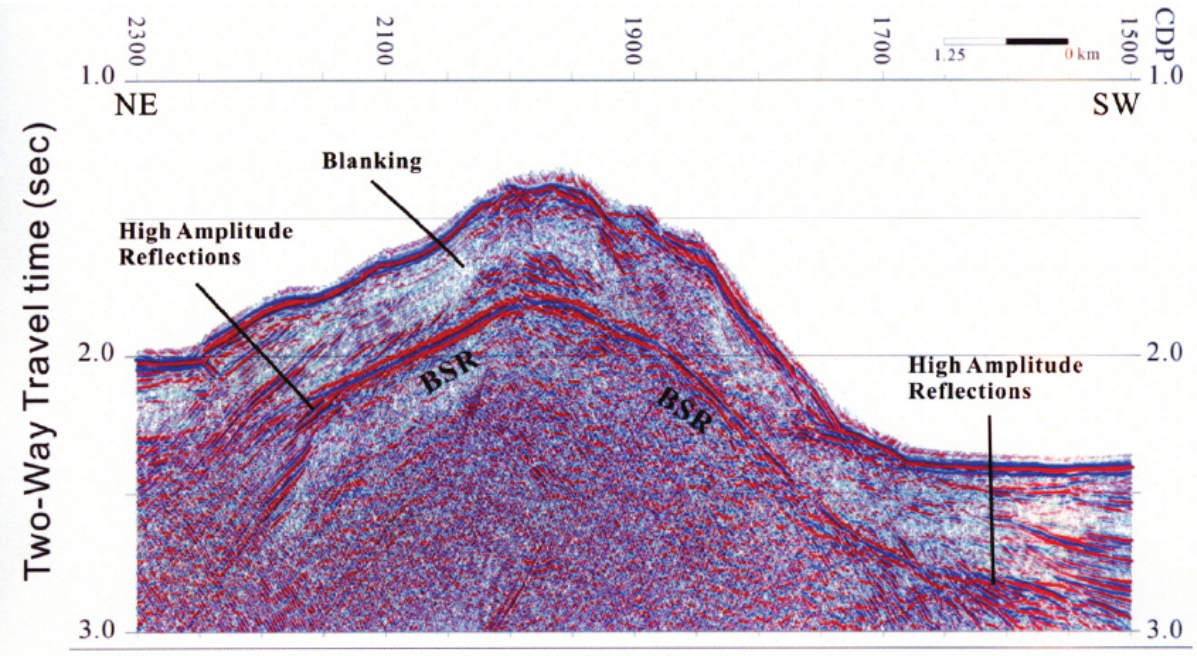

Figure 1.12 An example of seismic data with the BSR annotated as well as blanking associated with the gas hydrate zone of stability (Liu et al., 2006)

1.7 Thesis Outline

In this thesis, a combination of heat flow and seismic data is used to try to understand the thermal and physical properties of the subsurface beneath Pukeroro Ridge. The differences between the two seismic data sets are examined, and the effectiveness of the BSR as a proxy for heat flow is evaluated.

Chapter 2 presents the seismic and heat flow data sets that are used in this thesis. The chapter discusses the collection methods used to obtain the data as well as the processing and data manipulation techniques used to refine and analyse the data sets. Errors are also discussed and quantified throughout this chapter.

Chapter 3 compares and contrasts the RR1508 and PEG09 data sets. The similarities and differences between the high-resolution RR1508 seismic data and the conventional PEG09 data are discussed. These differences help to highlight the advantages and disadvantages of the different survey types as well as identifying their specific uses.

Chapter 4 covers the seismic interpretations that have been made using the RR1508 seismic data. The chapter presents the relative positioning of the reflections, their amplitudes and velocities determined from the seismic data. These observations are then discussed in terms

of the features or processes they represent, including lithology determinations, zones of gas hydrate accumulation, fluid features and faulting.

Chapter 5 covers the observations and interpretations made based on the results originating from the heat flow calculations. These are combined with measured and calculated geothermal gradients. The data give an insight into the calculated thermal conductivity of the subsurface and what it can tell us about sedimentary lithologies and fluid dynamics.

Chapter 6 discusses the effectiveness of estimating heat flow in the vicinity of nearby seismic lines, using both the calculated thermal conductivities and the heat flow probe measured thermal conductivities in combination with the respective geothermal gradients derived from measured BSR depths. The two thermal conductivity sources are compared and the errors, possible uses and related issues are discussed, such as variable lithologies and fluid flow.

Chapter 7 summarises the findings made throughout Chapters 3 to 6, and discusses possible future work which could further this research.

2 Data

2.1 RR1508 Survey

The data set that this project is based around is a combination of heat flow and seismic data that were collected on the *RV Roger Revelle* off the East Coast of the lower North Island in June 2015. The cruise, RR1508, was titled "A Subduction Thrust Investigation of New Zealand using Geothermics and Seismics (STINGS)". The overall goal of the cruise was to 'investigate the thermal regime and structure of the Hikurangi Margin and its influence on slow slip earthquakes' (Harris et al., 2015a).

The cruise collected heat flow, bathymetric, seismic and eXpendable BathyThermograph (XBT) data. The cruise was split into two surveys: the northern and southern field areas (Figure 2.1). The northern area is directly east of Hawkes Bay (Figure 2.2) with the southern area directly east of Wellington (Figure 2.3), both straddling the deformation front of the Hikurangi Margin.

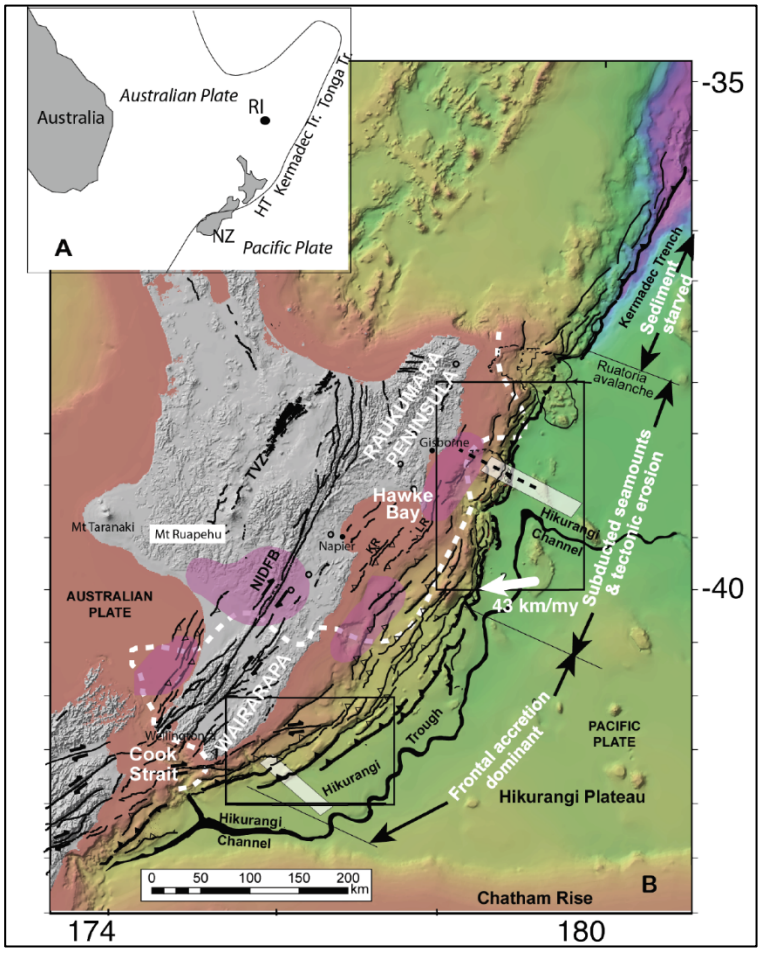

Figure 2.1 Map showing the two survey areas (black boxes) top HKS01 and bottom HKS02 and the major tectonic features of the area (Harris et al., 2015a).

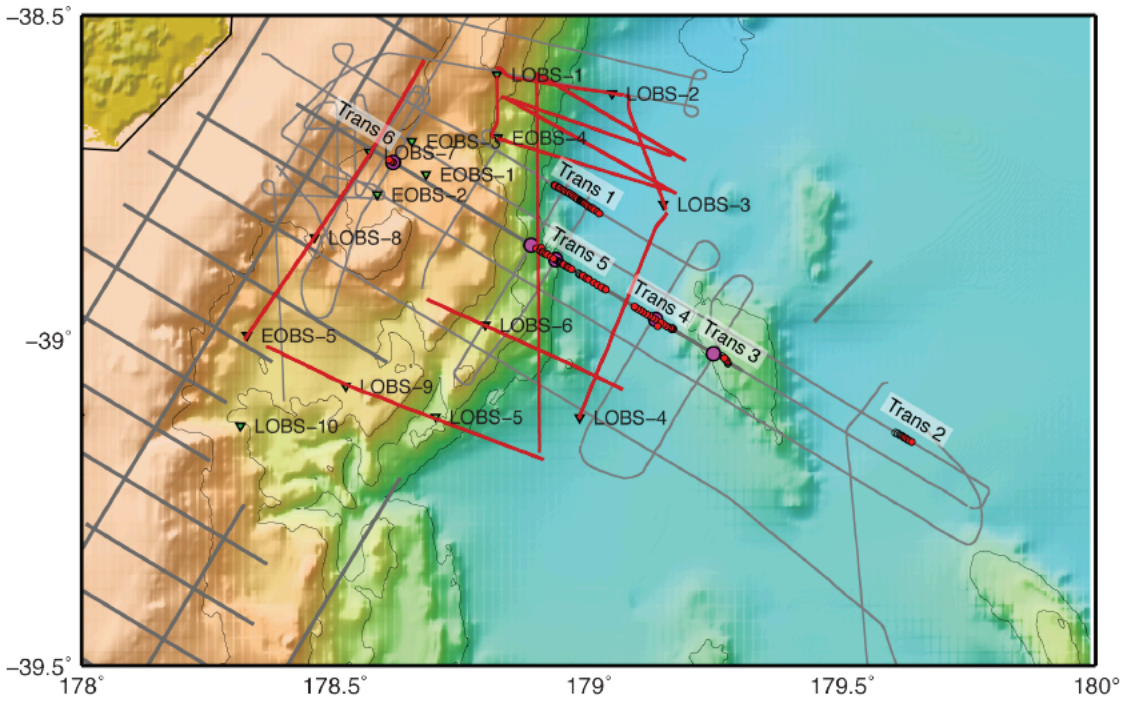

Figure 2.2 Map showing the ship track of the RV Roger Revelle from field area HKS01 along with the deployed ocean bottom seismometers (Harris et al., 2015a).

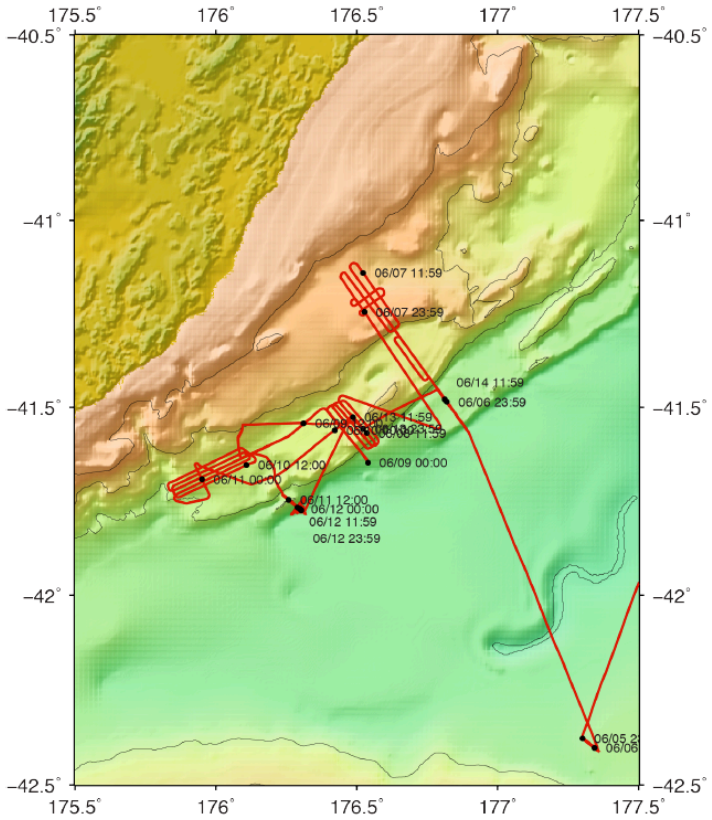

Figure 2.3 Map showing the ship track of the RV Roger Revelle from field area HKS02 (Harris et al., 2015a).

2.2 High-Resolution Multi-Channel Seismic Survey

A total of 37 seismic reflection lines were collected during the RR1508 cruise, totalling 881 km of seismic data. The survey was conducted as a high-resolution survey to build on previously collected data in the region, while still maintaining penetration into the subsurface. The seismic survey was split up into HKS01 and HKS02, with HKS01 consisting of the first 13 lines and HKS02 the remaining 24 lines (Figure 2.2 and 2.3) (Harris et al., 2015a).

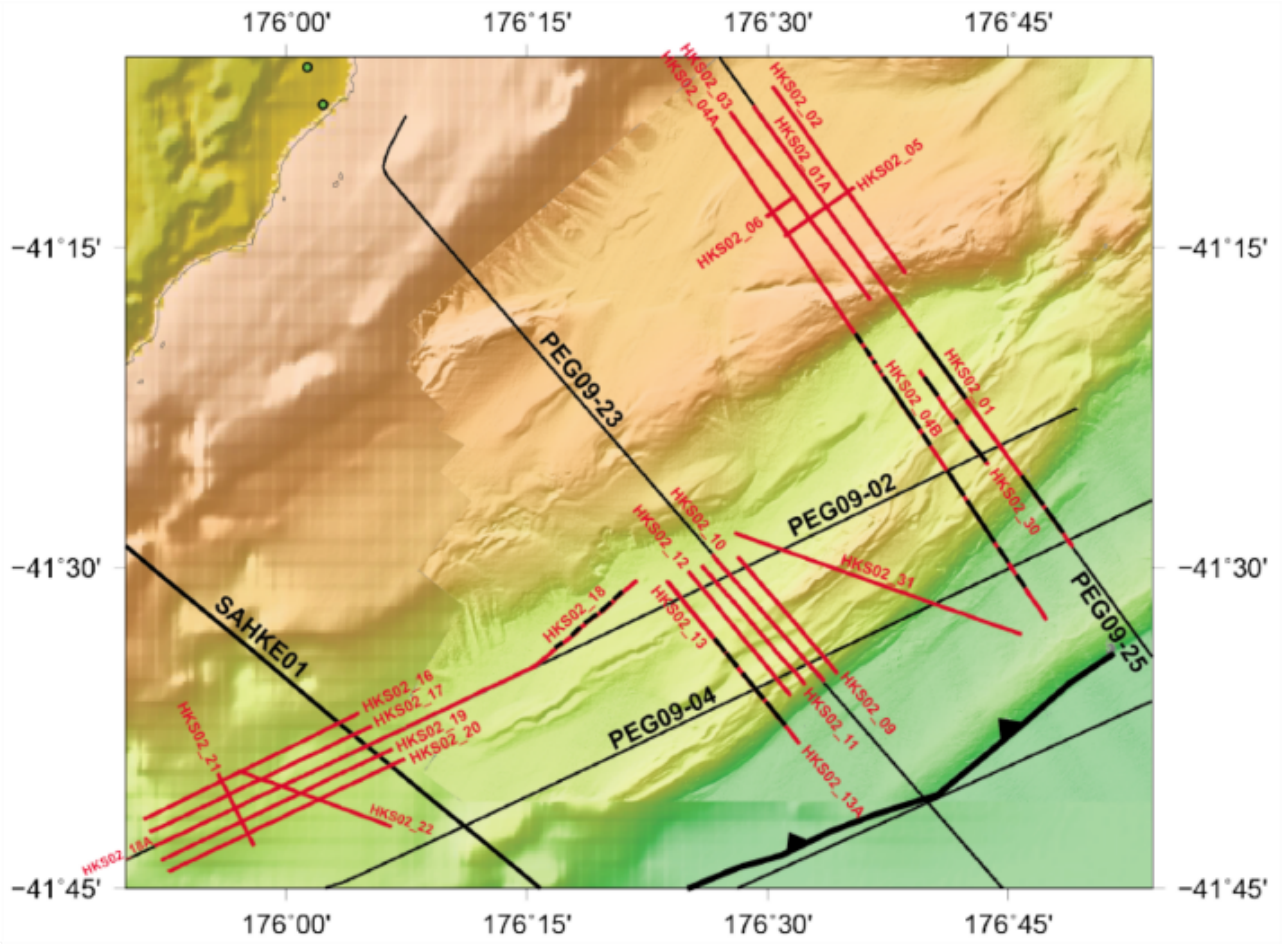

Figure 2.4 A close up showing the HKS02 area. The lines in red are the seismic lines collected during the RR1508 cruise. The lines in black are the previously recorded seismic lines from the PEG09 survey (Harris et al., 2015a).

This thesis focuses on the data collected above Pukeroro Ridge in the centre of the southern field area. Specifically, lines HKS02_09, 10, 11, 12 and 13A (*Figure 2.5*).

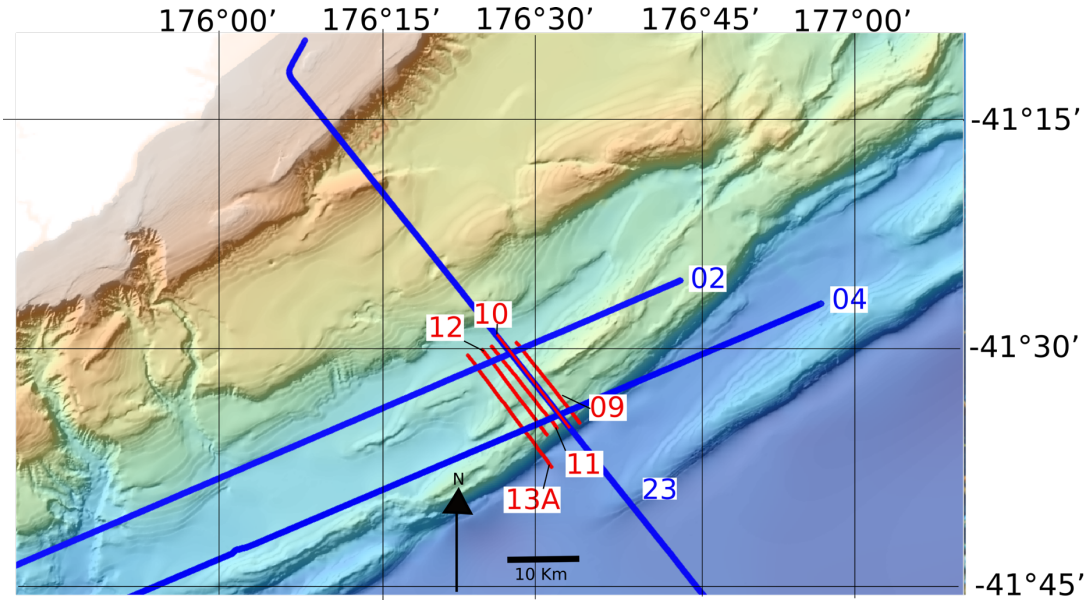

Figure 2.5 A close up of the seismic lines focused on in this thesis, with the Roger Revelle lines in red and the PEG09 lines in blue.

The seismic system used was a portable seismic reflection system from Scripps Institute of Oceanography (the host institution of the *RV Roger Revelle*). The system is made up of two 45/105 cubic inch generator injector guns, deployed 2 m apart mounted on a floating steel frame as a seismic source. A 600 m long 48 channel Geometrics GeoEel hydrophone digital streamer was used as the receiver. Both the source and receiver were towed at 3.5 m below the surface, with the receiver's depth controlled by four evenly distributed compass birds (Baker, 2016).

The survey had a shot spacing of 25 m (triggered by the GPS system), with a nominal fold of 12. The records had a length of 8 s with a 1 ms sampling interval. The shot locations were recorded using the ship's navigation in NZTM2000.

Several notable difficulties arose during the data acquisition. The setup presented issues related to the absence of recorded receiver locations, short offsets, low fold and decreased penetration. The high resolution, relative to industry surveys, was produced by using a higher frequency sound source, however this also resulted in decreased penetration. Additionally, wildlife encounters shut down the survey on multiple occasions resulting in incomplete lines (Harris et al., 2015a).

2.3 Heat Flow Measurements

191 heat flow measurements were taken during the survey, across 17 heat flow deployments or "stations". The 17 heat flow stations were located along 10 heat flow transects across the two survey regions (Harris et al., 2015b). Data from all 17 heat flow stations where used to create our heat flow transects

Table 2.1. Table showing heat flow stations and their corresponding transect numbers and survey areas.

HEAT FLOW STATION	SURVEY REGION	TRANSECT NUMBER
HK1	Northern	Transect 1
HK2	Northern	Transect 2
HK3	Northern	Transect 2
HK4	Northern	Transect 3
HK5	Northern	Transect 6
HK6	Northern	Transect 5
HK7	Northern	Transect 5
HK8	Northern	Transect 4
HK9	Northern	Transect 4
HK10	Northern	Transect 1
HK11	Southern	Transect 7
HK12	Southern	Transect 9
HK13	Southern	Transect 8
HK14	Southern	Transect 8
HK15	Southern	Transect 9
HK16	Southern	Transect 10
HK17	Southern	Transect 9

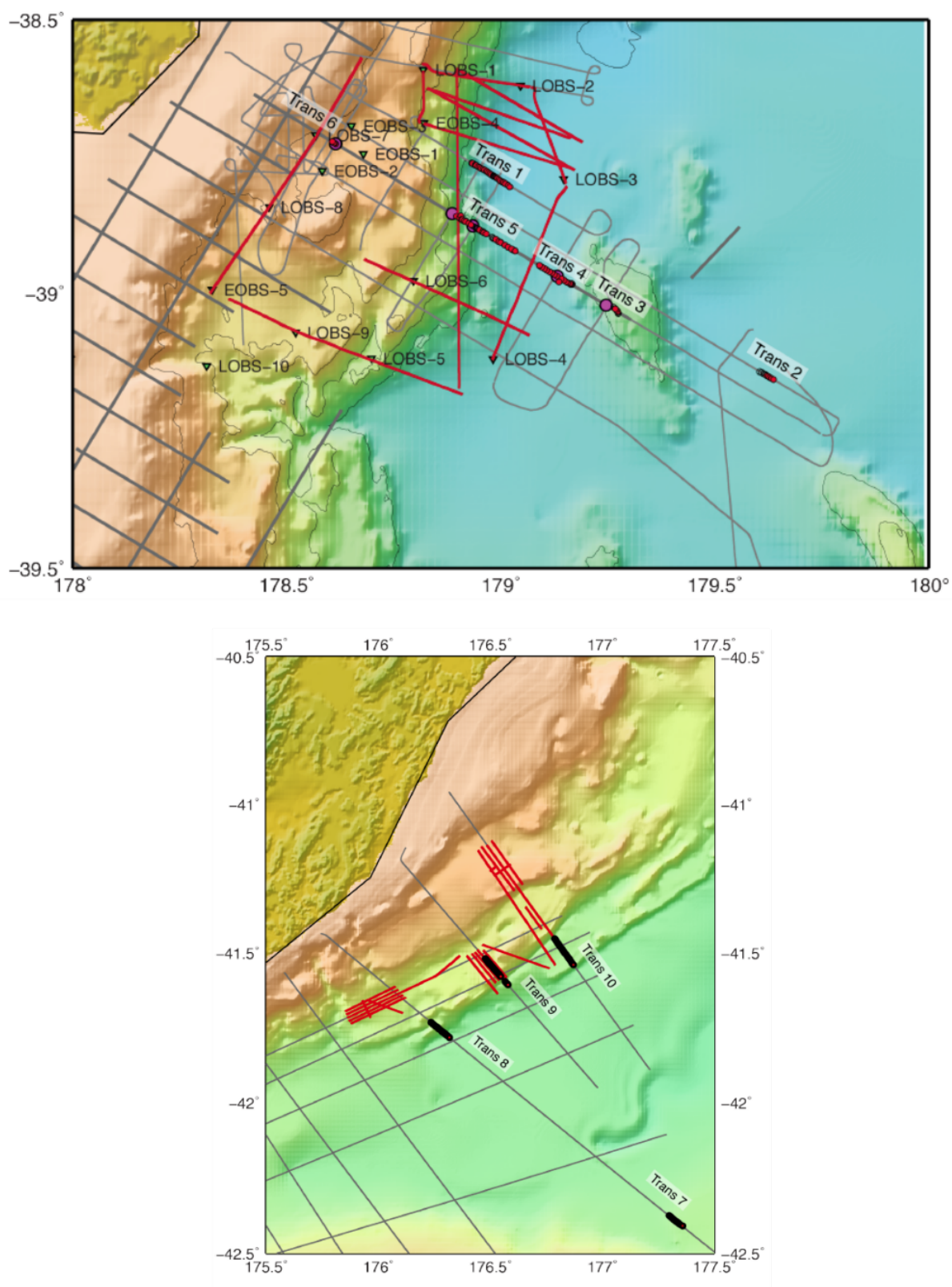

Figure 2.6 Maps showing the locations of heat flow transects 1-10 from HKS01 (top) and HKS02 (bottom) (Harris et al., 2015b)

Heat flow measurements were taken to measure the thermal gradients and temperature decay rates of the subsurface, with the survey areas focused around areas of faulting and slow slip seismic events.

The temperature measurements were all recorded using the Oregon State University's multi penetration heat flow (MPHF) probe. The MPHF probe consists of a 3.5 m violin bow heat flow system, containing 11 thermistors. The probe contains a solid-state data logger in the weight stand which records; time, pressure, water temperature, tilt and a stable reference resistance (Harris et al., 2015b) (Figure 2.7).

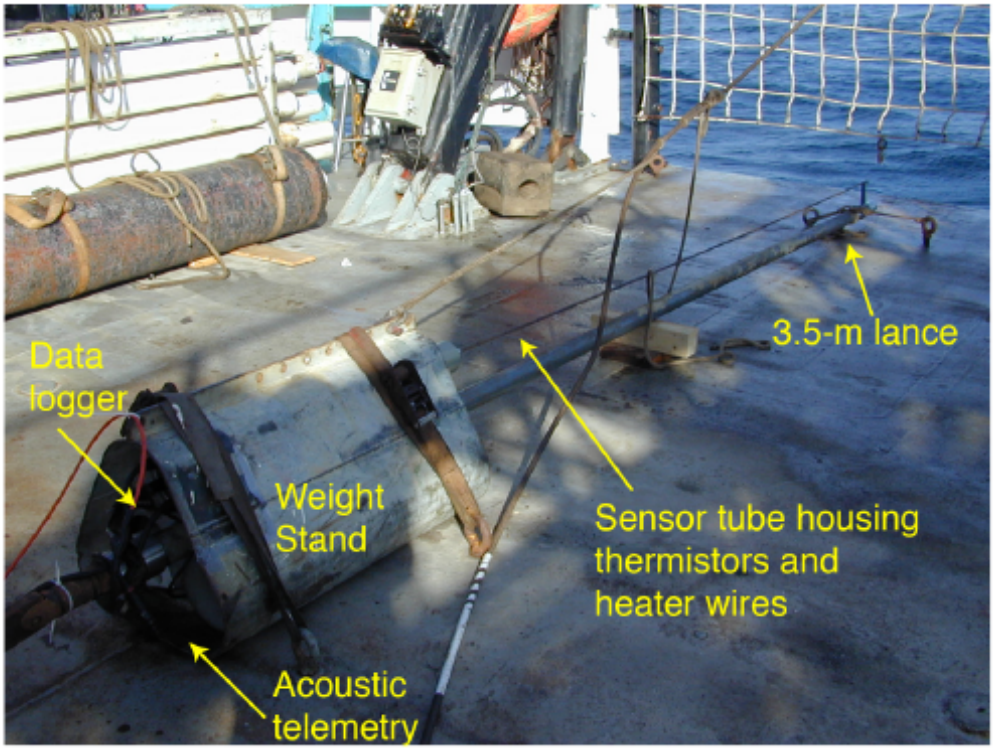

Figure 2.7 Annotated photo showing the heat flow probe used to collect heat flow data during the RR1508 cruise (Harris et al., 2015a)

During the data collection, the heat flow probe is lowered off the back of the boat using a trawl wire. The probe is lowered into the sediment under the force of the weight attached to the top of the probe. Once the probe is completely inserted, temperature recordings begin at a sampling interval of 10 s for 7 minutes. Over the 7 minutes, the thermistors reach equilibrium with the surrounding sediment; it is these temperatures that are used to calculate the thermal gradient of the sediment. After the initial 7-minute period, a calibrated heat pulse

is produced by the heater wire in the sensor tube. The thermistors then measure the resulting temperature decay *in situ*. The probe is then removed and pulled about 100 m above the seafloor while the boat travels to the next heat flow location at 1-2 knots (Harris et al., 2015a).

2.4 Data Processing

The data sets collected during the RR1508 and PEG09 surveys are both high quality. Both surveys required processing to refine the data and highlight the near surface features which are the focus of this thesis.

2.4.1 **RR1508 Data Processing**

2.4.1.1 SEG-D to SEG-Y Conversion

The data were received as individual SEG-D files for each shot, as well as navigation files in the form of .p190 files. The SEG-D files must be converted into SEG-Y files for each line of data (Barry et al., 1975). A shot file (ending with the file extension ".sht") was also produced that contains an ASCII text listing of the shot number and GPS coordinates for each individual shot (Ravens, 1995).

2.4.1.2 Geometry Conversion

The geometry conversions for the RR1508 data set were performed using the geometry tool in the seismic processing software GLOBE Claritas. The geometry tool uses the observers' logs and navigational text files to create a geometry data base. The tool uses pre-measured offsets (Figure 2.8) from the seismic acquisition to co-ordinate 2D seismic geometric information (Ravens, 1995). The geometry tool is also used to place shots into their corresponding bins.

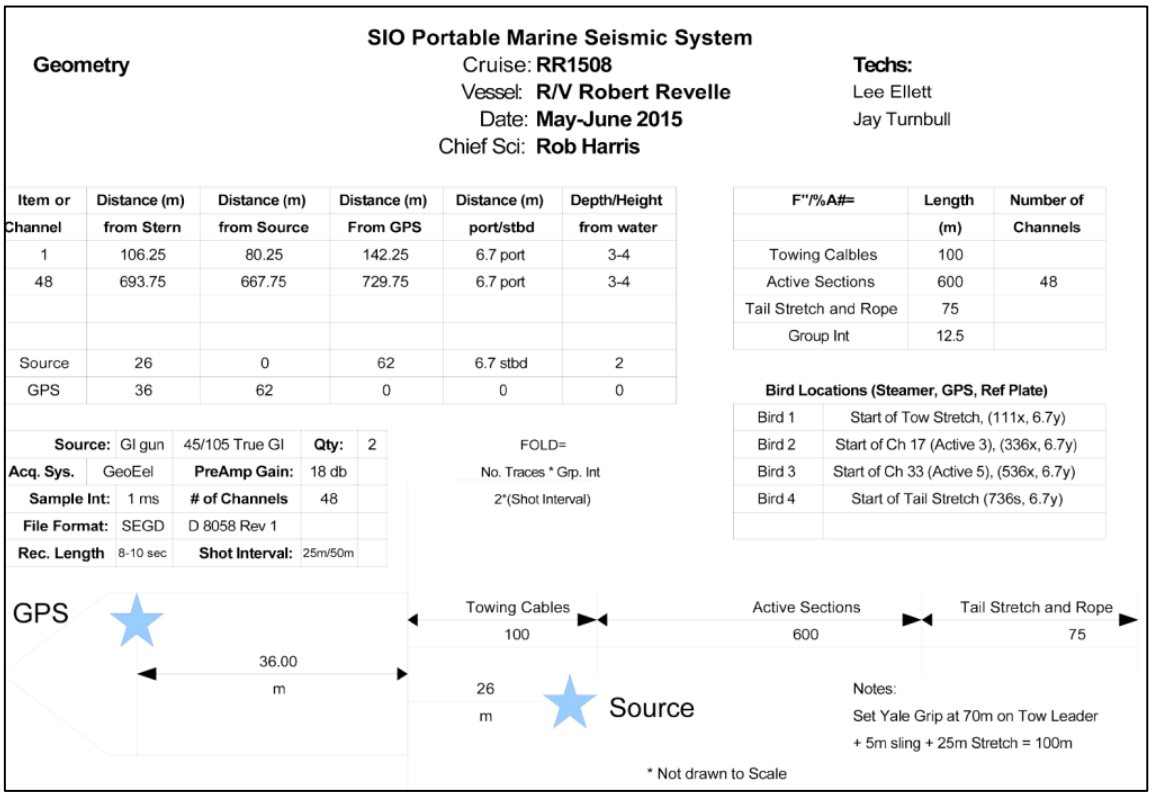

Figure 2.8 The geometry layout of the SIO Portable Marine Seismic System used during RR1508 (Harris et al., 2015a)

2.4.1.3 Static Shifts

Static shifts were applied to the shot records to ensure the times recorded for the reflections were precise and accurate. Errors can be present in the recorded times if the measured offsets change due to wave conditions or if the depths of the source or the receivers change. Incorrect times were found in the RR1508 survey due to a delay between the time of recording and the source producing the sound. Due to the shot time delay, the times for reflections in the data were not representative of the total time taken for the sound to travel from source to receiver (Yilmaz, 2001).

The original results were tested via two methods to determine the depth of the source and receivers to allow for correction. First, the CDP stacks produced were viewed in the Claritas module Xview. In Xview, the time between the top of the recording and the seafloor and the time between the seafloor and the seafloor multiple were compared. If the shot delay time was accounted for these times should be identical.

Five spot pick comparisons were undertaken along each line, calculating the differences and then averaging them across all the picks. This was, however, deemed to be too variable and the picking of the same points was too imprecise, leading to incorrect static shifts being applied.

The second method used was to apply a Linear Move Out correction (LMO) to the shot records. By applying a LMO of 1500 m/s plus a time shift of 50 ms, if the shot records were correct they would line up at the 50 ms mark. The static shift time was then adjusted until it aligned on the 50 ms mark. After testing multiple different static shifts, a shift of 50 ms was applied to account for the delay between the air gun firing and the system recording. This 50 ms shift moved the entire survey up by 50 ms.

2.4.1.4 CDP Sort

The next module was the common depth point (CDP) sort job of GLOBE Claritas, which combines source-receiver pairs to convert the data from shot gathers to CDP gathers. This allows the data to be associated with common reflection points, rather than with the source locations (Wood and Treitel, 1975). This step is essential to allow a number of reflections to be stacked together, thereby improving the quality of the final product (Fletcher, 2016).

2.4.1.5 FDFilt

Following CDP Sort, the FDFilt module was applied. FDFilt is a frequency-domain bandpass filter used to remove extreme frequencies based around four user-defined corner frequencies (XSGEO, 1999a). By using four corner frequencies, frequencies that could not have been produced from the source or reflections can be isolated and removed (Figure 2.9). These frequencies correspond to a large proportion of the noise, which can corrupt and contaminate the data (Yilmaz, 2001).

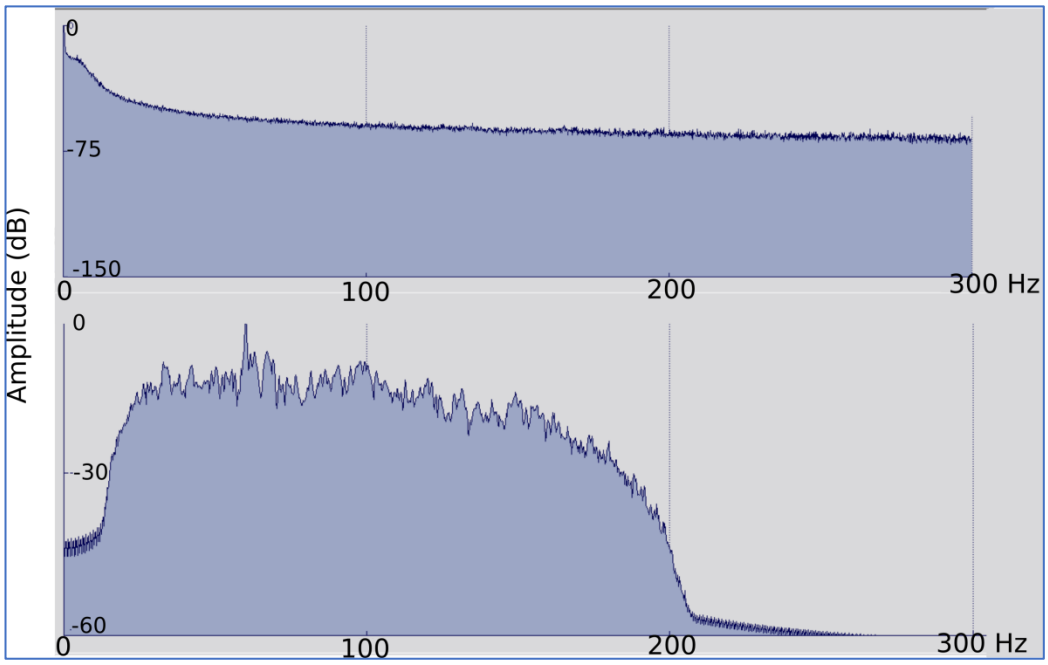

Figure 2.9 Two frequency spectra taken from the same location on Line 10. The top spectrum has no bandpass filter applied while the bottom graph has been filtered using FDFILT. The amplitudes shown in the two graphs do not have the same scale.

2.4.1.6 Spherical Divergence

The spherical divergence correction is a dynamic scaling applied to seismic data. The scaling compensates for loss of energy due to a reduction in the amplitude of the seismic waves resulting from geometric spreading of the wave, as well as attenuation due to dissipation of the energy (Ravens, 1995).

To compensate for the amplitude reduction, the module multiplies the trace samples by a scalar amount using the Equation 2.1

$$G(t) = V(t)n\ tm \exp[V(t)t\alpha]xq \quad (2.1)$$

Where,

n=VPOWER1- Power value of the average velocity at T (two-way time)

m=TPOWER1- Power value of the two-way time used in calculation the spherical divergence

q=XPower1- Power value of offset used in calculating the trace-by-trace scalar

α=ALPHA1- Power of exponential term

(Figure 2.10)

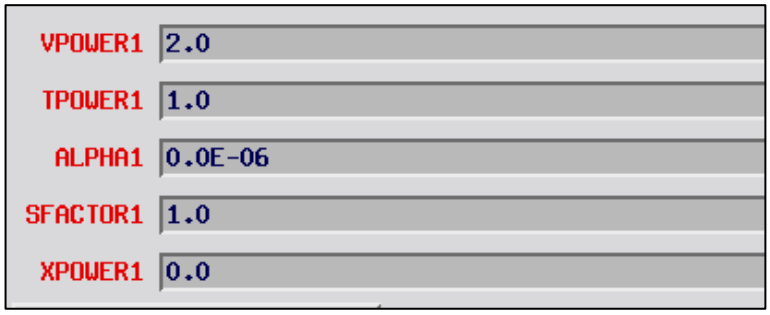

Figure 2.10 The parameters window from the GLOBE Claritas spherical divergence module.

2.4.1.7 NMO

Once the geometry has been corrected and the various filters and mutes have been applied, a velocity analysis is undertaken using the GLOBE Claritas velocity analysis (CVA) utility. The NMO correction aims to take into account the effect resulting from the change in distance between the source and receivers. The identified velocities calculated by the CVA utility are applied as NMO corrections. The NMO correction replaces the assumed velocity of sound through the subsurface with a more realistic velocity (Yilmaz, 2001). Initial stacks were produced assuming that the subsurface velocity increases from 1500 m/s at the seafloor, constantly increasing with depth to a velocity of 2000 m/s at 3.75 s. In reality, the velocities change at variable rates dependent on the rock types in the subsurface. Velocities generally increase in steps due to changes in rock type, which is especially apparent in sedimentary rock units (Fletcher, 2016). Velocity picking was a very important part of the data processing flow as these velocities are used to convert the seismic data from time to depth (Chapter 2.4.1.13).

The velocities from the RR1508 cruise were picked in CVA using semblance plot (Figure *2.11*). A semblance plot is a plot of stacking amplitudes or energy graphed by time vs stacking velocity, showing the velocities with highest levels of energy. Picking the velocity-time pairs where the energy is highest allows determination of the velocities where stacking will occur best (XSGEO, 1999b).

The initial attempt at picking correct velocities for the RR1508 data set left sections of poor stacking and migration artefacts. The picked velocities were most likely incorrect due to the short offsets in this particular high-resolution data set seismic data set, as discussed in Chapter 3.

These short offsets result in low fold and as a result the velocity picking is less accurate than for longer offset data. To account for this, we made use of the velocities that were picked during the commercial processing of the coincident PEG09 survey. Line 23 of the PEG09 survey actually overlaps with Line 10 from the RR1508 survey. As the PEG09 survey had much longer offsets (10 km), the picked velocities were more accurately constrained. Using the PEG09 velocity profile in the coinciding region, our velocity profiles were adapted and altered (Figure *2.12*). When this new velocity profile was used, the stacks and migrations produced better quality data. While the other RR1508 lines did not coincide specifically with any other commercial lines, they did run across similar stratigraphy as Line 10. This meant similar velocities were likely. Using Line 10 as a guide, the remaining velocity profiles were modified and the resulting seismic lines were improved.

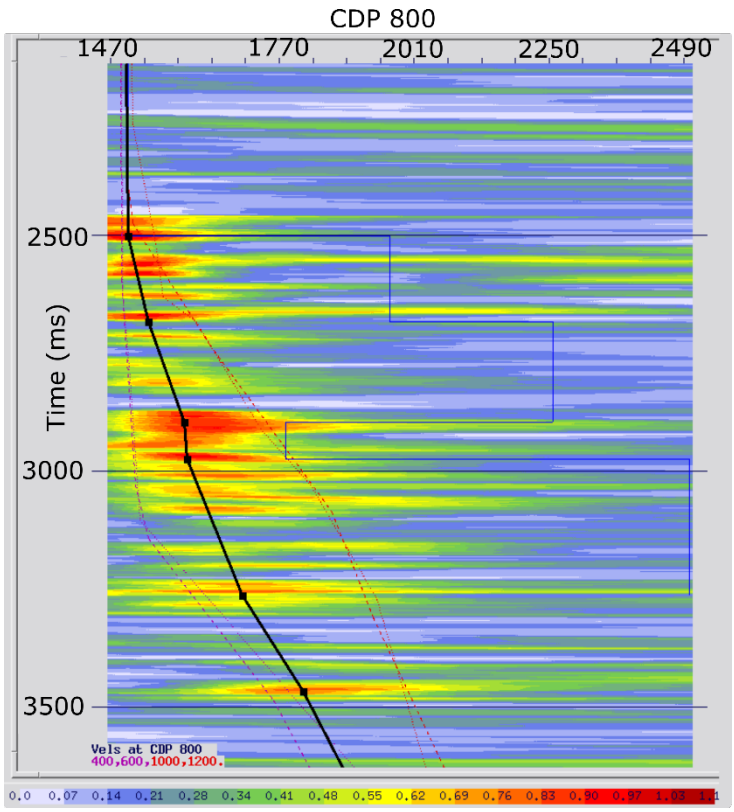

Figure 2.11 *An example semblance window (CDP 800 from Line 10) during velocity picking. The black points connected by the black line are the velocity picks that have been made.*

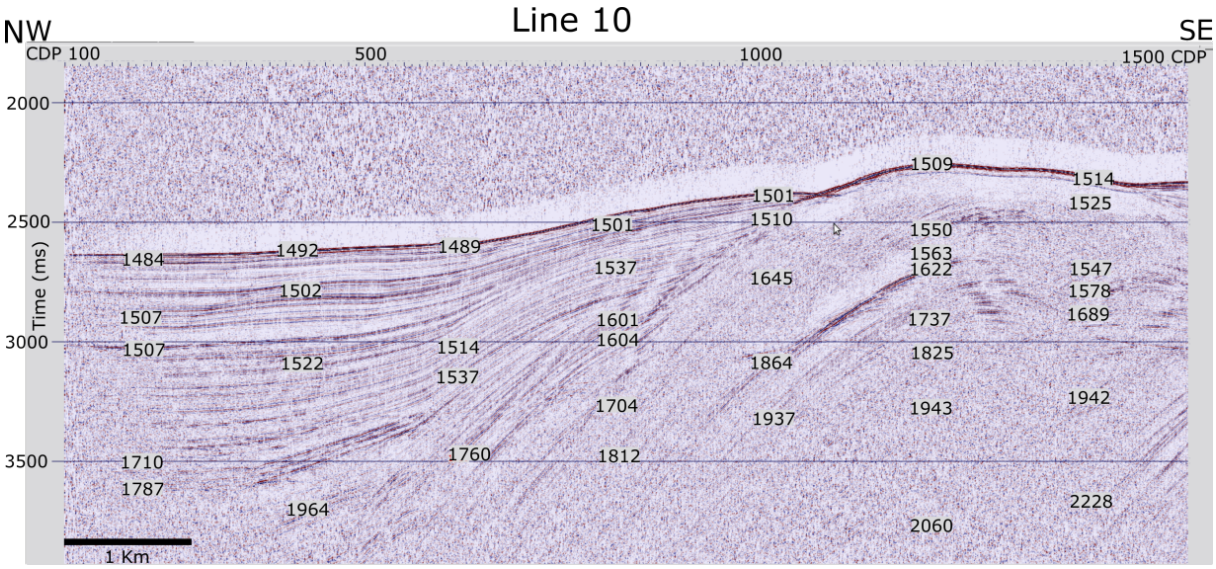

Figure 2.12 *A stack of Line 10 with picked seismic velocities from PEG09 Line 23 overlain.*

2.4.1.8 Stacking

The stacking module in GLOBE Claritas is used to sum the individual traces contained within each CDP into a single trace. Stacking emphasises reflection signals, making them stand out from noise that does not stack in, due to its random nature. This increases the signal-to-noise ratio and improves data quality. Traces with common reflection points (another, more accurate, term for CDP) are stacked to form a single trace (Yilmaz, 2001).

The conventional stacking method from GLOBE Claritas was used. Conventional stacking evenly weights each trace and simply sums all the data. This method was used as there was no reason to favour particular traces. The fold, which is the number of traces combined for each CDP, was only 12 for the RR1508 compared with the much larger 133 for the PEG09 data set. The lower fold was due to the short streamer length and smaller number of receivers numbers used in the RR1508 survey (Ravens, 1995).

2.4.1.9 Balance

The balance process scales each trace by a scalar constant that does not vary over time. This scalar is set so that the average amplitude of each trace is constant across the survey. This means the traces are evenly balanced in energy from trace to trace, creating a so-called horizontally balanced section of traces (Ravens, 1995).

2.4.1.10 Finite Difference Migration

The Finite Difference Migration (FDMIG) module was used to perform migrations using a defined interval velocity model of the data. Migration is used to correct for geometrical features that arise during stacking as well as inaccurate NMO corrections caused by non-flat features. When an NMO correction is applied and the data is stacked, dipping events are imaged incorrectly, appearing flatter and further down dip than they are in reality. As well as incorrect imaging of dipping events, discontinuities such as faulting can cause diffractions (Yilmaz, 2001).

Interval velocities produced from the earlier derived stacking velocities were used to migrate the data (Figure 2.13). Interval velocities contain velocities at individual pre-determined time windows (e.g., 5 ms). This is different to the stacking velocities which represent an average velocity for the entire area above the point where the velocity is recorded.

These interval velocities are calculated using the Dix's Equation (2.2), seen below.

$$V_{int} = [(t_2 V_{RMS2}^2 - t_1 V_{RMS1}^2) / (t_2 - t_1)]^{1/2} \quad (2.2)$$

Where

V_{int} = interval velocity

t_1 = travel time to the first reflector

t_2 = travel time to the second reflector

V_{RMS1} = root-mean-square velocity to the first reflector

V_{RMS2} = root-mean-square velocity to the second reflector.

(Ravens, 1995)

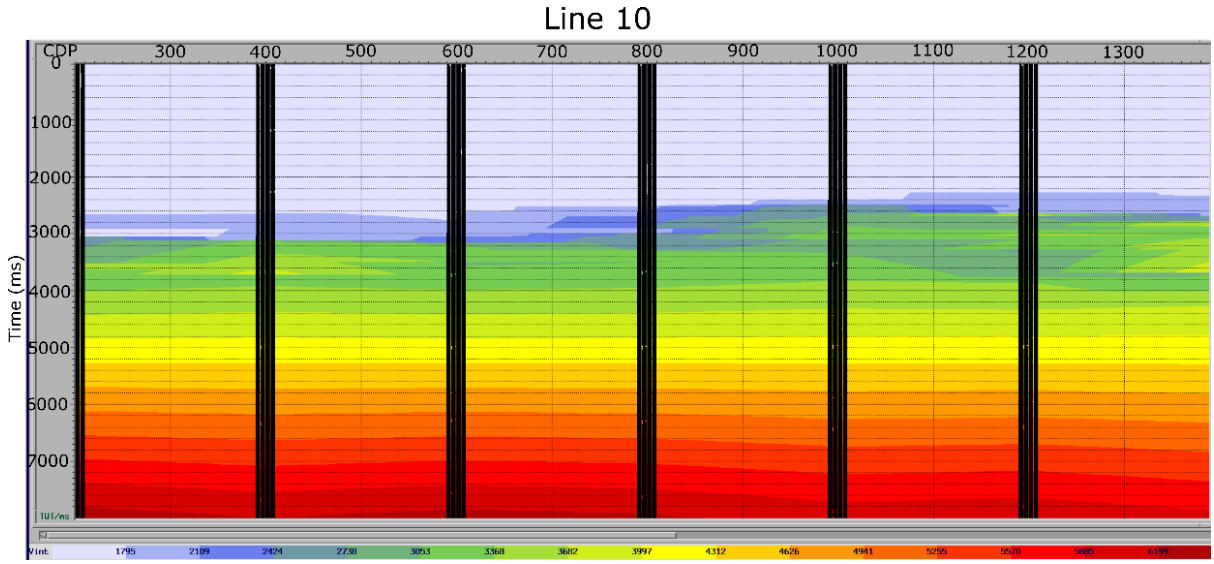

Figure 2.13 An isovels window of Line 10 with the interval velocity isovels in the background with the interval velocity picks (black bands) overlain.

2.4.1.11 STATICS - Source and Receiver Depth Corrections

Like the static used to correct for the delay in recording applied at the beginning of the flow, another bulk shift is applied to compensate for the source and receivers sitting beneath the surface of the water. A bulk shift of -5 ms was applied to the data to correct for this error. The bulk shift is applied at the very last step in processing so as not to influence any of the stacking and only the overall times (Yilmaz, 2001).

2.4.1.12 SMUTE

The surgical mute (SMUTE) module was used to remove any data collected from above the seafloor reflection. The purpose of the mute is purely aesthetic as the data above the seafloor are irrelevant and contain only noise for this study (Figure 2.14). The surgical mute is applied based on a digitally picked horizon. Using the automatic horizon picking tool, the reflection representing the seafloor was identified, and once read in, any data preceding the reflection was removed (Mavko, 2005; Gadallah and Fisher, 2009). A 10 – 50 ms buffer was used so as not to accidentally mute the seafloor due to horizon picking errors.

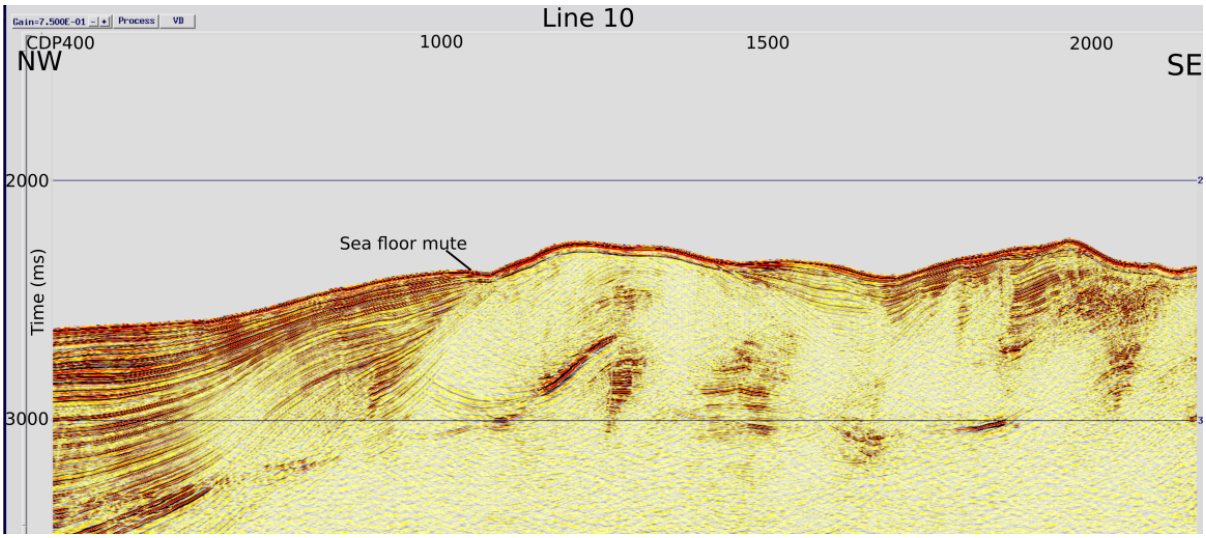

Figure 2.14 Line 10 with a surgical mute applied at the seafloor. The mute's effect is evident by the lack of data in the water column. The CDP spacing is 6.25 m.

2.4.1.13 TDCONV1

The time-to-depth conversion model was an important final step which uses previously picked stacking velocities to convert the Y axis from time to depth. This step was important for this research as the depth measurements of both the BSR and seafloor are both potential sources of error. By creating as accurate a velocity profile as possible, the time to depth conversion errors were reduced (Ravens, 1995).

2.5 PEG09 Survey

To complement the RR1508 seismic-survey by increasing seismic line coverage and making use of the long offset data-set for analysis, data from the PEG09 cruise were selectively used throughout this thesis. PEG09 was an industry focused cruise completed by Reflect Geophysical using the *MV Reflect Resolution* in 2009 and 2010. The survey was undertaken by the New Zealand government to try to generate hydrocarbon exploration interest in the region (Baker, 2016). Identification of specific hydrate features in the PEG09 data was used to position the survey lines for RR1508.

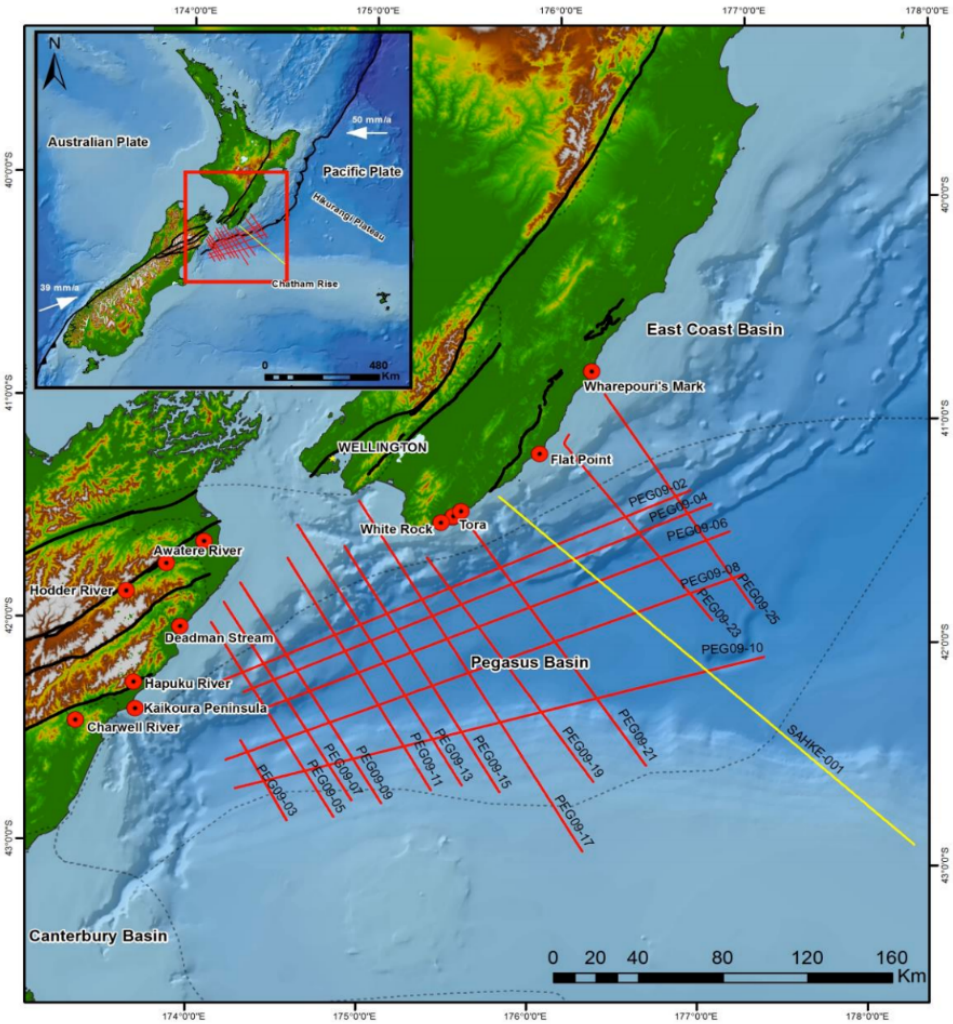

Figure 2.15 *Map showing the distribution of the PEG09 seismic survey (red), also including the SAHKE-001 line (yellow) (NIWA, 2013).*

The line coverage (Figure *2.15*) extends from south of the Uriti Basin to just north of the Canterbury Basin. While the majority of the lines are south of the field area, Pegasus Line PEG09_23 runs along the same transect as HKS02_10 and Heat Flow Transect 9. HKS02_10 and Heat Flow Transect 9 were purposefully positioned on top of PEG09_23 as it provides a long offset, lower resolution seismic data set for comparison.

The PEG09 data were collected using three Bolt APG 8500s airguns with a 5 m spacing as the source and a 10,000 m, 800 channel MSX solid (gel-filled) digital hydrophone streamer as a receiver. The receiver and source were both deployed at a depth of 11 m. DigiCourse birds with compass levellers were used to orientate the streamer. The 37.5 m shot spacing resulted in a fold of 133. The records were 12 s long, recording at a 2 ms sampling interval (RPS Energy Pty Ltd, 2010). The long offsets and increased fold created a data set capable of much more accurate velocity analysis, and as a result can be used as an error estimation tool for the RR1508 velocity calculations performed in this thesis.

2.5.1 **PEG09 Data Set**

The Pegasus data set was obtained in a partially processed format, having been processed by Geotrace for resource exploration potential. While SEG-D data were also available, the commercially processed data provided sufficiently accurate velocities allowing for depth conversions and comparison with the RR1508 data.

PEG09 was processed with the aim of producing good clear images with high signal-to-noise ratios, while preserving relative amplitude information suitable for hydrocarbon identification (Table 2.1) (RPS Energy Pty Ltd, 2010). There were several major differences between the processing flows of the PEG09 and the RR1508 data sets which are discussed in Chapter 3.

Table 2.*1 The processing flow used by Geotrace to process the Pegasus data set (RPS Energy Pty Ltd, 2010)*

Production Processing Flow

Preliminary Processing:

1. Input from SEGD.
2. Navigation Merge
3. Source de-signature to convert data to minimum phase
4. Resample to 4ms
5. Low cut filter: 2 (6) Hz (dB/Oct)
6. Temporal anti-alias high cut filter: 90 (72) Hz (dB/Oct)
7. T^2 amplitude recovery
8. Amplitude Statistics and trace quality control
9. Bad shot and trace edits
10. TFD swell noise attenuation in shot and receiver domain

Pre-stack Processing:

11. Sort CDP domain (various fold depending on survey acquisition details)
12. Preliminary velocities Analysis (1km interval)
13. FX interpolation in CDP domain to generate 2*fold CDPs
14. Full SAA on interpolated, NMO corrected CDPs
15. Radon Demultiple (1st Pass) incorporating stretch mute
16. Interpolated traces dropped
17. Random and/or Diffraction noise attenuation in receiver and CDP domain

Migration Processing:

18. Migration Velocity Analysis (1km) – Curved Ray Kirchhoff, 2km half aperture
19. Smooth migration velocities
20. Main 2D Curved Ray Kirchhoff Time Migration, 2km half aperture; dip limit tapered from 55 to 65 degrees

Post Migration and post-stack Processing:

21. Residual velocity generation and interpretation (500m spacing)
22. 4th Order residual NMO correction
23. FX interpolation in CDP domain to generate 2*fold CDPs
24. High resolution Radon
25. Interpolated traces dropped
26. Inner trace mute – 5 degrees angle inside mute
27. Outer trace mute – 40 degrees angle outer mute
28. Time Variant Bandpass Filter
29. Phase-only Q Compensation
30. Stacks – full angle (5°-40°), near (5°-20°), middle (15°-30°) and far angle (25°-40°)
31. 10 trace 2D SNIP noise attenuation
32. Residual Gain
33. Amplitude scaling – 1000ms stable AGC
34. Gun and cable static (10ms)

Final Deliverable/Archive Production:

35. Migrated final stacks: full offset scaled and angle scaled (near, mid and far)
36. Raw Un-migrated Stacks

2.6 IHS Kingdom Analysis

Once both the PEG09 and RR1508 processing was complete and finalised, the surveys were written out as Claritas SEG-Y files and imported into the IHS Kingdom analysis package. Kingdom software allows the plotting of the line coordinates on a map, so the different surveys can be viewed together. The package also maps line intersections and allows images to be built comprised of several seismic sections from crossing surveys. This feature was important in ensuring the lines all intersect at correct locations and it also acts as a quality control measure for the depth conversion process (Figure 2.16).

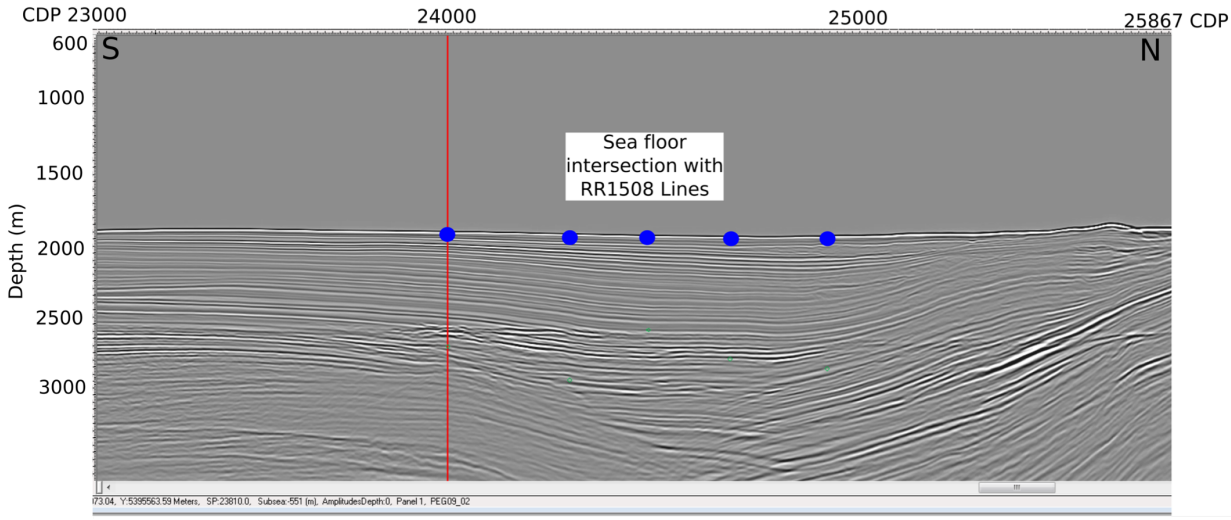

Figure 2.16 Kingdom window showing Line PEG09_02 with annotations (dots) for the seafloor intersections with 5 RR1508 lines. The presence of the blue intersection markers at the seafloor indicates an accurate time-to-depth conversion within the water column. CDP spacing is 6.25 m.

After the lines were loaded and tie lines indicated that the depth conversions were accurate and uniform, both the seafloor and BSR events were digitised with the depth at every CDP recorded (picked) (Figure 2.17). The seafloor was picked using the 2D hunt picking tool which picked the seafloor based on amplitude. The seafloor was then corrected in any sections where the picks deviated using the manual picking tool.

The BSR was picked entirely using the manual picking tool as the BSR was too intermittent and varying for the automated 2D hunt tool. When picking the BSR horizons, the horizon was separated into two, the first being a clearly visible BSR and the second being a weakly interpolated BSR. While both horizons were used for the heat flow calculations, there was an increased error associated with the BSR depth for the interpolated BSR.

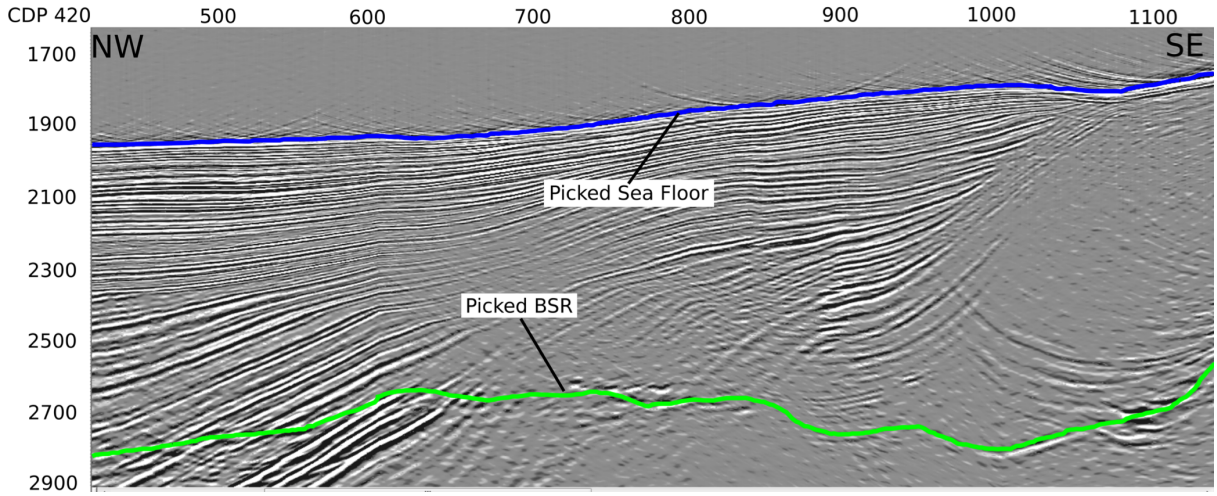

Figure 2.17 An example window showing the seafloor (blue) and BSR (green) picked as horizons. CDP spacing is 6.25.

These picked horizons were then exported out into an Excel spreadsheet along with line number, CDP number and depth. By subtracting the seafloor depth from the BSR, the depth for each CDP, the depth of BSR beneath the seafloor can be calculated.

2.7 Heat flow

The first step in calculating the heat flow from the BSR, is using the BSR as an isotherm. This was done using a script written by Gareth Crutchley of GNS Science, which uses a hydrate stability curve (Figure 2.18) to predict the temperature at the BSR using a predetermined set of depth and environmental conditions such as pore fluid concentration (Appendix 1).

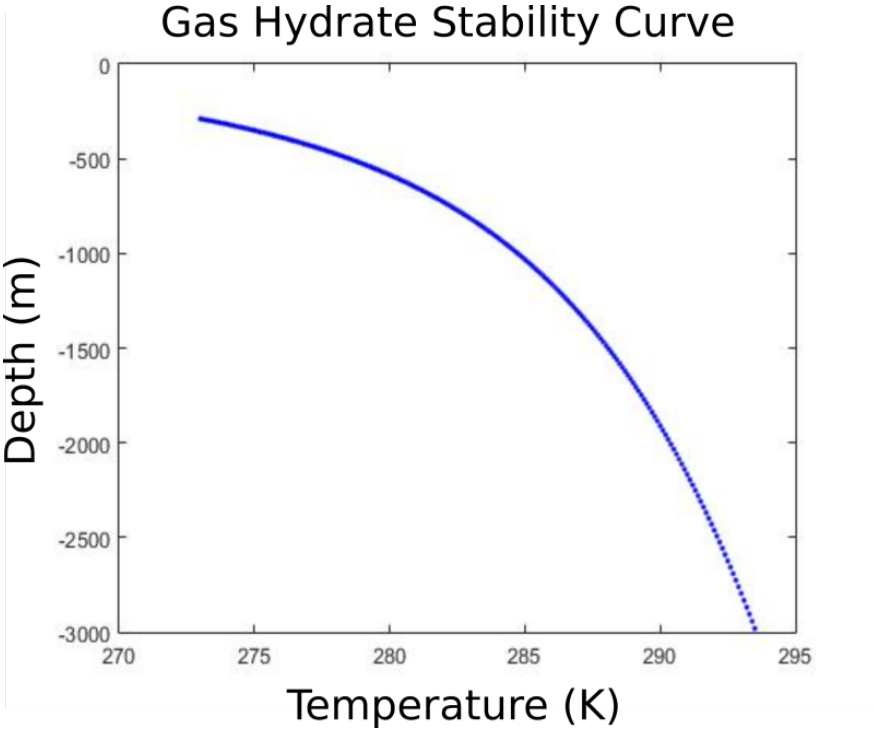

Figure 2.18 Gas hydrate stability curve used to calculate the temperature at the BSR. The curve assumes hydrostatic pressure.

The script requires .csv files containing the depth of the seafloor, depth of the BSR and a temperature profile of the water column. The seafloor and BSR depths were calculated using the picked horizons and the temperature profile used was taken from a nearby autonomous profiling float survey conducted by the ARGO programme in June of 2013. The similar season of data acquisition meant seasonal variations between the temperature profile and the survey were not an issue.

Once the temperature at the BSR had been calculated, the temperature gradient for the subsurface was calculated by using the bottom water temperature from the same autonomous profiling float temperature profile used earlier. This temperature gradient is an integral part of calculating the heat flow.

The heat flow can be calculated using the formula $Q = K(\frac{\Delta T}{\Delta z})$

$$\mathrm{Q}=\mathrm{K}(\frac{\Delta \mathrm{T}}{\Delta \mathrm{Z}}) \tag{2.3}$$

where
Q = heat flow,
K = thermal conductivity
$\Delta T / \Delta z$ = thermal gradient

A large source of error in calculating the heat flow is the estimation of the thermal conductivity of the sediments in the subsurface.

Thermal conductivity is a measure of the ability of a medium to conduct heat. It is measured in W/m/K (Adkins, 1987). In geology, the thermal conductivity of sedimentary units is a very important factor in understanding heat transfer in the subsurface. Thermal conductivity is a highly variable quantity that is largely controlled by pressure acting on a given geological unit as well as the density of the unit (Abdulagatov et al., 2006). As a result of these controlling variables, the thermal conductivities of the subsurface used when calculating heat flow based upon the BSR are likely to be higher than those measured by the heat flow probe.

The majority of thermal conductivity measurements are made in a laboratory setting through a variety of methods: most commonly either a divided bar steady state or a needle probe measurement (Blackwell and Steele, 1989). The divided bar steady state measurement is designed to be undertaken on machined core samples of hard rock. An axial load is applied to a saturated sample, a temperature drop is applied to the sample, and the resulting temperature change is compared to a standard.

The needle probe method is designed for softer samples where needle mounted thermistors are inserted into the sample and a temperature-versus-time plot is produced that can be used to calculate the thermal conductivity (Lockmuller et al., 2004).

These physical measurements are useful but require cores or physical samples that can be difficult to obtain in marine environments. The other issue with physical samples is that surface samples are not always representative of the subsurface as thermal conductivities will change with depth due to pressure.

Since there were no physical measurements of thermal conductivities, the previous heat flow measurements from the probe were used to back calculate thermal conductivities, using the BSR to determine the temperature gradient. By using the heat flow probe derived heat flow measurements, which should be constant, and the thermal gradient derived from the BSR, a corresponding thermal conductivity which produces correct results could be determined.
The issue with this method was that the heat flow probes measurements were taken at sparse intervals, especially when compared to the dense CDP scale used for the BSR picks. To

counteract this, each heat probe site was correlated with its nearest CDP. The heat flow values were then interpolated between points taking into account the general trend of the heat flow to produce a heat flow value associated with each CDP.

2.8 Sources of Uncertainties

Errors and uncertainties are introduced throughout the collection, processing and analysis of the data. While steps have been made to reduce the uncertainties as much as possible, they will always remain.

2.8.1 **Depth Conversion**

The errors associated with the depth conversion are due to incorrect velocity analysis resulting in the time-to-depth conversion being slightly inaccurate. The error margins on the velocity were mostly within 10-20 m/s. At a depth of around 2500-3000 m a 20 m/s error in velocities results in about a 1-1.5% error in the depth conversion. These errors are more significant at shallower depths; however, they were within reason for this project.

2.8.2 **BSR Identification and Selection**

Identifying the uncertainties associated with selecting the BSR is a less quantifiable exercise. For sections where the BSR is clearly visible, the BSR can be identified at a given depth to within about 20 m of its true depth. This uncertainty becomes much larger when selecting an inferred BSR as the selections are based on faint reflections and trends of adjacent more prominent BSRs.

These uncertainties, although smaller than those associated with the depth conversions, have a much larger effect due to their use in determination of the geothermal gradient. These uncertainties can result in deviations of 5-10%

2.8.3 **Heat Flow Interpolation**

There are also uncertainties associated with the heat flow interpolation process, as well as any errors which carried over from the seismic processing and analysis stages. The BSR temperature script makes several assumptions including pore water concentrations and hydrostatic pressures. The best way to deal with these uncertainties is to make sure constant values are used, meaning additional comparisons within the data sets continue to be accurate.

3 High-resolution vs Low-resolution Seismic Data

3.1 Introduction

The co-located PEG09 and RR1508 surveys provide a unique opportunity to compare the products of a high-resolution scientific seismic survey with a lower-resolution commercial survey. The PEG09 survey was undertaken as an industry-style seismic survey by the New Zealand Government, to promote oil and gas exploration off the east coast of the North Island. The deep targets of the survey required low-frequency sound sources in the form of three Bolt APG 8500s airguns (RPS Energy Pty Ltd, 2010), producing frequencies in the range of 2 - 150 Hz. The survey also used a 10,000 m, 800 channel MSX solid (gel-filled) digital hydrophone streamer as its receiver array (RPS Energy Pty Ltd, 2010). The low frequencies and long streamer allowed for substantial penetration and long-offset velocity control.

The RR1508 survey, in contrast, was a research cruise focused on the upper 1500 m of the subsurface. The shallow targets allowed for the use of a high-frequency seismic source as deep penetration was not necessary. The aims of the research cruise were focused on mapping heat flow in the region. This required a higher resolution seismic survey to allow identification of features on a decimetre scale (Harris et al., 2015a). As a result the RR1508 cruise used two 45/105 generator injector air guns producing frequencies between 20 and 450 Hz (WHSC Seismic Profiling Systems, 2016). The survey also was limited by the configuration of the 600 m, 48 channel streamer that was used (Harris et al., 2015a). This length is shorter than optimum, with better velocity control achieved with streamers kilometres in length, but not short enough to cause a major reduction in data quality. The high frequencies used in the survey mean that the signal lost energy much faster by absorption and as a result the use of a much longer streamer would have been of no benefit.

These two seismic surveys are spatially coincident for a portion of PEG09 Line 23 where it overlaps with RR1508 HKS02 Line 10 (Figure 3.1). This identical location and fairly stable locality provide a good situation to compare the results of the two different surveys.

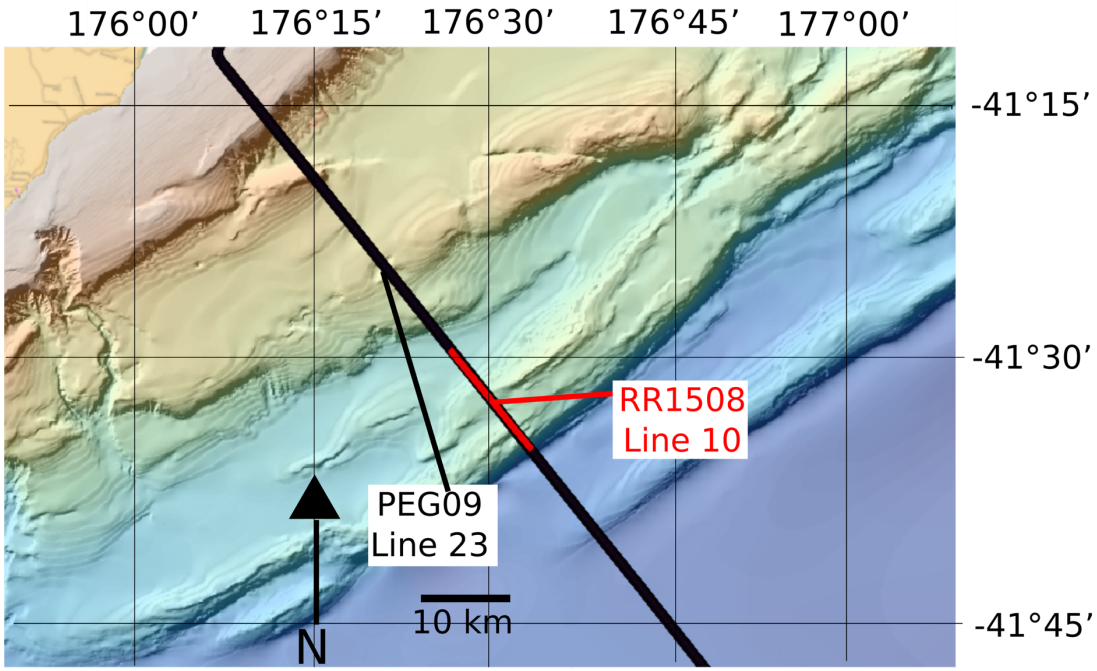

Figure 3.1 Location map showing the RR1508 Line 10 (red) and the PEG09 Line 23 (black).

3.2 Seismic Processing Differences

The processing techniques used on the two surveys varied considerably because of the differences in data quality, the respective strengths and shortcomings of each technique, and the respective targets of the two surveys. The PEG09 data set has been processed by a number of research institutes and companies. The particular processing flow used here is the Geotrace flow. Geotrace is a seismic processing company that was contracted to process data by New Zealand Oil and Gas in 2009 (Table 3.1) (RPS Energy Pty Ltd, 2010). This processing flow is presented as the outputs of Geotrace processing that was compared to the RR1508 data (*Table 3.2*). For the RR1508 processing, our own processing flow was used. Although the eight-year time gap between processing is notable, differences in the technology used are insignificant.

Table 3.1. The processing flow used to refine and improve the RR1508 data set.

RR1508 Processing Flow

Preliminary Processing
1. Import SEGY
2. Apply Static (+50 ms)
3. Apply Geometry
4. CDP Gather
5. FDFILT (12,35,160,210 Hz)

Stack Processing
6. Velocity Analysis (NMO) RMS velocities
7. Stack
8. Balance

Migration
9. Migration (interval velocities
10. Static (-5 ms)

Plotting
11. Seafloor Mute
12. Time to Depth Conversion Interval Velocities)
13. Write to SEGY

Table 3.2. The processing flow used by Geotrace to process the Pegasus data set (RPS ENERGY Pty Ltd, 2010).

PEG09 Processing Flow

Preliminary Processing
1. Input from SEGD
2. Navigation Merge
3. Source de-signature to convert data to minimum phase
4. Resample to 4 ms
5. Low cut filter: 2(6) Hz (dB/Oct)
6. Temporal anti-alias high cut filter: 90(72) Hz (dB/Oct)
7. T^2 amplitude recovery
8. Amplitude statistics and trace quality control
9. Bad shots and trace edits
10. TFD swell noise attenuation in shot and receiver domain

Pre-stack Processing
11. Sort CDP domain
12. Preliminary velocity analysis (1km)
13. FX interpolation in CDP domain to generate 2x fold CDP's
14. Full SAA on interpolated, NMO corrected CDP's
15. Radon demultiple (1^{st} pass) incorporating stretch mute
16. Interpolated traces dropped
17. Random and/or Diffraction noise attenuation ion receiver and CDP domain

Migration Processing
18. Migration velocity analysis (1 km) Curved ray Kirchhoff
19. Smooth migration velocities
20. Main 2D curved ray Kirchhoff time migration

Post Migration and Post-stack Processing
21. Residual velocity generation and interpretation
22. 4th Order residual NMO correction
23. FX interpolation in CDP Domain to generate 2x fold CDPs
24. High resolution radon
25. Interpolated traces dropped
26. Inner trace mute (5 °)
27. Outer trace mute (40°)
28. Time variant bandpass filter
29. Phase-only Q compensation
30. Stacks full angle, near, middle and far angle
31. 10 trace 2D SNIP noise attenuation
32. Residual Gain
33. Amplitude scaling (1000 ms stable AGC
34. Gun and cable static (10 ms)

Final Deliverable
35. Migrate Final stacks
36. Raw Un-migrated Stacks

3.2.1 **Velocity Analysis**

The main processing differences between the PEG09 and RR1508 surveys involved the ability to more accurately constrain the velocities for the PEG09 data set. The long offsets of the survey (due to the 10,000 m streamer) allow for more accurate velocity analysis to be undertaken. The longer streamer also means that the fold (the number of traces in each CDP bin) is much higher. This means there are more traces to analyse, at a larger variety of offsets, allowing for a more accurate velocity analysis (Hyndman and Spence, 1992 ; Yilmaz, 2001).

By having a better control on the velocities, several of the other velocity reliant processes become more effective. Processes such as NMO or migrations become more effective, resulting in better stacking and noise mitigation (Yilmaz, 2001). While the offsets found in the RR1508 survey do allow for velocity analysis, the results have a lower accuracy and thus cannot be used as effectively as those based on long-offset velocity analysis (Figure 3.2).

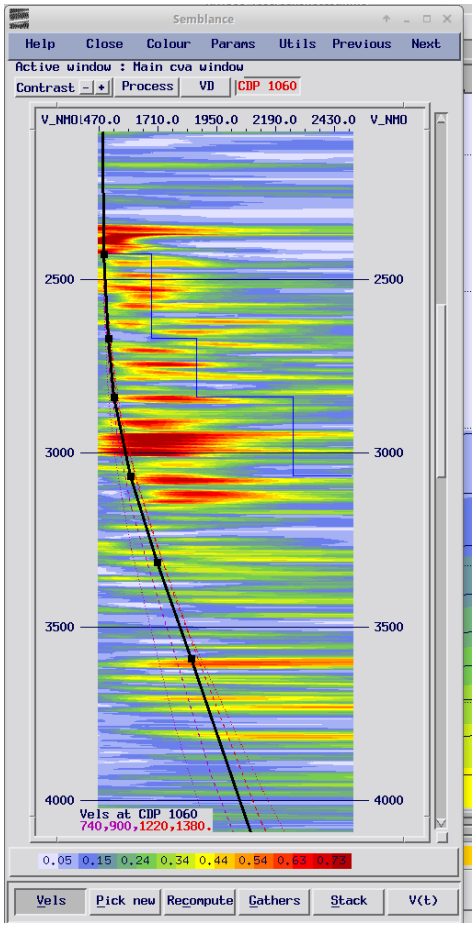

Figure 3.2 Example of semblance spectra from CDP 1060 on line from RR1508. The spectra illustrate the poor velocity control as seen by the widely dispersed 'bullseyes'.

3.2.2 **Trace Editing**

One processing module used on the PEG09 seismic lines that was not required in the RR1508 processing flow is trace editing (Table 3.2). The trace editing process identifies energy spikes and removes them. These energy spikes, if not removed, can be migrated and interfere with real reflections (Anderson and McMechan, 1989). The RR1508 data set did not require this trace editing as there were very few energy spikes recorded, most likely due to the shorter streamer and lower energy seismic system. While trace editing can be helpful, the removal process is controlled by user-determined amplitude thresholds, creating the possibility of accidental removal of energy from real reflections. As a result, it is preferred if the processing step is not required, particularly with lower fold data.

3.2.3 **Frequency Domain Filtering**

The frequencies emitted by the sound sources from the two survey types varied considerably. The high-frequency sound sources used during the high-resolution survey have a much wider range and as a result frequency domain filtering is performed to restrict the data to a more useful range. The 20 - >450 Hz range of frequencies produced by the GI guns is a large range, but the upper frequencies are too high to allow for good reflections in the 1500 – 2000 m water depth the survey was conducted in. As a result, a band pass filter was applied (Figure 3.4). The filter uses four user-determined corner frequencies to create a trapezoidal shape in the frequency domain, outside of which the frequencies are filtered out (Ravens, 1995). The corner frequencies used for the RR1508 data were 12, 35, 160, and 210 Hz, (A in Figure 3.3). These were determined via trial and error and by examining the frequency spectra (Figure 3.4). The filtering of higher frequencies also reduces the amount of noise by removing frequencies that are similar to those produced by engine noise and other anthropogenic and natural sources.

The filter used is different from the filter used in the processing of the PEG09 data, where a low-cut filter of 2 Hz/ -6 db/octave and a high-cut filter at 90 Hz/-72 db/octave were applied (B and C in Figure 3.3) (Yilmaz, 2001). The filters differ due to the differences in the sound sources used requiring that different frequencies are isolated.

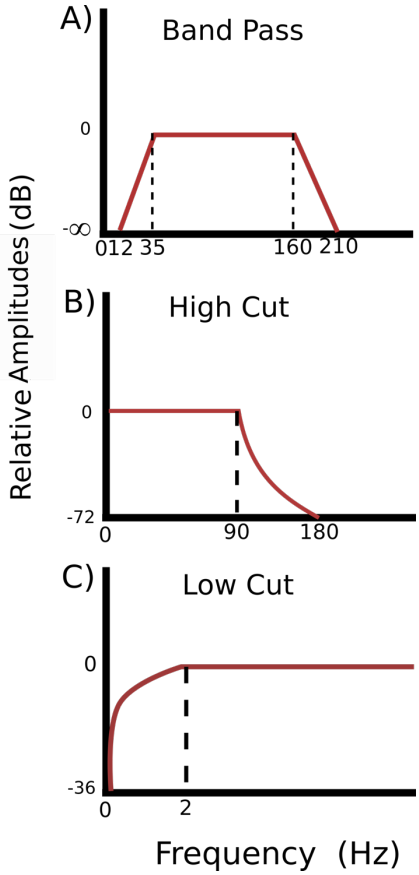

Figure 3.3 Three different filters used throughout the processing flow. The band pass filter (A) was used to filter the RR1508 seismic data, while the high and low cut filters (B and C) were used on the PEG 09 data.

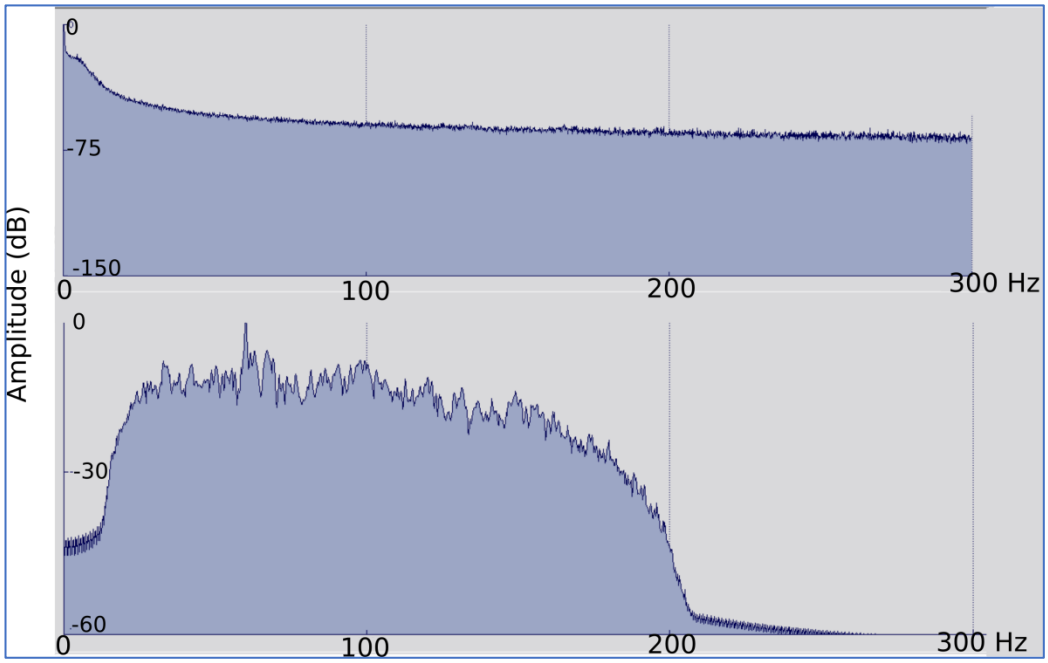

Figure 3.4 The frequency spectra from RR1508 Line 10 before (top) and after (bottom) the FDFilt of (12, 35, 160, and 210 Hz) has been applied. Note that the amplitudes in the two plots are relative to the respective maxima, so cannot be compared directly.

3.2.4 **Demultiple**

The increased penetration associated with the low-resolution survey does have associated issues. The first problem is the interference with primary reflections by multiples. In the RR1508 data sets, penetration of the high-frequency sound is limited to less than 3000 m (Figure 3.6). These depths are still well above the first occurrences of the seafloor multiples, which appear over 4000 m into the seismic sections. In the PEG09 survey, the multiples occur at similar two-way travel times; however, the increased penetration of the low-frequency data means these multiples overlay primary interpretable reflections. To remove these multiples, a radon demultiple processing routine is used (Cao, 2006). The radon demultiple job is also used to remove 'ghosts'. The 'ghosts' are caused by sound travelling from the airguns up to the surface first, before reflecting down towards the seafloor and subsurface. These ghosts are much more prevalent in the PEG09 seismic lines due to the streamer being towed deeper beneath the sea surface, as well as the lower frequencies used (Jovanovich et al., 1983). Both of these survey characteristics mean 'ghosts' are more obvious and obscure real reflections.

3.3 Comparing the Two Surveys

After the seismic data were run through their own individual processing flows, different features were highlighted.

3.3.1 **Penetration**

The most obvious difference between the PEG09 and the RR1508 seismic lines is the depth of penetration of the sound. The high-frequency RR1508 lines show minimal reflections at depths greater than 1500 m beneath the seafloor (Figure 3.6). The high-frequency sound waves used in the high-resolution survey attenuate much more quickly due to their shorter wave lengths (Figure 3.5) (Parkes and Hatton, 1986). The dissipation of energy is controlled by the medium the wave is propagating through. The energy loss is the same per cycle no matter the frequency of the wave. As a result, the amount of energy lost for the same distance penetrated is greater for higher frequency waves. Due to this energy loss, the high-frequency waves can only penetrate a relatively short distance into the Earth's surface before too much energy has been lost and the reflections are too weak to be recorded by the hydrophones (Yilmaz, 2001). The lower frequency waves produced by the PEG09 seismic survey have larger wavelengths (Figure 3.5) and thus attenuate more slowly and can reach further into the

subsurface. The PEG09 survey imaged features over 5000 m below the surface. The typical rate of attenuation is 0.2 db/wavelength in a medium with a velocity of 1500 m/s. A wave with a frequency of 30 Hz loses about 0.2 db per 50 m in comparison with a 100 Hz wave which loses 0.2 db every 15 m. Based on these attenuation rates, an amplitude drop of about 20 db renders the reflections invisible to the eye (Tullos and Reid, 1969).

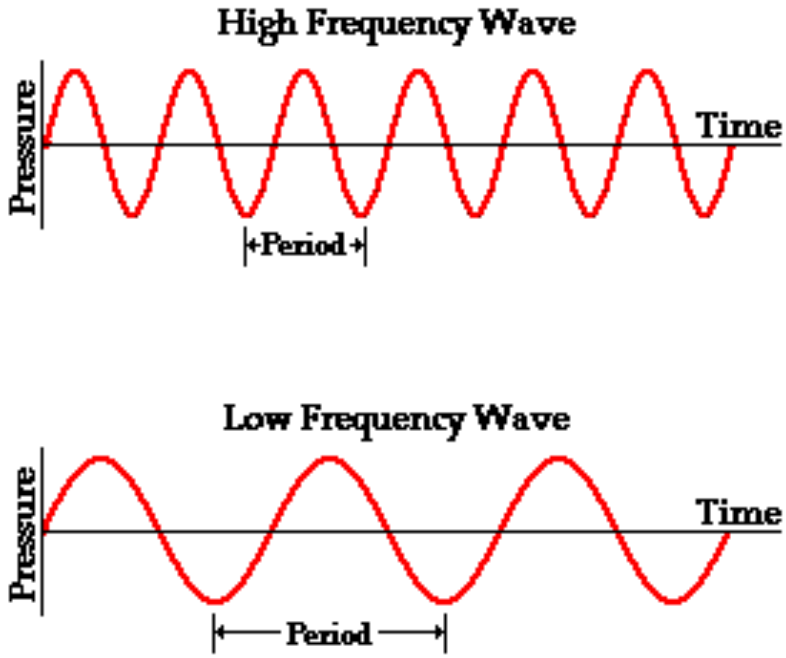

Figure 3.5 Diagram showing the difference in travel paths of high and low frequency sound (Physics Class Room, 2016).

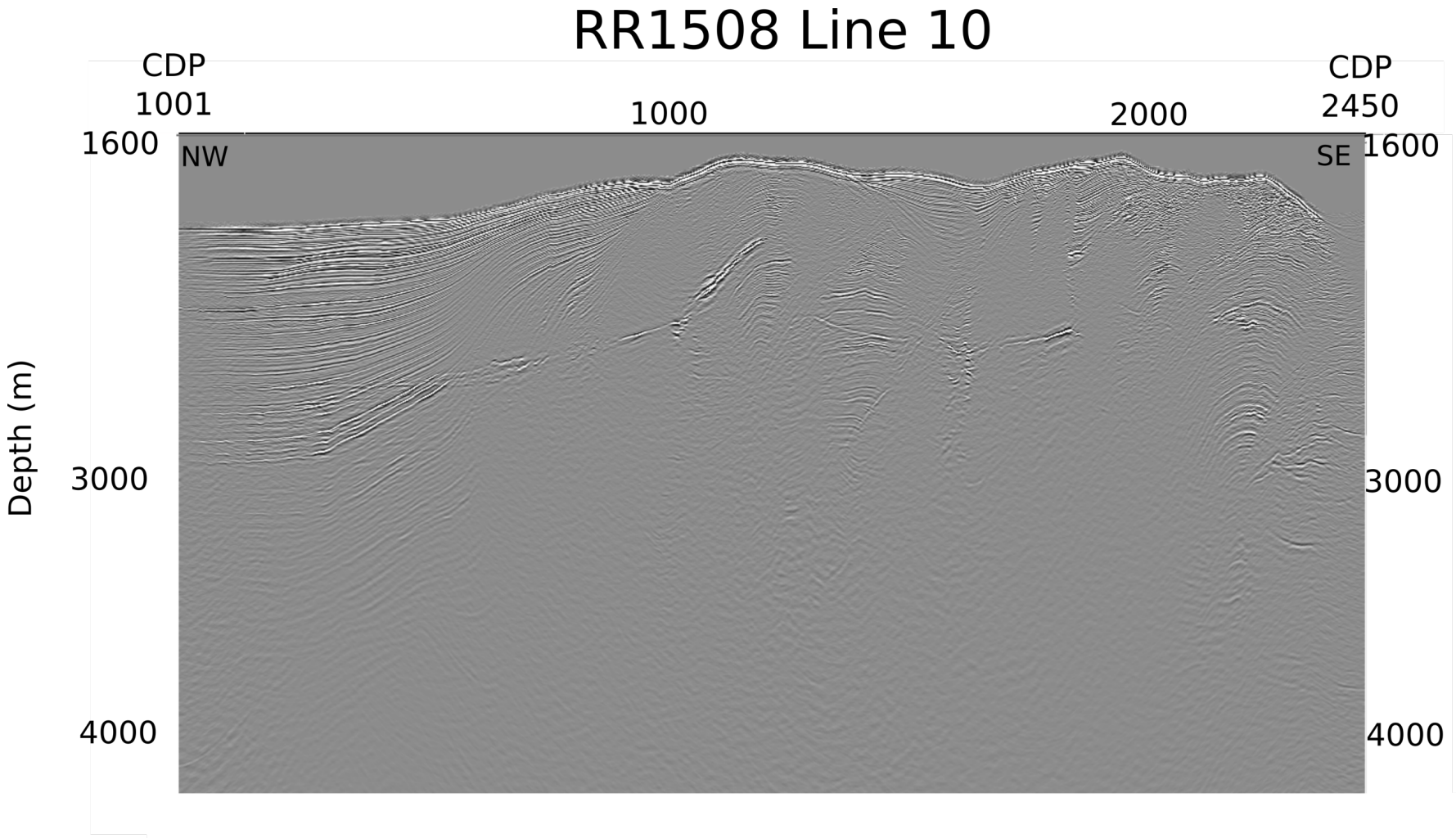

Figure 3.6 Line 10 from the RR1508 survey. The depth-converted seismic line shows the full depth of penetration (> 3000 m). CDP spacing is 6.25 m)

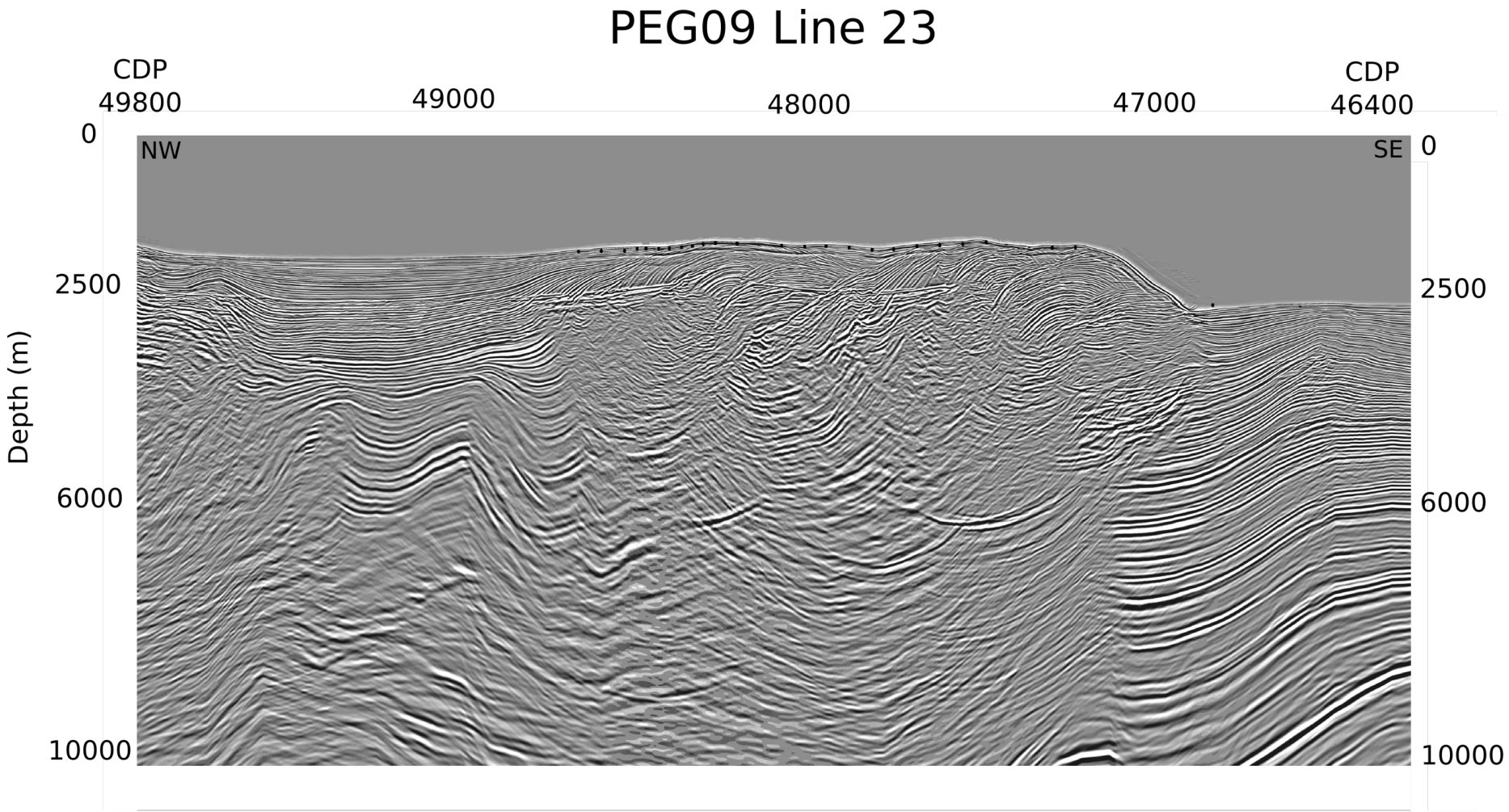

Figure 3.7 The section of Line 23 from the PEG09 survey which overlaps (CDPs 47000 to 48000) with Line 10 from the RR1508 survey. The depth converted seismic line shows the full depth of penetration (5000-10000 m). CDP spacing is 6.25 m.

3.3.2 **Resolution**

In the RR1508 seismic lines, the most noticeable difference as a result of the increased resolution is the ability to identify thinner beds in the near surface. The accretionary wedge structures and small sedimentary accumulations at topographic lows are imaged in greater detail and a larger number of thin beds can be identified in comparison to the PEG09 seismic data (Figure 3.8) (Morton-Thompson and Woods, 1993).

Seismic resolution defines the minimum size at which a disturbance will be visible in a seismic data set. Seismic resolution is controlled by both the vertical and horizontal resolution of the seismic survey. The vertical resolution is generally defined as being equal to a quarter of the wavelength ($\lambda/4$); although in some instances disturbances can be detectable up to $\lambda/32$. $\lambda/4$ is the most commonly accepted limit for vertical resolution (Yilmaz, 2001).

The horizontal resolution is controlled by the Fresnel Zone, which represents the phase shift of a sine wave deflecting off an object within the zone. Horizontally resolvable features are those that are wider than the Fresnel Zone. The Fresnel Zone is calculated using Equation 3.1 (Yilmaz, 2001).

$$r = \left(\frac{v}{2}\right)\sqrt{\frac{t_0}{f}} \tag{3.1}$$

r= Radius of the Fresnel Zone
v=Velocity
t_0=Time
f= Dominant Frequency

Due to the time component in the determination of the Fresnel Zone, the lateral resolution decreases with depth and is variable along a seismic line.

In the PEG09 survey only thicker units and features can be identified. The PEG09 survey used sound sources with a frequency range of 2 – 150 Hz and a dominant frequency of about 50 Hz. These frequencies result in a dominant wavelength of ~32 m assuming a velocity of 1575 m/s, limiting the vertical resolution to features greater than 8 m thick. Some thinner features can be identified but are often inaccurate and only sometimes imaged (Figure 3.9). The higher resolution data sets used frequencies ranging between 20 and 450 Hz with a dominant frequency of about 110 Hz. This gives a dominant wavelength of about 13 m and a vertical resolution of about 4 m. This increase in resolution allows imaging of much finer bedding and identification of smaller subsurface features (Figure 3.8) (Childs et al., 2000).

Using the Fresnel Zone equation (equation 3.1), with a velocity of 1575 m/s, at a TWT of 3.1 seconds and a dominant frequency of 110 Hz, a Fresnel Zone radius of 132.2 m for the high resolution RR1508 survey can be calculated. The difference in lateral resolution is evident when compared with the 620 m Fresnel Zone radius for the much lower resolution PEG09 survey, using a 50 Hz dominant wavelength (Yilmaz, 2001).

This increase in resolution also allows for improved imaging of discontinuous features or interruptions in bedding. Features such as faulting, disruptions of the BSR or other smaller scale features are much more apparent in the high-resolution RR1508 data sets (Knapp and Anderson, 1995). The imaging of these features results in more discontinuous reflections. These breaks in the reflections become quite an apparent difference between the RR1508 and PEG09 data sets (Figure 3.9 and Figure 3.8) (Trabant, 1942).

Another feature that is evident in the RR1508 data set but not the PEG09 data sets is lateral amplitude variation. These variations appear to be due to a combination of poor localised penetration or localised pockets of gas (Fader, 1997). While some of the larger pockets of gas are evident, if the amplitude loss is only minor then it is often not recorded by the lower resolution data (Figure 3.9). The longer wavelengths of the low-resolution data also counteract these localised zones of no penetration, so these also are not imaged.

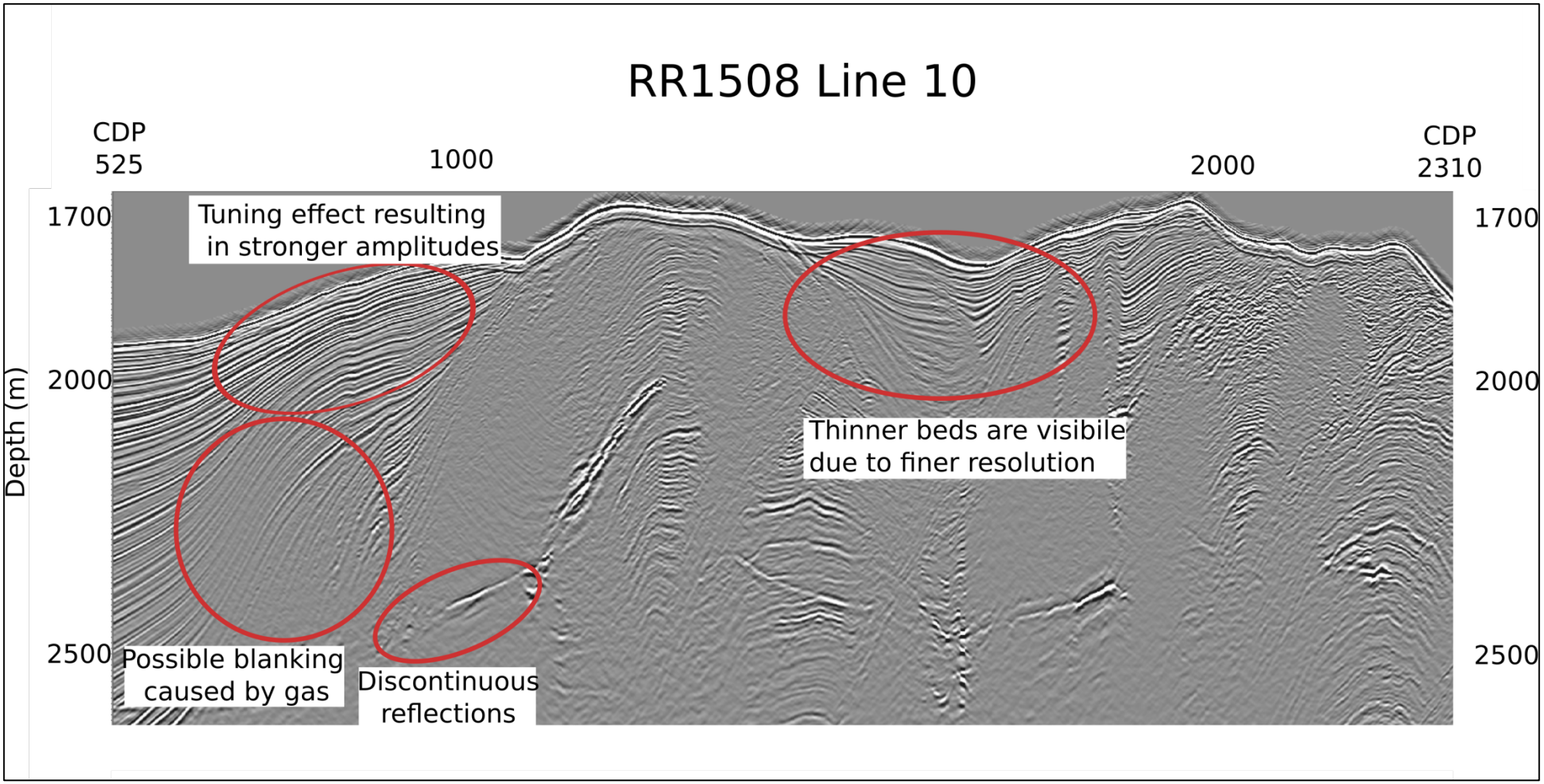

Figure 3.8 Line 10 from the RR1508 survey. The specific features of the survey that contrast those of PEG09 have been circled and annotated (cf. Figure 3.10)

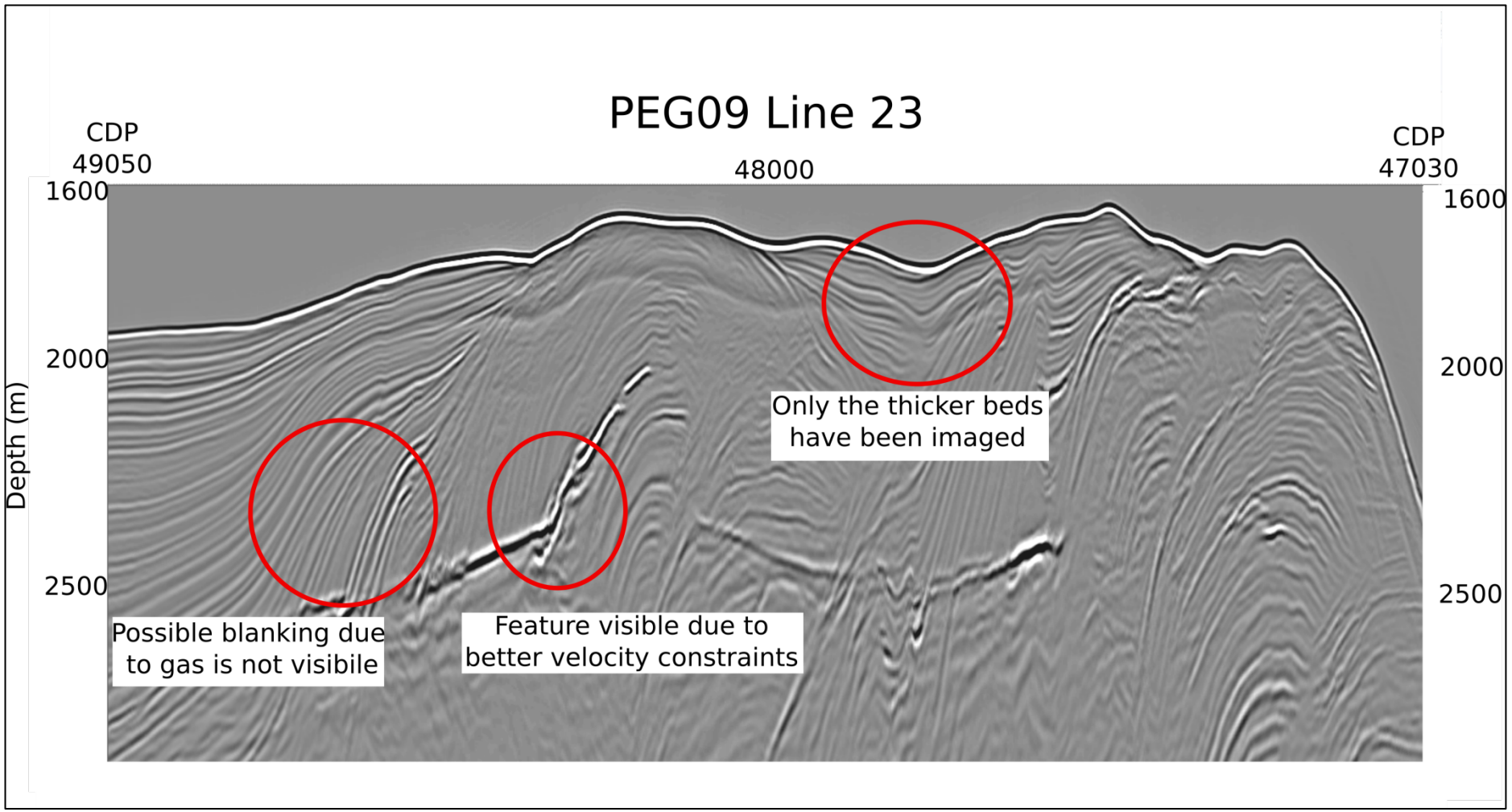

Figure 3.9 Line 23 from the PEG09 survey. The differences between the RR1508 survey have been circled and annotated. The lateral extents of RR1508 is identified by the 2 red lines (cf.Figure 3.8)

3.3.3 **Determinations of Stacking Velocities**

One considerable advantage of the PEG09 data set is the 10-km-long hydrophone array used to collect the data. The reduced rate of attenuation of the long wavelengths means a much longer streamer can be used with a lower frequency, higher energy source. The 10 km streamer used in the survey allows for a greater fold of approximately 133 (Yilmaz, 2001). This increased fold means that velocity analysis is more accurate and can be undertaken to greater depths. Better velocity control means depth conversions are more accurate and the stacking and migrations done to the data during processing are often more effective. These improvements in the processing allowed previously unidentifiable features to become visible via improved stacking (Figure 3.9) (Yilmaz, 2001).

The velocity analysis of the PEG09 data set proved to be valuable when processing the RR1508 seismic lines. The velocity profile from PEG09 Line 23 was used to produce a more accurate velocity profile for Line 10 from the RR1508 survey. The CDPs in PEG 09 Line 23 were matched with the first and last CDPs of Line 10 and the velocity profile from between these CDPs was extracted and rescaled to match Line 10. These velocities where then applied to the high-resolution seismic line. The velocities from the accurate velocity profile used on Line 10 were then used to guide the velocity picking on the remaining parallel lines from the RR1508 survey. The parallel nature of the lines meant that expected velocities could be formulated and they could be used on the remaining lines in combination with normal velocity picking techniques.

3.3.4 **Continuity**

Reflections in the PEG09 seismic lines appear much more continuous than those in the RR1508 data. The lower resolution means smaller breaks in the bedding are not always imaged and as a result only the larger scale features show up (Nanda, 2016). This results in the appearance of long continuous reflections. This can be advantageous in some circumstances, as minor changes in reflectivity often show up as broken discontinuous reflections in the

high-resolution seismic data, making it difficult to follow horizons. These continuous reflections are useful when trying to identify the BSR as an isotherm; however, they can be

misrepresentative of the BSR if volume or distribution calculations are being made (Nanda, 2016). This discontinuous nature can sometimes represent real features such as faults. In these cases, the continuity in the low-frequency data can be misleading and result in poor interpretations. Observations of continuity are tightly linked to resolution, so the ability to image stratigraphic and structural details of these breaks decreases with depth.

3.3.5 **Signal-to-Noise Ratios**

The signal-to-noise ratio of the data is generally lower for low-resolution surveys due to the most common sources of noise emitting lower frequencies. The most common source of noise in these data sets is swell noise. Swell noise is high amplitude and has a frequency that ranges between 1 and 20 Hz (Tamunobereton-Ari et al., 2015). This frequency sits right in the frequency range of the low-resolution data. This can result in difficulties when trying to filter out the noise (Tamunobereton-Ari et al., 2015). In contrast, the RR1508 data are impacted more severely by higher frequency noise such as engine noise. This higher frequency noise, however, is easily filtered out, as it is mostly at a frequency higher than those used in the high-resolution surveys.

3.4 Interpretational differences

The increased resolution and differences in the interactions between sound waves and reflectors can lead to some significant differences in the interpretations of the high- and low-frequency seismic data.

3.4.1 **Thin Beds**

Thin beds may be mis-interpreted at lower frequencies due to destructive interference between the upper and lower surfaces of the bed (Knapp and Anderson, 1995). When the bed is approximately ¼ of the dominant seismic wavelength, this destructive interference, or tuning, is the greatest (Figure 3.10) (Zeng, 2013). At higher frequencies, the tuning thickness required to cause this effect is smaller. Therefore, there may be sufficient distance to separate the upper and lower surfaces of a bed that was ‘tuned’ in the low-frequency data. As a result, the amplitude response for a thick bed can be double that of a thin bed (Widess, 1973). This results in the amplitude response being strongest at the tuning thickness, so thinner beds can

be better imaged with high-resolution surveys but thicker beds are better imaged by lower frequencies (Knapp and Anderson, 1995).

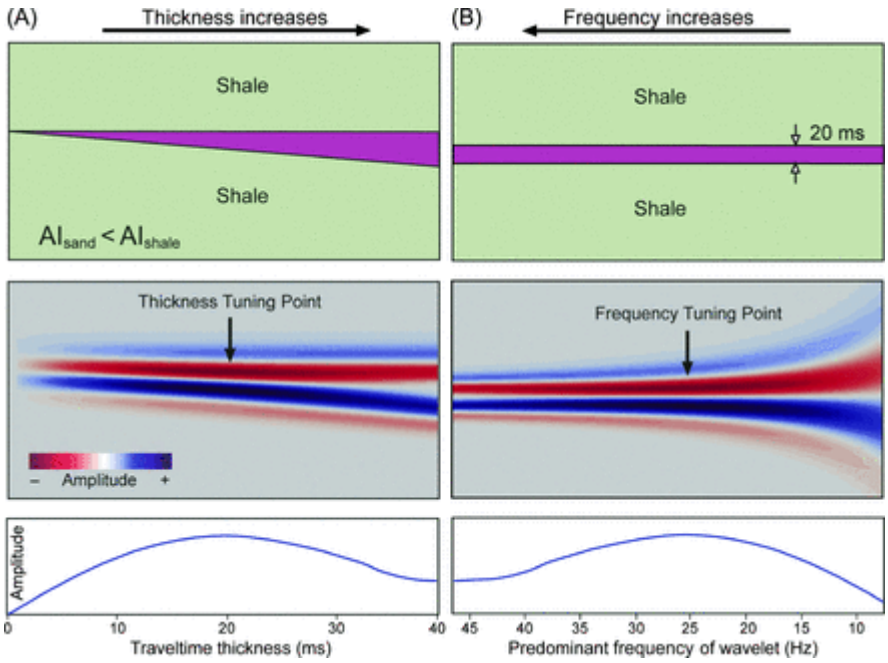

Figure 3.10 Example illustrating the effect of wavelength approaching the tuning point and its effect on amplitudes (Zeng, 2013).

This tuning is visible in the RR1508 seismic lines (Figure 3.8). The shorter wavelengths of the survey result in an increase in amplitude in bedding in comparison with the PEG09 survey where the wavelengths are longer than the tuning thickness (Yilmaz, 2001).

3.4.2 **Acoustic Impedance Gradients**

If a wavelength is longer than the thickness of a geological unit that contains an impedance gradient, then the seismic wave will not be affected by the gradient. If the frequency decreases, then the wavelet broadens and the event appears to have both a lower frequency and a lower amplitude. If the higher frequencies increase, then the reflections within the zone can cancel out, leaving only the edges of the zone visible and eventually becoming effectively invisible (Knapp and Anderson, 1995). As a result, these gradients will appear stronger on conventional lower resolution data sets compared with higher resolution data sets. Impedance gradients in this region can be associated with gas pockets where there is a gradual increase in gas concentration.

3.4.3 **Lateral Rugosity**

The ability to image lateral rugosity (horizontal undulations within the seismic data) is strongly controlled by the lateral resolution of the seismic data set, which in turn depends on the lateral extent of the wavelet (Claerbout, 1986). As mentioned previously, this lateral component of resolution is controlled by the Fresnel Zone Width. The higher the frequency, the smaller the Fresnel Radius, so as a result the higher frequency data are more sensitive to lateral rugosity. A feature showing short-wavelength, low-amplitude rugosity may appear continuous in low-resolution data and then be more intermittent in high-resolution data (Knapp and Anderson, 1995).

3.5 Summary

The comparison between the high-resolution (RR1508) and conventional (PEG09) seismic datasets clearly highlights some major differences. The high-resolution data, as expected, were better at imaging structures and bedding in the near surface, while for imaging depths greater than 1500 m, conventional seismic data were superior. The conventional data were more useful for following and identifying large continuous structures, even in the near surface, due to the lower resolution creating more continuous reflections and not imaging smaller breaks or discontinuities. Accurate volumetric analysis or detail orientated interpretations were more successful with the high-resolution data as all the breaks and discontinuities were visible. The comparisons also highlight tuning effects that vary with wavelength and are dependent on the size of geological structures. This comparison really emphasised the importance of matching the frequency spectra used in the surveys to the specific survey targets.

4 Seismic Results and Interpretations

4.1 Introduction

The high-resolution seismic data presented in this thesis allows for a detailed insight into the subsurface, to gain a better understanding of the lithologies and gas hydrate and fluid flow dynamics (Cooper and Hart, 2003). The seismic reflections alone help to increase our understanding of the structure of the subsurface and allow for improved interpretations of the nearby heat flow observations.

4.2 Observations and Results

There are a variety of elements within the seismic data that can be observed and described based on their physical characteristics without invoking geological interpretations. The first and most obvious observation is made concerning the two-way travel times (TWTs) of the reflections, which indicate the relative position of a variety of reflectors (Herron and Latimer, 2011). These reflections in the seismic data also have amplitude values which are directly related to the strength of the impedance contrasts, as well as polarities which indicates the nature of the impedance contrast i.e. from high to low or low to high (Yilmaz, 2001). The final observations made are consistent with the velocity profiles of each line. The velocities are picked by examining the CDP gathers to identify where the most energy stacks. (Chapter 2.1.1.7; Yilmaz, 2001). These velocities can tell us a lot about the medium through which the sound is travelling.

4.2.1 **Seismic Reflections**

4.2.1.1 Overall Reflection Distribution

The parallel distribution of the lines means most linear features that run along the ridge are seen in all lines, so changes between lines can tell us something about the 3D structure of the region.

Reflections found in the RR1508 data set are fairly localised. The main package of reflectivity is a dense unit of horizontal reflections found on the north-western end of the lines. A smaller package of similar sub-parallel reflections is also found half-way across the lines and up to about 200 ms below the initial reflection. Apart from these two occurrences, reflections are fairly limited. There is a single continuous reflection found 400 – 700 ms beneath the initial reflections which can be identified in certain portions of all the lines. There

are also occasional minor zones of fairly chaotic reflectivity scattered throughout the sections.

4.2.1.2 Seafloor Reflections

The first strong reflection, identified as the seafloor in all of the seismic lines, runs across the seismic data at a TWT of 2000 – 2700 ms. This seafloor reflection undulates northwest to southeast in all of the lines. The reflection gradually steepens and the TWT decreases eastward across the line. A third of the way across the line, a peak shape is formed and the TWT begins to increase southeastward. This TWT increase continues across the rest of the lines along with several undulations present along the eastern half of the line. The first undulation forms a basin-like shape where the reflection suddenly trends upwards. At the south-eastern end of several of the lines, a steep increase in TWTs can be seen, where the reflection exhibits a steep drop off (Figure 4.1).

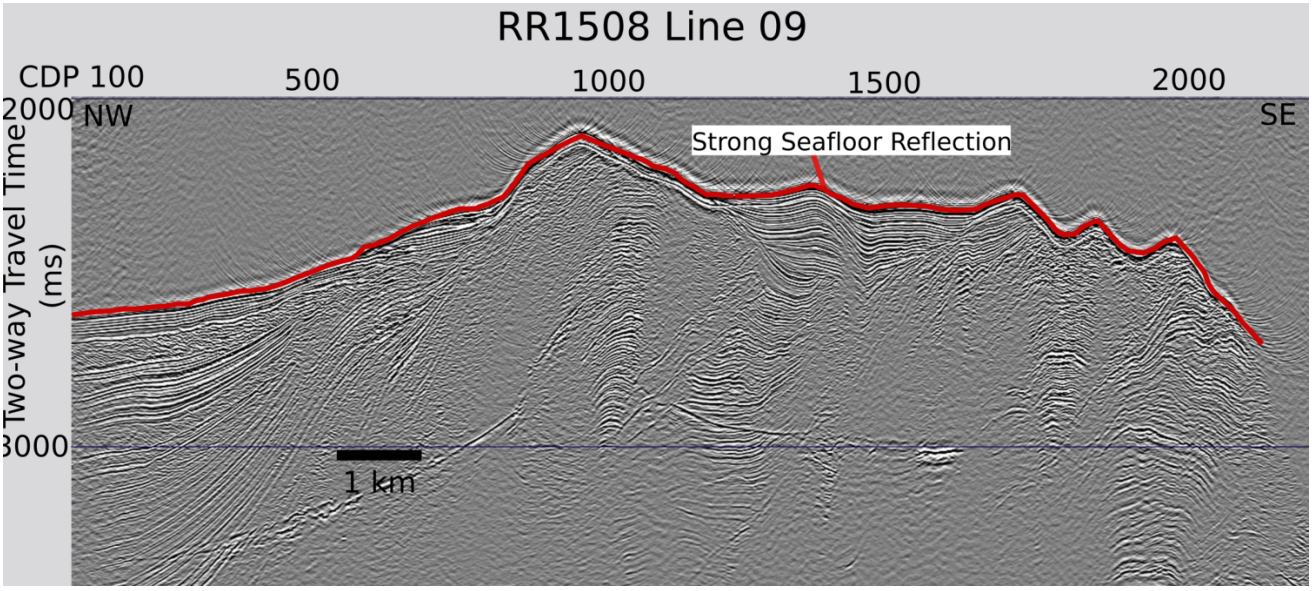

Figure 4.1 Line 09 from the RR1508 survey with the strong seafloor reflection annotated in red.

4.2.1.3 Western Package of Sub-Parallel Reflections

At the northwestern end of the lines, a wedge-shaped package with numerous reflections distributed at a fine spacing throughout the unit is clearly visible (Figure 4.2). This unit thins south-eastward along the line with the TWT of the deepest reflections from this unit starting out at 3700 ms and decreasing up to 2400 ms in lines 9 and 10, where the feature thins to nothing (Figure 4.2). In lines 11, 12 and 13A this same group of reflections do not thin out and remain several 100 ms thick connecting with a similar unit further along the line (Figure 4.3). In all lines, the unit exhibits a dense collection of sub-parallel reflections. Halfway through this package the reflections lose their horizontal orientation and begin to develop a dip, towards the northwest. The dip at the base of the package is parallel to the contact between the package and the underlying unit. In the uppermost 300 ms or so, the reflections also terminate at the contact between the units in an onlapping fashion.

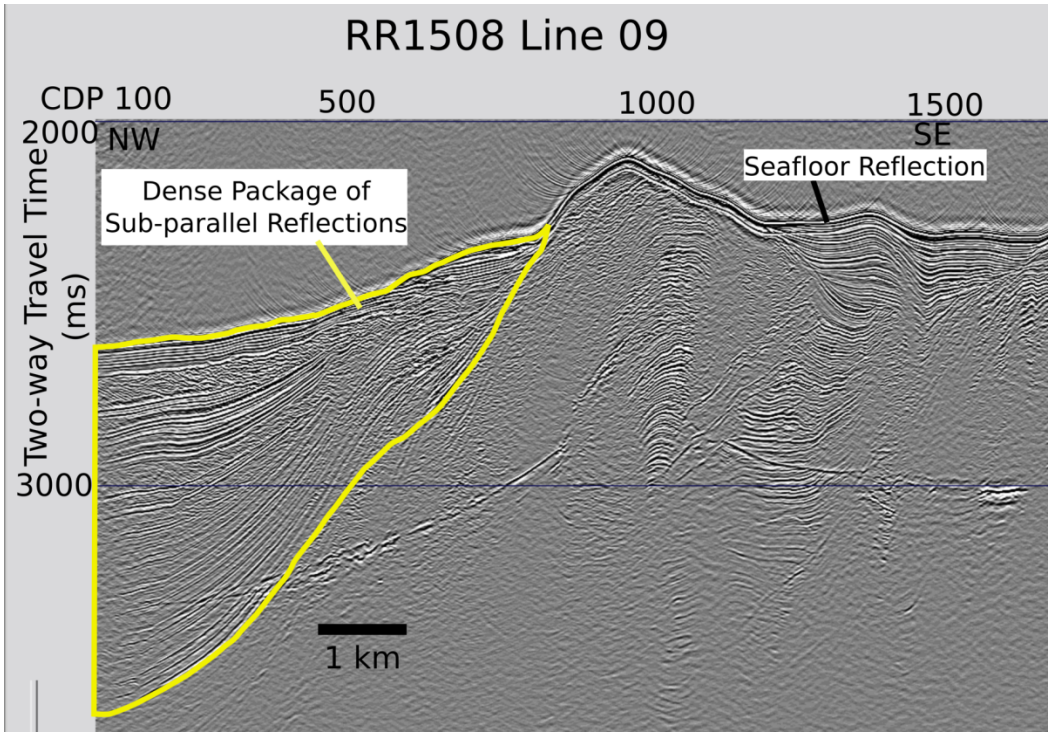

Figure 4.2 Line 09 from the RR1508 survey, with a package of sub-parallel reflections outlined. The seismic line shows the package terminating about a third of the way along the line travelling from the NW.

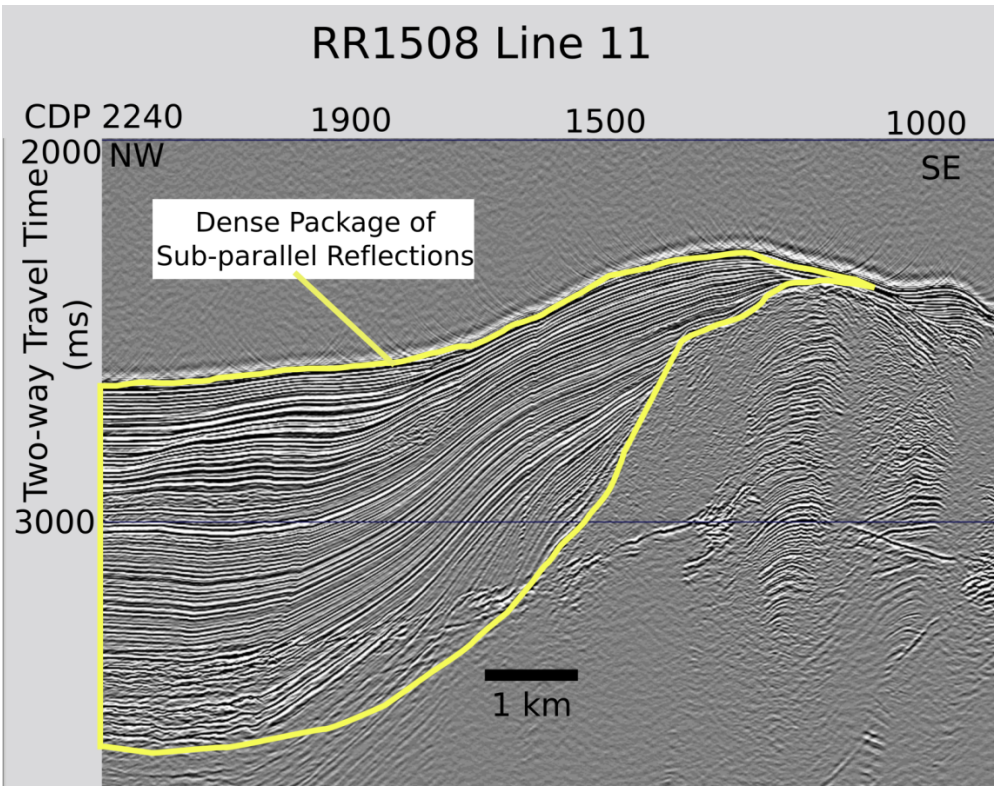

Figure 4.3 Line 11 from the RR1508 survey, with the package of sub-parallel reflections outlined. The seismic line shows the package terminating about half-way along the line travelling from the NW at a lower two-way travel time than in Line 09.

4.2.1.4 Basin Shaped Package of Parallel Reflections

8-10 km in from the north-western end of the RR1508 lines, a small V-shaped package of dense sub-parallel reflections, similar to those found on the north-western edge, is found. The package is thickest where the TWT of the initial reflections is greatest. On either side of this thick zone, the package tapers out (Figure 4.4). The base of the package is similar to that found in Line 9, where the reflections lose their horizontal orientation with depth. The reflections also terminate against the contact producing an onlapping shape to the package.

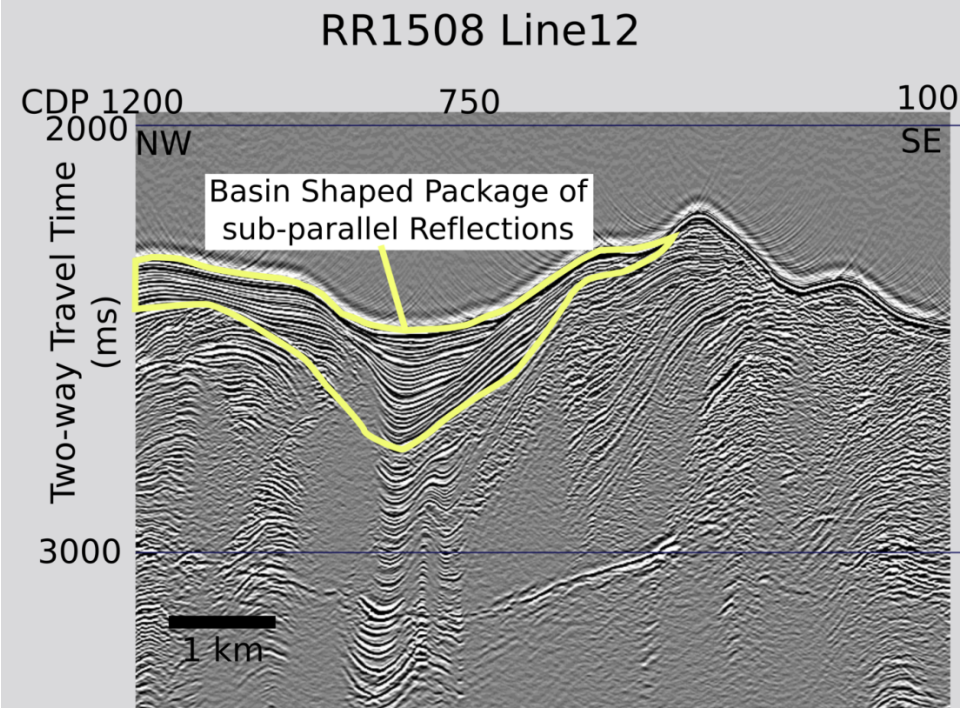

Figure 4.4 Line 12 from the RR1508 survey. Outlined in yellow is the package of sub-parallel reflection in a basin shape.

4.2.1.5 Sub-seafloor Reflections

Along the eastern two-thirds of lines 9 and 10, the region 300-500 ms beneath the seafloor reflection has a patchy appearance. Once the unit with dense sub-parallel reflections has thinned, there are very few reflections immediately below the seafloor. The first instance of reflectivity in this zone is about half-way along the line, below the basin shaped reflections identified previously. Here, there are100 – 200 ms of dense sub-parallel reflections that are thickest at the centre of the basin-like feature. On the south-eastern side of this feature, beneath the undulations in the seafloor, there are erratic zones of noisy reflectivity. The reflections observed are not sub-parallel and appear to lack continuity. The localities of these zones are unpredictable and do not appear to relate to any seafloor features.

In lines 11, 12, and 13A, the upper 300 ms beneath the seafloor reflection is mostly a dense collection of sub-parallel reflections, very similar to those described on the north-western edge of the lines (Figure 4.3).

4.2.1.6 Continuous Single Reflection at Depth

In all lines a linear reflection can be observed between 400 and 700 ms beneath the seafloor. Each reflection appears to be relatively continuous, although the reflection disappears for sections in all lines (Figure 4.5). These reflections are sub-horizontal apart from a few exceptions. When found amongst other reflections, the continuous linear reflection is seen to cross-cut. The TWT between the reflection and the seafloor reflection appears to be fairly constant across all lines, except for a third of the way along the lines from the northwest, where the TWT of the reflection suddenly decreases and the reflection gets closer to the seafloor reflection. The general trend of this reflection is similar in all lines.

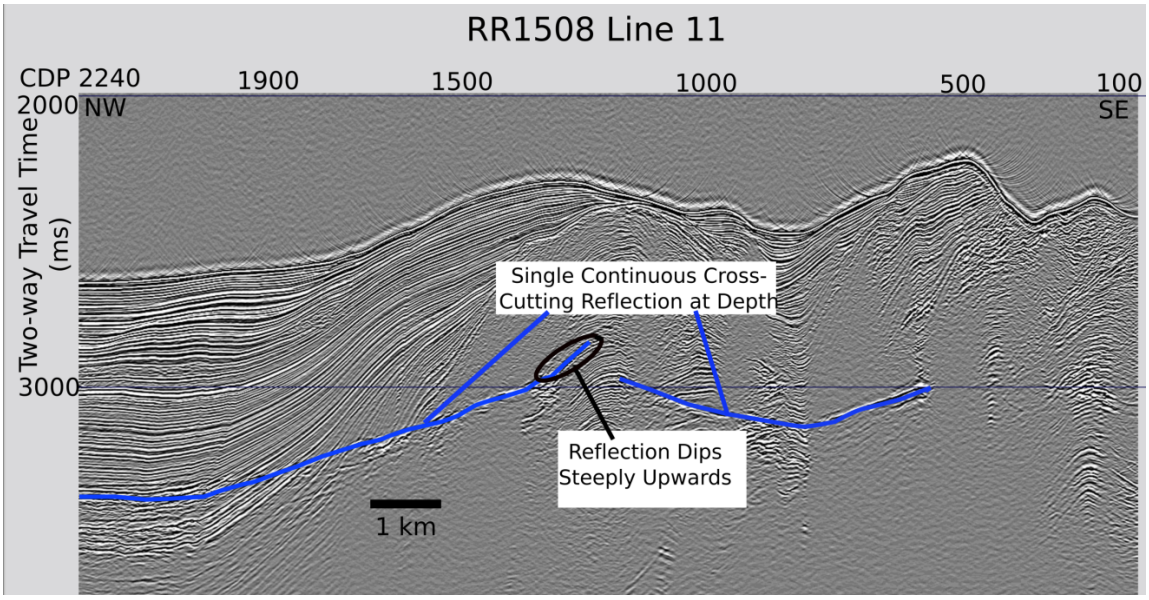

Figure 4.5 Line 11 from the RR1508 survey with the strong continuous reflection at depth in blue.

4.2.1.7 Absence of Reflections

In addition to the observable reflections, the lack of reflections can also tell us something about the subsurface geology. In RR1508, lines 9 – 13A, there are localised zones where there are very few reflections. The majority of these zones are found east of the sub-parallel wedge of reflections. Several zones with no reflectivity are found amongst these sub-parallel reflections. The majority of these 'blank' patches are laterally variable, these 'blank' zones stretch from just below the strong seafloor reflection deep into the subsurface, yet strong reflections can be seen only tens of metres away.

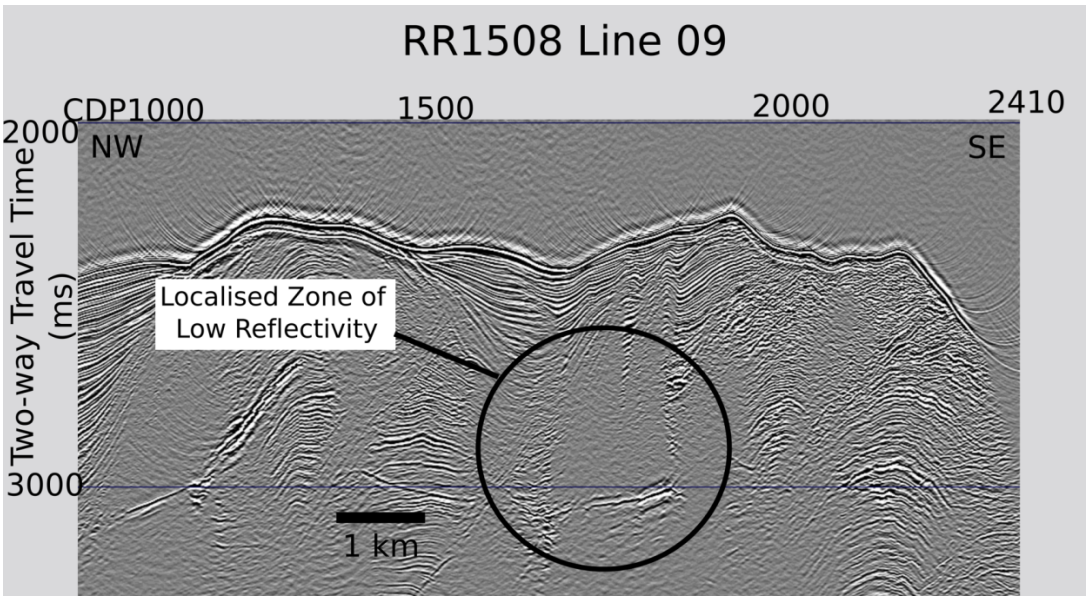

Figure 4.6 Line 09 from RR1508 with a localised zone of low amplitude circled.

4.2.1.8 Vertical Linear Disruptions

Vertical linear disruptions are evident in some of the seismic lines. These disruptions appear to be associated with regions of high reflectivity and vertical offsets in reflections. All of the linear features appear to dip at about 45°NW from the surface.

4.2.2 **Seismic Amplitudes**

As well as TWT, the amplitudes of the reflections contain information on the nature of the contacts between subsurface layers. The strongest amplitudes are found along the seafloor reflection; these amplitudes tend to decrease in strength as their TWT increases (Herron and Latimer, 2011). Amplitudes throughout the packages of sub-parallel reflections are relatively similar but do gradually weaken with depth. The amplitudes also remain fairly constant between similar packages from line to line.

The strong seafloor reflection has a positive amplitude response, a wavelet with a positive-negative-positive amplitude signal, corresponding to a boundary with a positive impedance contrast. The single strong continuous reflection located about 500 ms below the initial seafloor shows the opposite amplitude response in the form of a negative response (negative-positive-negative amplitude signal corresponding to a boundary with a negative impedance contrast.) (Figure 4.7). In limited areas, however, this single continuous reflection undergoes a polarity reversal. This reversal is best seen in Line 10 located along a single continuous reflection where it dips steeply and exhibits a decrease in TWT at CDP1200 (Figure 4.7).

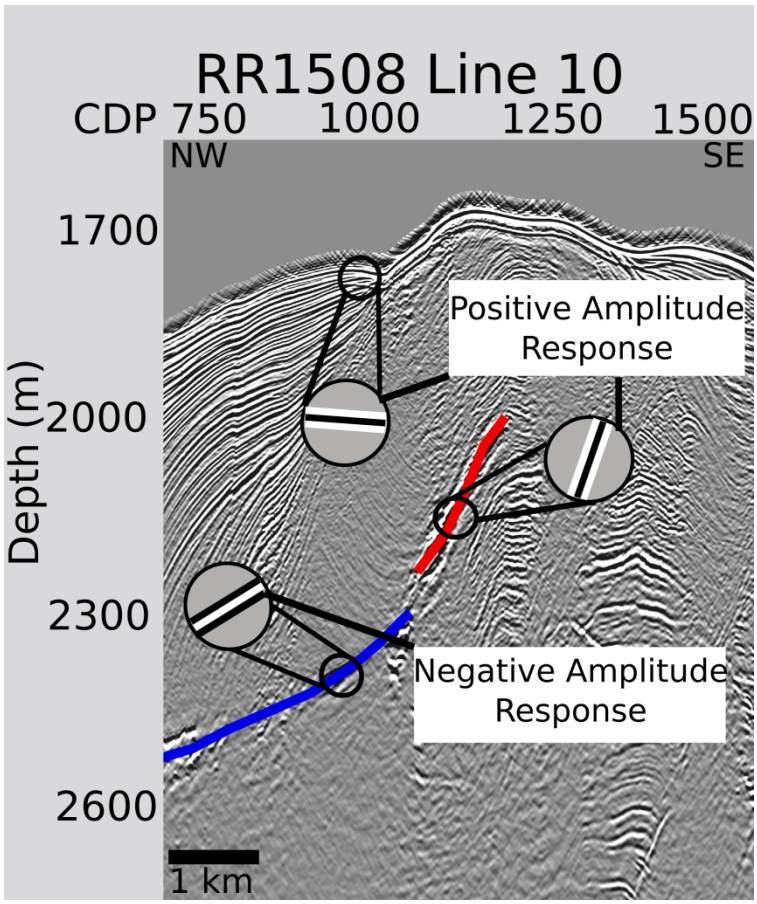

Figure 4.7 Depth-converted Line 10 of RR1508 with the polarity of the strong seafloor reflection, and two different polarities present on the strong continuous reflections at depth.

4.2.3 **Seismic Velocities**

Velocities picked during seismic processing show similar trends throughout all lines. The strong seafloor reflection in all lines had stacking velocities ranging between 1481 and 1500 m/s. The seismic data contained two different trends with depth. The regions of sub–parallel dense thin reflections increase in velocity with depth, increasing from ~1485 m/s to 1600 m/s at about 1000 ms beneath the seafloor. This increase was fairly constant both vertically and throughout areas with similar reflective patterns. The much less reflective regions in the seismic lines also showed increasing velocities with depth; however, they were far less uniform, partly because there were no or few events to analyse in these regions. Over a similar distance, the less reflective regions reached velocities of ~1675 m/s (

Figure 4.8). This shows a 50% increase in velocity at the same depth within several kilometres of each other.

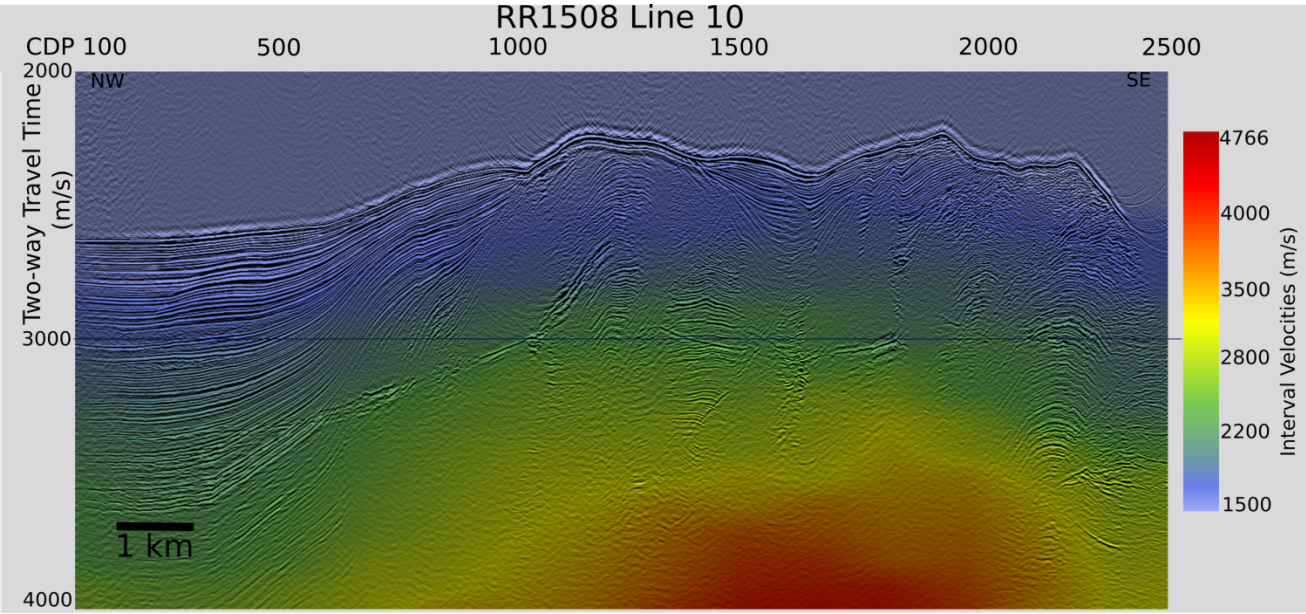

Figure 4.8 Velocity profile overlain on top of seismic Line 10 from the RR1508 survey.

4.3 Seismic Interpretations

Interpretation and analysis of the seismic observations made in Chapter 4.2 aim to explain the structures and features imaged in the sub-surface in the region. These interpretations allow us to gain an understanding of the sub-surface mechanics of the region, including possible fluid and hydrate movements or accumulations.

4.3.1 **Lithologies**

Previous studies in the Pegasus Basin region have suggested some possible lithologies and ages; however, without drill holes, any interpretations or identifications are speculative. The surface deposits imaged in RR1508 lines 09 – 13A have been interpreted as being Pliocene – Pleistocene in age with a siltstone-mudstone composition, through drilling of nearby basins and evaluation of their stratigraphic architecture (Bland et al., 2017; Kroeger et al., 2015).

The seismic lines all run across a ridge structure starting with dense decimetre-scale sub-parallel bedding prevalent up to 700 m beneath the surface. This bedded unit thins out to the southeast along the lines where a denser, presumably more lithified unit replaces it. This lithified unit has noticeably fewer internal reflections. The seafloor continues to shallow for a short distance until it peaks and then deepens again. As the seafloor deepens, the upper 200 m of the subsurface develops more sub-parallel dense bedding, forming a small basin. This basin then pinches out towards the surface where another lithified unit with some minor

internal structures undulates but still maintains an overall deepening trend south-eastward to the end of the lines (Figure 4.11).

This overall morphology is similar for lines 9 and 10; however, beginning in Line 10 and progressing through Line 12 the bedded unit extends further south-eastward. In the more southern lines the unit begins to drape over the high peak, leaving a 200 m thick bedded unit across the entire ridge. The south-eastern most portions of the seismic lines are all similar.

The seismic velocities of the various media are strongly controlled by the Newton-Laplace equation (Blackstock, 2000) as seen below in Equation 4.1.

$$Vp = \sqrt{\frac{K + 4/3(\mu)}{\rho}} \tag{4.1}$$

where:

$$Vp = P - Wave\ Velocity$$
$$K = Bulk\ Modulus$$
$$\mu = Shear\ Modulus$$
$$\rho = Density$$

This equation is important as it highlights the fact the relationship between P-wave velocity and density is indirect. Due to the density being in the denominator, any increases in density contribute to a decrease in P-wave velocity, the opposite of what is expected and observed in most cases. Density increases however, are almost always accompanied by an increase in pressure. It is this increase in pressure that controls the bulk and shear moduli which results in an overall P-wave velocity increase. This suggests that the differences in velocities between the bedded units and the relatively reflection-free units are due to changes in pressure as a result of lithological variations
Figure 4.8) (Schultz, 1998).

While P-wave velocity can tell us something about the pressure changes, the seismic images and the recorded reflections are strongly controlled by impedance contrasts. Impedance is controlled by Equation 4.2

$$Impedance = Vp * \rho \tag{4.2}$$

Strong reflections in the seismic data require strong impedance contrasts. The bedded units with their densely-packed reflections suggests the seafloor units imaged here are made up of well-defined discrete layers with very different densities and velocities. These strongly contrasting layers result in the strong reflections seen in the seismic data. On the other hand, the lack of internal reflections in the lower sedimentary unit suggests that either the bedding within the unit is finer than the resolution allowed by the survey and as a result is not imaged or the bedding lacks the impedance contrasts seen in the reflective units, resulting in a lack of reflected sound.

The bedded units are probably less lithified units, potentially with poorer sorting and thus more variable porosity. This combined with fine scale bedding with varying densities possibly indicates a siltstone/mudstone interbedded with clay. Without drilling, the lithology of the massive unit with only minor internal structures is very difficult to identify. The velocity profiles also support a siltstone/mudstone composition (
Figure *4.8*); however, any further interpretations are limited.

4.3.2 **Bottom Simulating Reflection (BSR)**

The strong reflection that can be seen about 400 – 500 ms below the seafloor is interpreted as a bottom simulating reflection (BSR). The reflection is identified as a BSR due to the way the reflection shadows the seafloor's bathymetric variations. Another key characteristic is the fact that the reflection will cross-cut other identified reflections (Figure 4.11) (Thakur and Rajput, 2011). The feature also has a negative amplitude response indicating a transition from a high velocity medium to a lower velocity medium. This response is characteristic of the transition between hydrate-bearing and gas-bearing sediments (Figure 4.7) (Chi et al., 1998).

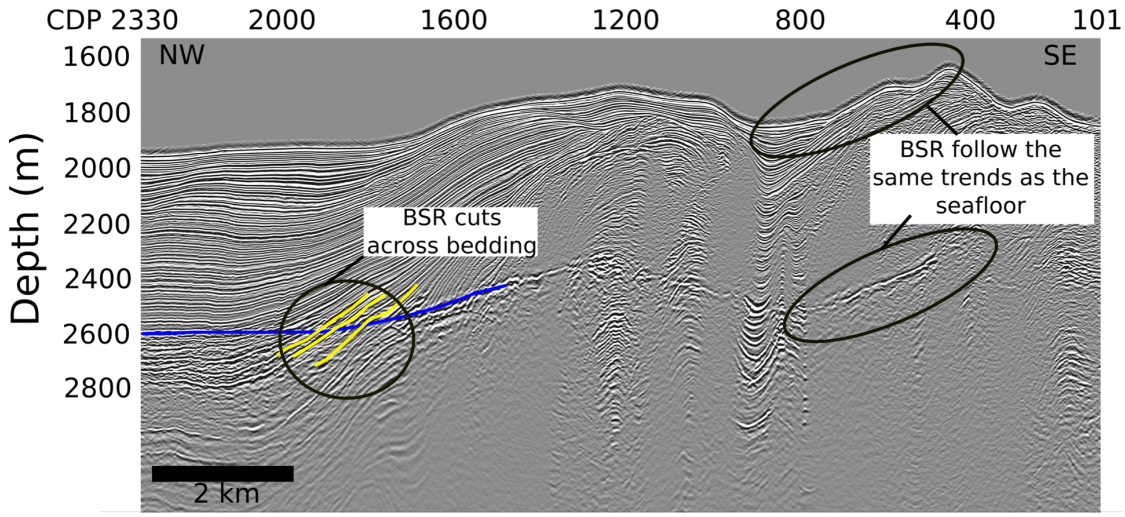

Figure 4.9 Depth-converted seismic Line 12 showing the characteristics of the BSR that allow its identification.

A BSR occurs at the interface between the zone of gas hydrate stability and a region of underlying gas-charged units, which is controlled by pressure and temperature as discussed in Chapter 1.4. Below the BSR, pore spaces cannot contain gas hydrate, whereas above the BSR pore spaces do contain hydrate. Due to the Newton-Laplace equation (Blackstock, 2000) the velocity of the medium decreases as a result of the presence of gas, resulting in a negative impedance contrast and a negative polarity reflection (Batzle and Wang, 1992).

The presence of gas hydrate can in places also explain the lack of reflectivity in apparently non-bedded units. If the pore spaces of a unit contain gas hydrate, this can create a more uniform impedance throughout the hydrate-bearing sediments because of the relatively high velocity and density of hydrate compared to other pore fluids (Fader, 1997). This uniformity disguises any structural impedance contrasts, producing the blank areas.

The BSR maintains a fairly consistent shape throughout the lines, imitating the shape of the seafloor and staying within 700 m of the seafloor. The BSR is not visible continuously throughout all the seismic lines. However, the appearance of the BSR is relatively constant where it is observed, likely due to regional controls promoting or inhibiting penetration of the sound. The BSR is visible through the sedimentary bedded units and then again beneath the small infilled basin. On either side of the basin in all lines the BSR becomes weak and can only be inferred. This loss of reflectivity may be due to the specific sedimentary units found in their region allowing a greater absorbance of sound and an increase in energy loss at the

surface. This is supported by the observation that seismic lines, that image sections of the ridge with more extensively bedded units across the surface, also show a more extensive BSR.

4.3.3 **Faulting**

Vertical disruptions in reflections also appear to be present throughout the seismic data. These angled linear vertical features result in offset bedding. These features are indicative of faults. The presence of faults throughout the seismic lines is expected due to the tectonic regime of the locality associated with the nearby subduction zone. The faults present throughout the seismic lines are mainly reverse faults with a dip average of 40 – 45°NW. This is similar to the major fault in the area, the Pahaua Fault (Litchfield et al., 2013). Faulting is also highlighted by the presence of high-amplitude reflections from the faults themselves, which localise fluid flow. Hydrate can form in the areas surrounding such faults in porous sediments causing increased amplitudes around the faults.

4.3.4 **Fluid Migration**

Areas of localised fluid flow are evident throughout the lines, particularly beneath the bathymetric high approximately 5 km in from the north-western edge of the seismic lines (Figure 4.11 and Figure 4.12). Fluid migration often occurs due to features such as a faults or the axes of folds that concentrate fluid migration along a distinct path (Ligtenberg, 2005). This fluid migration brings warm methane-rich fluids up through the sub-surface and into the zone of gas hydrate stability. This causes the formation of a zone of concentrated hydrate resulting in a high velocity zone that can be imaged by a seismic survey (Crutchley et al., 2015).

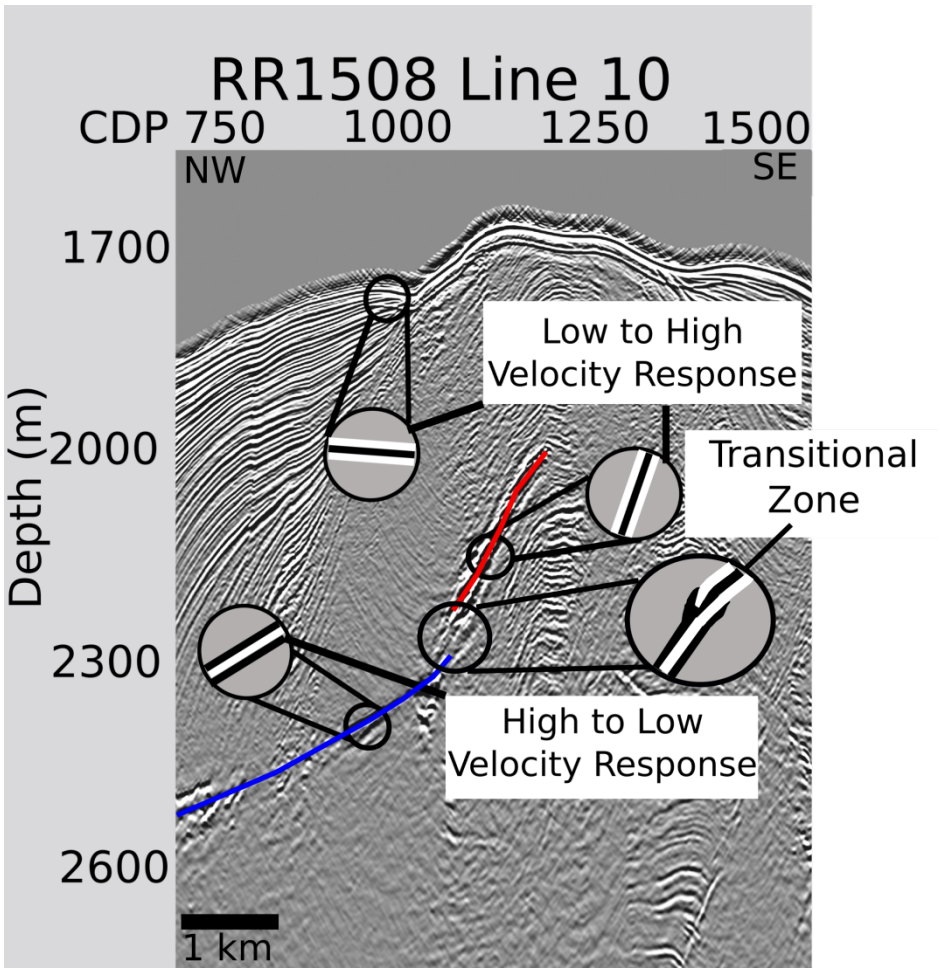

Figure 4.10 Polarities of specific features on Line 10 with the transition between the BSR and hydrate lens illustrated.

The main fluid migration feature, which is strongest in Line 10 but also visible in lines 9, 11 and 12, is identified by the positive polarity of the reflection. The negative response seen at the BSR transitions to a positive response just above the BSR. This shallowing reflection with its positive response indicates a zone of high velocity which is interpreted as a shallow zone of hydrate. Below the BSR, the negative response indicates a gas-charged layer.

Fluid localisation is possibly due to tectonic processes in the subsurface supported by the sudden termination of the reflection beneath the bathymetric high on the seafloor (Crutchley et al., 2013). The collection of fluid possibly due to a tectonic structure trapping the fluid results in a saturation of the pore space to the extent not all of the gas can exist as hydrate. This results in the change in seismic response across the feature,

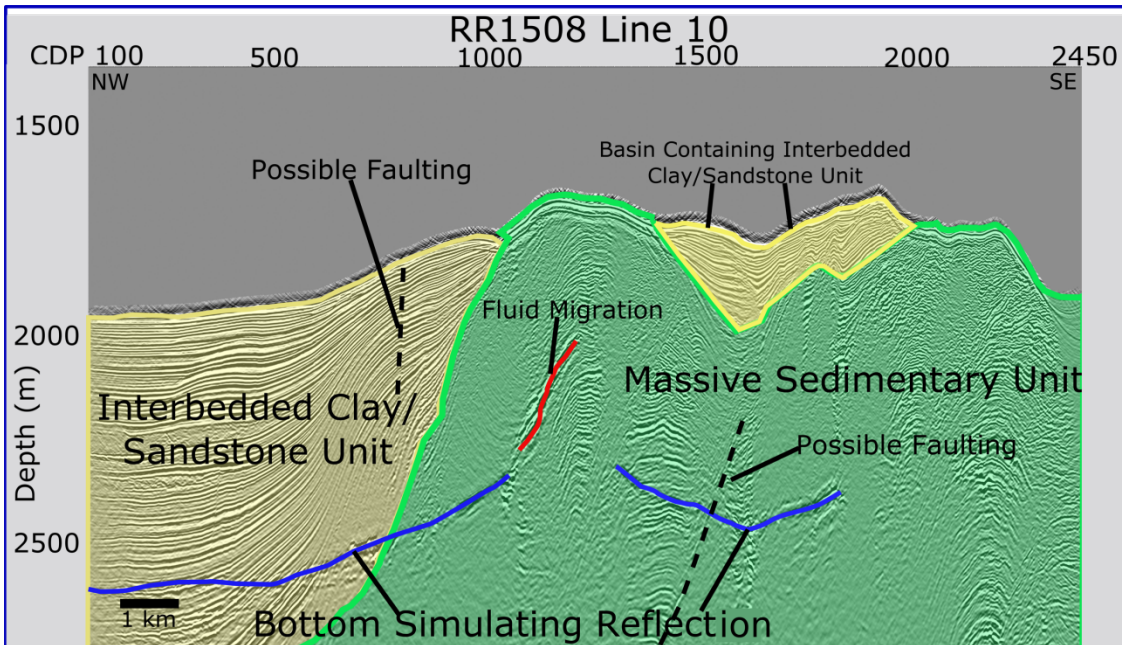

Figure 4.11 Line 10 from the RR1508 survey. The seismic line with interpreted features annotated. The interbedded clay/siltstone unit is highlighted in yellow and the massive silt/mudstone unit is highlighted in green.

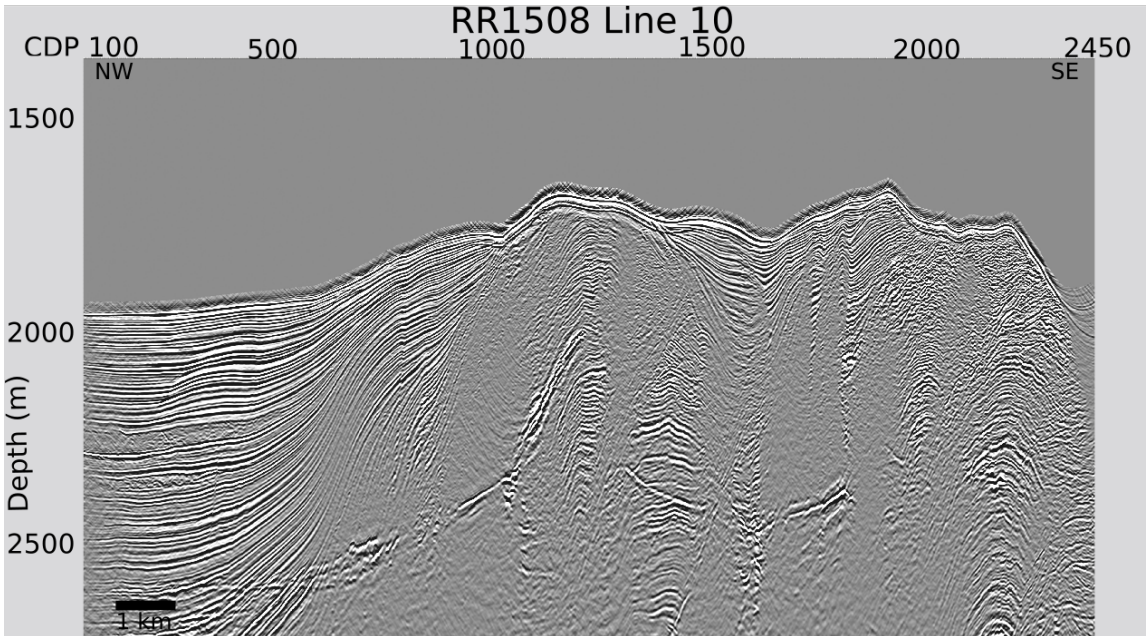

Figure 4.12 Line 10 from RR1508 un-annotated.

4.4 Summary

The interpretations based around the high-resolution RR1508 seismic data successfully improved the understanding of the fluid dynamics, lithologies and hydrate distribution beneath Pukeroro Ridge. The high-resolution reflections in combination with the velocity profiles clearly highlight the differences between two distinct lithological units and allow for a better understanding of the physical characteristics of the bedding. The amplitude data were instrumental in identifying a transformation from positive to negative impedance along a presumably porous unit, which in turn allowed for fluid migration interpretations. The reflections also provided a means to recognise the contact between hydrate-bearing sediment and gas-bearing sediment beneath the gas hydrate stability zone. In the following chapters, heat flow data will be incorporated to build on these interpretations, using both the variation in thermal characteristics of the units and the surface heat flow variations.

5 Heat Flow Along Seismic Line 10

5.1 Introduction

The main aim of the heat flow study conducted as part of this research across Pukeroro Ridge was to gain a better understanding of the physical and thermal characteristics of the geological units in the region and the hydrothermal regime controlled by the geology. The combination of heat flow and seismic data can be used to constrain thermal conductivities by making use of the BSR as an isotherm. By combining thermal conductivities, heat flow and seismic data we can get an insight into the subsurface dynamics of the region. All calculations were made between CDP 744 and 2154 (Figure 5.1) corresponding to the extent of the heat probe measurements.

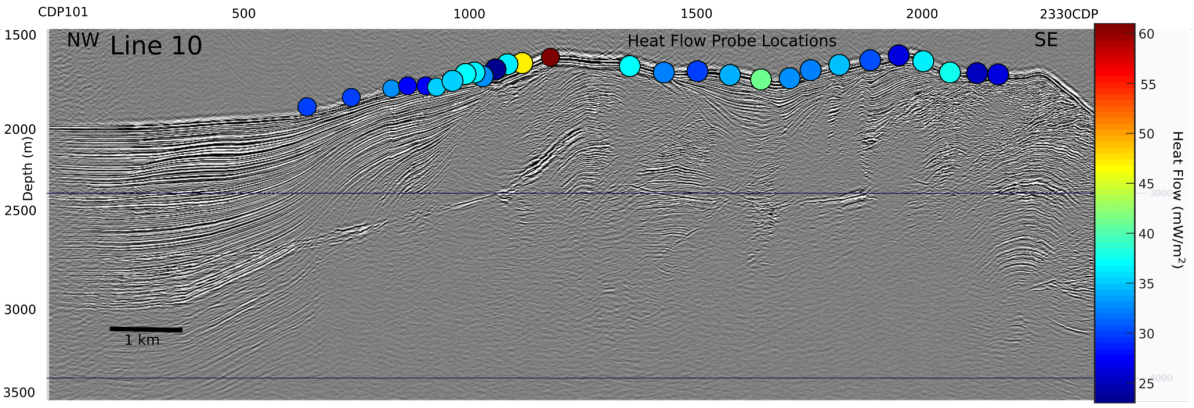

Figure 5.1. Seismic Line 10 with heat probe locations. Probe locations are colour coded according to heat flow measurements.

5.2 Picking the BSR

Selecting the depth of the BSR for the thermal gradients was not straight forward. Sections of the BSR were very obvious in the seismic data and could be picked with a high level of confidence. Other areas had an indistinct BSR and required some interpolation or interpretation. For the majority of the zones lacking a significant BSR, the seafloor-mimicking nature of the BSR meant interpolations between points were reasonably simple. The most difficult interpretation was picking an appropriate position for the BSR beneath an interpreted fluid flow feature. Fluid migration in this region results in no gas accumulating and as a result no BSR is formed. Therefore, interpolating the bottom of the gas hydrate stability zone becomes difficult. The first option is to assume that the fluid feature is localised and therefore the BSR would continue along the trend except for at the exact location of the fluid flow. This scenario was discounted due to the lack of gas accumulation,

suggesting that there is at least some fluid migration in the zone surrounding the fluid feature. The second option was to pick BSR slightly above the regional trend, but still connecting the visible BSR on either side (Figure 5.2).

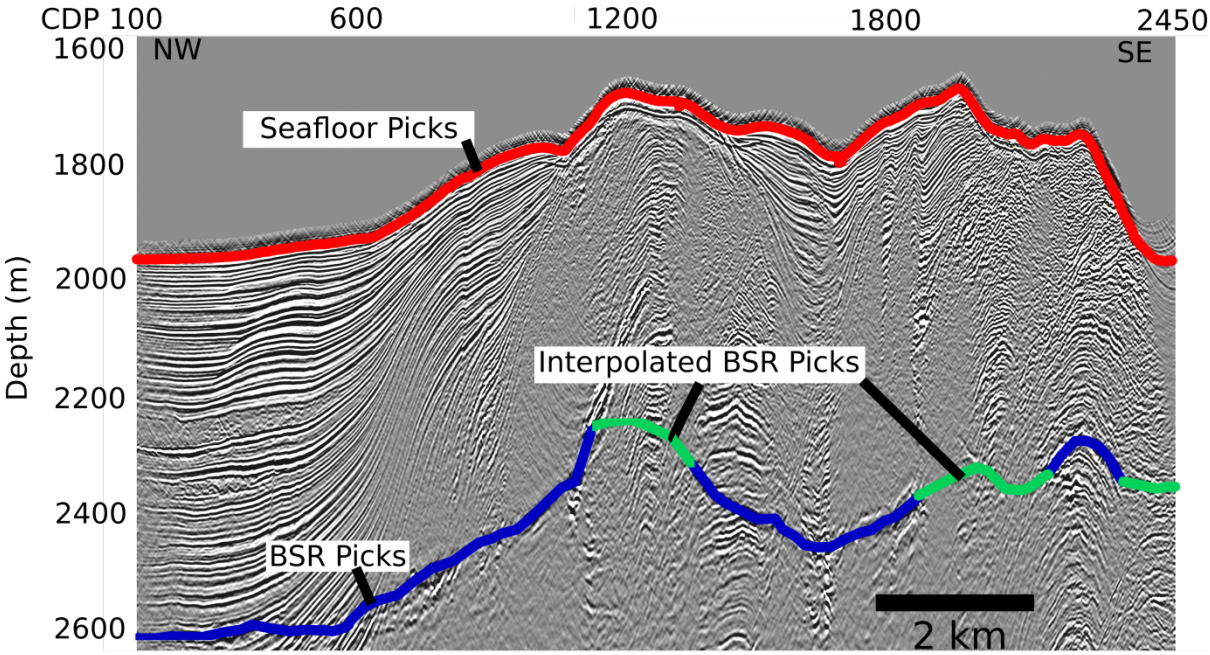

Figure 5.2 Seismic Line 10 with the seafloor, BSR and interpolated BSR picks annotated.

5.3 Results

5.3.1 Heat Probe Data

The measured heat flow data are erratic, with variable results ranging between 25 and 57 mW/m^2 (Figure 5.3). The data set identified one major heat flow anomaly where multiple heat flow measurements show an increasing trend to a high of 57 mW/m^2 at CDP 1200. Another significant peak was found at CDP 1600, with a heat flow reading of 40 mW/m^2. The peak at CDP 1600, however, is only one measurement. Three lows down to ~25 mW/m^2 at CDP's 900, 1900 and 2100 were also recorded by the heat flow probe. The south eastern-most kilometre exhibits a gently decreasing trend. Note that the data collection spacing was variable, with several gaps in the data due to failed probe measurements (Figure 5.1); this will have contributed to the roughness of the curve

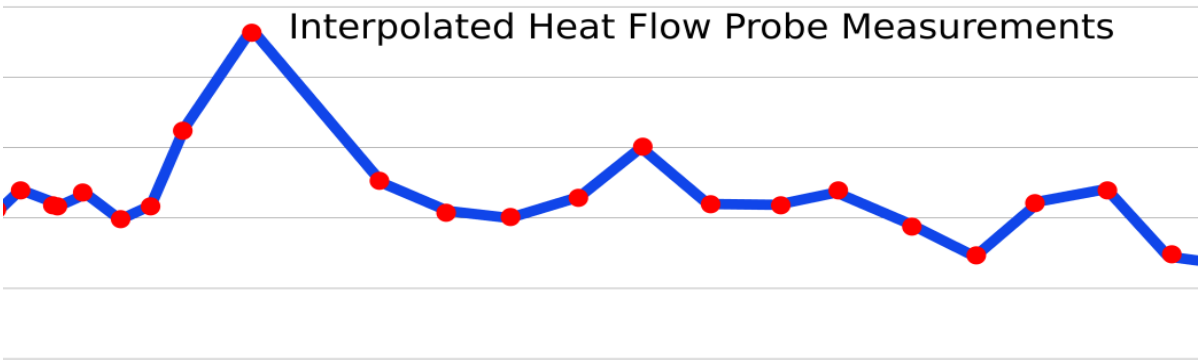

Figure 5.3 Interpolated heat flow measurements along seismic profile Line 10. The CDP spacing is 6.25 m.

5.3.2 **BSR Depths and Associated Temperatures**

The measured BSR depths are quite variable across seismic profile Line 10 (Figure 5.4). The first 400 CDPs at the north western end of the profile show a steep shallowing of the BSR from 2500 to 2250 metres below sea level (mbsl). The depth of the BSR then remains fairly constant for the next 160 CDPs before the sudden increase is reversed and the BSR deepens down to 2450 mbsl at CDP 1600. Following this decrease, the BSR then shallows again at a lower gradient rising to 2325 mbsl over the next 400 CDPs. The final 150 CDPs of the southeastern edge of the profile are characterised by a slight deepening of the BSR to 2355 mbsl, which is quickly reversed just before the line terminates.

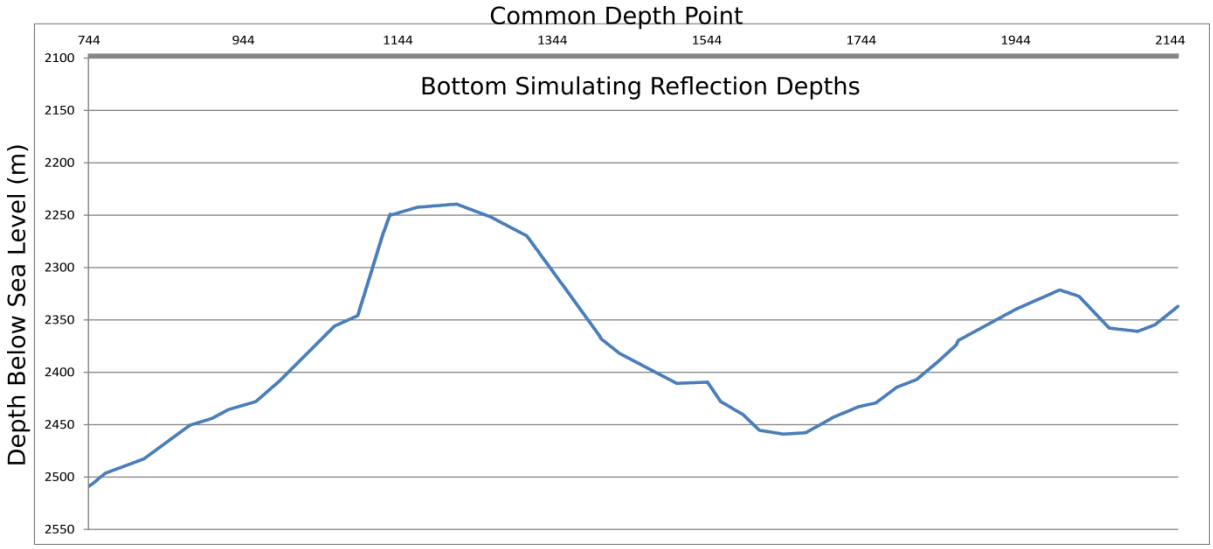

Figure 5.4. BSR depths at each CDP on Line 10, identified through depth conversion of seismic data. The CDP spacing is 6.25 m.

The gas hydrate stability curve script generated temperatures at the BSR based on the predicted gas hydrate stability conditions (Figure 5.5; Appendix 9.1). Temperatures start at 292.1 K on the north western edge of the profile and immediately decrease for the next 400 CDPs dropping to 291.1 K. The temperatures then rise again up to 292 K over the following 450 CDPs. Over the final 744 CDPs, there is initially cooling for the first 400 CDPs dropping to 291.48 K. There is then a small increase up to 291.7 K followed by a decrease down to 291.6 K.

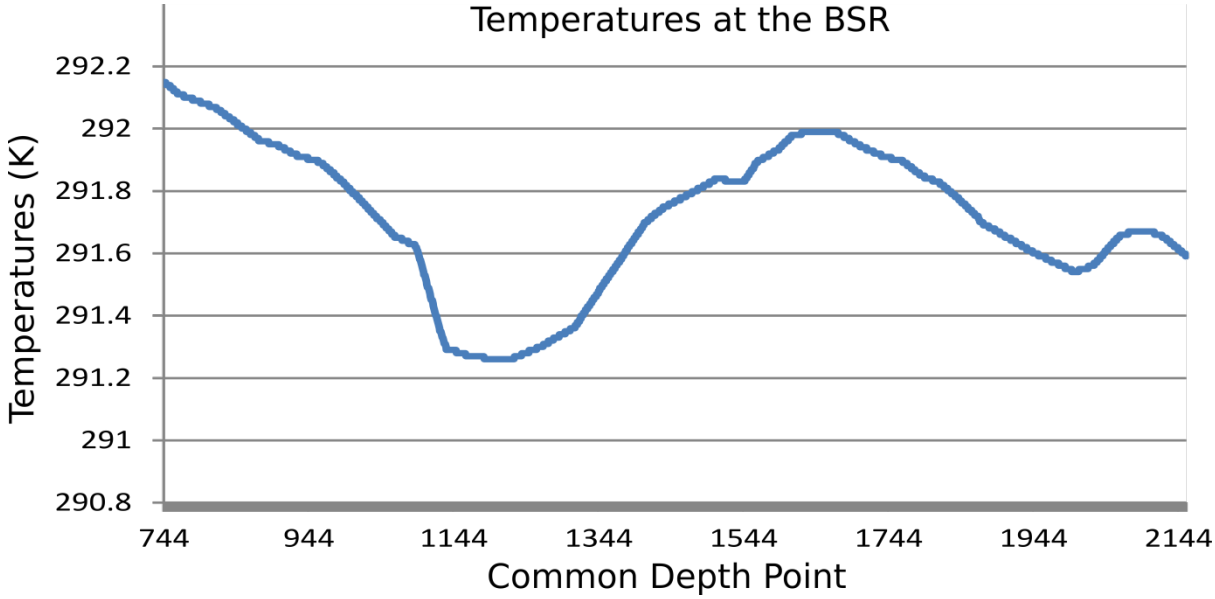

Figure 5.5. Temperature at the BSR based on the gas hydrate stability curve script. The CDP spacing is 6.25 m.

5.3.3 **Trends of the Thermal Gradients**

The geothermal gradients calculated from the BSR depths below the seafloor and the temperature at the BSR show some large-scale trends (Figure 5.6). The geothermal gradient was calculated at each CDP (Fig. 5.6) using the BSR depths below the seafloor, the temperature calculated at the BSR, and the interpolated water bottom temperature along the line. Some large-scale trends can be observed in these seismically derived values that match the trends measured by the heat probe (compare Figs. 5.3 and 5.6).

The first 225 CDPs of the profile show a gentle decrease in the geothermal gradient from 26 to 25 K/km. After a further 200 CDPs there is a spike in geothermal gradients which peaks at 29.5 K/km, 425 CDPs in from the north-western edge of the line. The 65 CDPs preceding the peak show a steep 3K/km drop in the geothermal gradient. After this decrease, there is a

gradual drop over the following 400 CDPs down to the lowest calculated geothermal gradient, 23 K/km. The following 65 CDPs show a slight increase of 2 K/km up to 25 K/km which quickly drops back down to 23 K/km where it stays at for a further 150 CDPs. The final 175 CDPs of the eastern edge of the profile exhibits a steep increase up to 27 K/km where the profile ends.

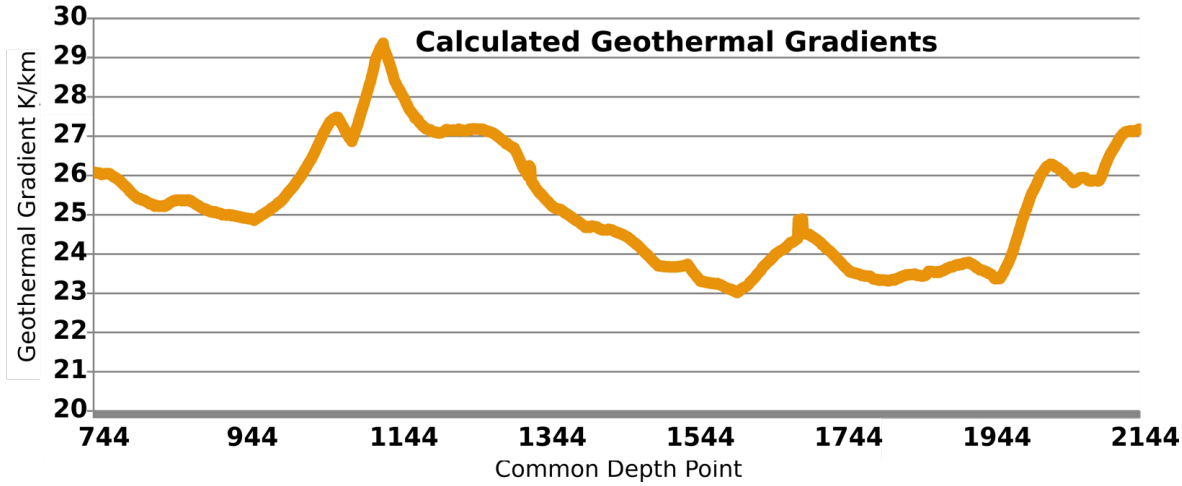

Figure 5.6. The thermal gradients per CDP calculated from the BSR depth below seafloor and the temperature at the BSR. The CDP spacing is 6.25 m.

5.3.4 **Thermal Conductivities**

The thermal conductivities calculated using the measured heat flow and the calculated geothermal gradient vary across the line (Figure 5.7) with the shape of the curve being dominated by the measured heat flow values. The first 150 CDPs show a slowly increasing trend from 1.15 to 1.30 W/m/K. Over the following 40 CDPs, the thermal conductivities drop down to 1.0 W/m/K, the next 65 CDPs reverse the previous decrease in thermal conductivity and thermal conductivity increases to 1.3 W/m/K. This increase is then reversed again over the following 65 CDPs, dropping down to 1.1 W/m/K. Following this low, a further 150 CDPs along the line, there is an extreme high where the thermal conductivity rises to its highest value of 2.1 W/m/K. This steep rise in thermal conductivity is then reversed for the following 150 CDPs, showing a steep decrease to 1.34 W/m/K. This decrease gently continues over a further 130 CDPs finally reaching a low of 1.2 W/m/K. The thermal conductivities then rise to 1.7 W/m/K over the next 150 CDPs. The following 380 CDPs generally decrease to 1.0 W/m/K with a slight rise up to 1.4 W/m/K, 180 CDPs into the decrease. The remaining 160 CDPs decrease down to the lowest thermal conductivity calculated at 0.85 W/m/K.

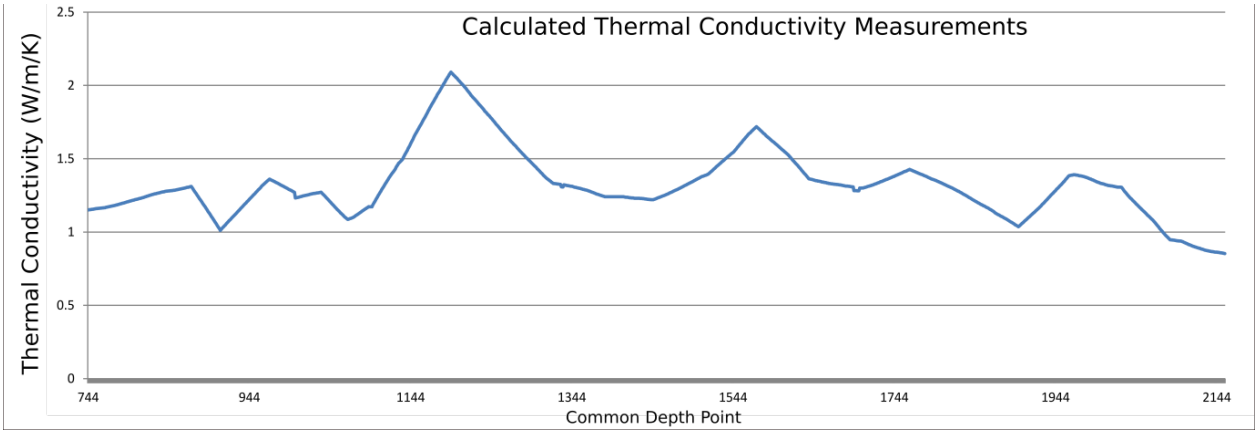

Figure 5.7. Thermal conductivity calculated for each CDP. The CDP spacing is 6.25 m.

5.4 Discussion

5.4.1 Focused Fluid Flow

The simplest interpretation that can be made is that the extreme peak in heat flow values of about 56 mW/m^2 coincides with the sudden decrease in the depth of the BSR and the transition from a typical BSR to what has been interpreted as a gas hydrate lens. This correlation suggest the possibility that fluid flow along a fault is allowing heat transfer via fluid movement, resulting in the heat flow anomaly (Figure 5.8) (Ligtenberg, 2005).

The thermal conductivities very closely follow the shape produced by the interpreted heat flow, showing the control that thermal conductivity has on heat flow (Figure 5.9). The thermal conductivity measurement can indicate whether the heat transfer is resulting purely from conduction or because of the migration of fluid which gives a false thermal conductivity high. Two separate peaks in thermal conductivity suggest two instances of fluid migration. The first anomaly, with a peak of 2.1 W/m/K, is the largest and is based on multiple heat flow measurements that suggest this is not the result of heat flow measurement errors. The second peak is much smaller at only 1.7 W/m/K, and it is associated with only one singular heat flow measurement. This suggests the possibility of an incorrect heat flow measurement (Bonneville, 2017).

The main thermal conductivity high also coincides with the interpreted hydrate lens localised around a possible fault. As previously mentioned, this further supports fluid migration as a means for increasing heat flow.

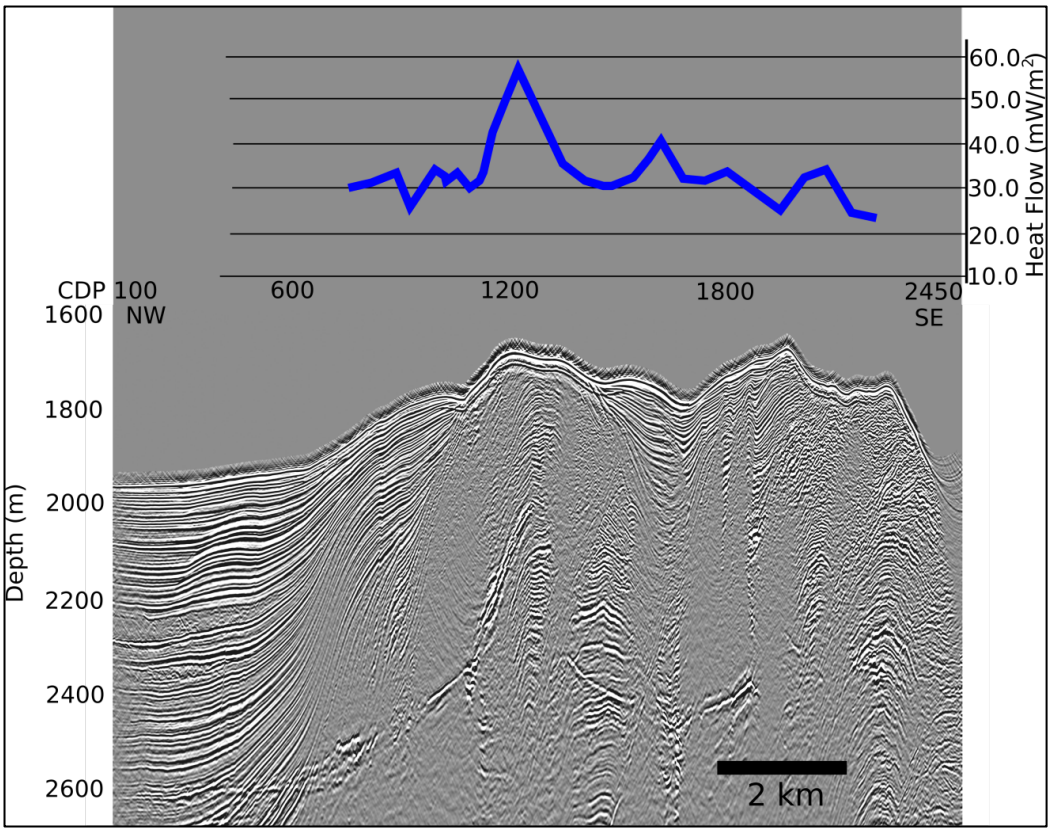

Figure 5.8 Image of seismic Line 10 with the measured heat flow overlain.

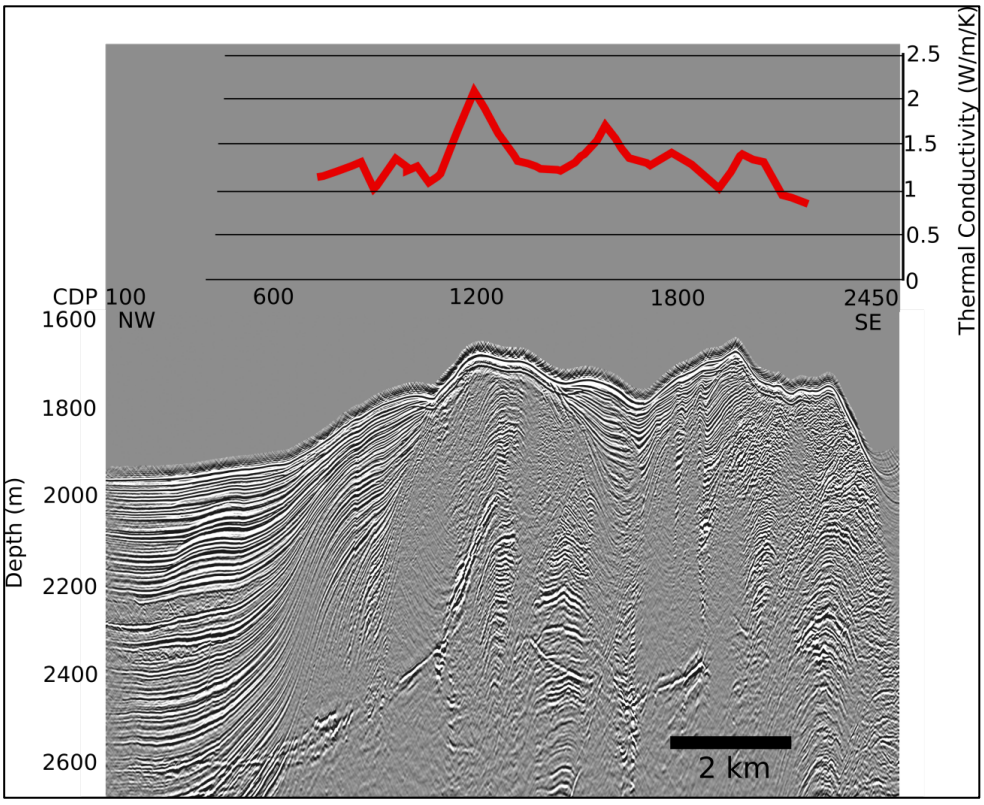

Figure 5.9 Seismic image of Line 10 with the calculated thermal conudctivities for each CDP annotated in (red).

5.4.2 **Overall Increase in Thermal Conductivities with Depth**

An increase in thermal conductivities with depth, calculated for each of the heat probe measurements collected during the tests, is expected. As the medium for which the thermal conductivity is determined deepens, the thermal conductivity increases due to increased pressure, a decrease in pore space and a more lithified medium, all of which contribute to the averaged properties of the medium for which thermal conductivity is measured (Abdulagatov et al., 2006).

Thermal conductivities increase by about 0.014 W/m/K per 1.0 MPa (Lin, 2011). However, pressures throughout the subsurface on the Hikurangi Margin are difficult to quantify due to the unknown effect of overpressure in the region. The pressures will range between a lithostatic pressure of 32.2 MPa and a hydrostatic pressure of ~18 MPa based on the average BSR depth of 618 m below the seafloor. By using a lithostatic pressure increase of 14.214 MPa, a maximum thermal conductivity increase, due to depth associated pressure increases can be suggested. With a lithostatic pressure at the mean BSR depth of 618 m below the seafloor, the maximum thermal conductivity increase is calculated to be 0.199 W/m/K between the seafloor and the BSR (Soufi, 2009). This increase is much lower than the increases observed for the majority of calculated thermal conductivity values (Figure 5.10). Note also that the increase is based on lithostatic pressure, which is much greater than the actual expected pressure. The expected pressure is predicted to be much closer to hydrostatic, which has an expected increase of only 6.31 MPa and 0.088 W/m/K at 618 m below the seafloor (Figure 5.10) (Milkov et al., 2004).

The large increases suggest a strong influence of fluid migration in the subsurface on the calculated thermal conductivity measurements. While the seismic data support this theory at CDP 1200 with a major heat flow anomaly, there are no seismic data that suggest localised fluid migration in other regions. This uniformly raised thermal conductivity across the seismic line suggests regional fluid advection. The effect of fluid flow is not evident in the surface measurements due to differences in the compaction and pore spaces of the sediment, compared to the lithified sediments used for producing calculated values between the BSR and seafloor. The near-surface sediments that the heat flow probe penetrates have a much greater pore volume. As a result, the upwelling fluid can dissipate quickly in the unconsolidated sediments resulting in an even distribution of warm fluid. This means the

fluid flow is more uniform through the unconsolidated sediments and as a result it does not affect the measured thermal conductivities.

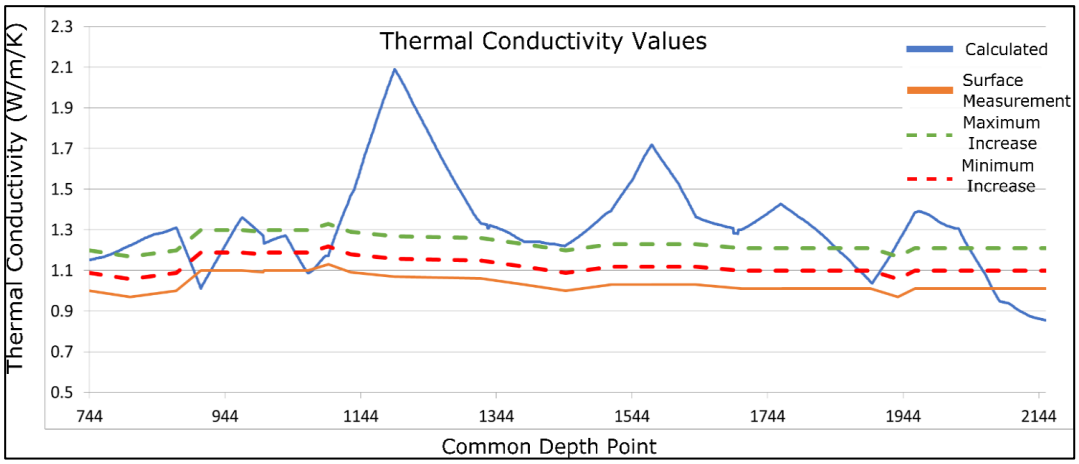

Figure 5.10. A graph comparing the thermal conductivities measured by the heat flow probe (orange) with the thermal conductivities calculated previously (blue). The dashed green line indicates the maximum increase of the measured thermal conductivities due to pressure increases based on lithostatic pressure. The dashed red line shows the minimum expected increase in thermal conductivity based off hydrostatic pressure.

5.4.1 **Bedded Sedimentary Package**

The sedimentary packages of alternating silt/mudstone and clay appear to have a fairly uniform heat flow of 30-33 mW/m^2 except for the two anomalies: one low at 25.5 mW/m^2, 5.2 km in from the north-western edge of the line and one high of 39.5 mW/m^2, 9.6 km in from the north-western edge of the line. The areas of bedding also coincide with the lowest thermal conductivity increases. The lack of major increases suggests that any fluid flow is minor. This is most likely due to the horizontal nature of the bedding and the reasonable assumption that fluid migration is channelled laterally through porous beds. As a result, vertical heat flow is mainly a result of conduction (Chapman, 1983).

5.5 Summary

The different thermal characteristics calculated from the heat flow probes using the BSR isotherm all exhibited their own local and regional trends. These patterns allow for investigation into the variations in thermal characteristics at and below the seafloor. The results support the identification of a significant fluid flow feature beneath the ridges and explain the heat flow anomaly recorded by the heat probe. The calculated thermal conductivities also suggest the possibility of regional fluid advection supported by higher

than expected thermal conductivities. In the following chapter the calculated thermal conductivities are combined with observations from the four other seismic lines in the area in an attempt to map the heat flow of the entire Pukeroro Ridge locality.

6 Heat Flow Extrapolation over Regional Seismic Lines

6.1 Introduction

The previously calculated thermal conductivities in combination with the high-resolution seismic data provided a good opportunity for estimating heat flow along adjacent lines, where no heat probe measurements have been collected. This method allows for wide-spread regional-scale heat flow interpretations, in an area containing seismic data, if accurate thermal conductivities can be determined. The issue that presents itself when applying this method to the Pukeroro Ridge locality is the lack of available drill cores used to determine thermal conductivities. To try and overcome this, thermal conductivities have been calculated from heat probe measurements. Due to the regional continuity of the lithological units, these thermal conductivities can be interpreted and used to assess heat flow across the extent of the survey area. This method is much more efficient and cost effective than collecting physical measurements with a heat flow probe.

6.2 Method

6.2.1 Calculating the Geothermal Gradients

The geothermal gradients for lines 9, 11, 12 and 13A were calculated using the gas hydrate stability script mentioned in Chapter 2.7 and Appendix 9.2. These lines are parallel to Line 10, which was collected along the heat probe transect. The same water column temperature profile was used for all lines as data in the region were limited at the required depths.

The geothermal gradients that were calculated from lines 9, 11, 12 and 13A followed very similar trends to those seen in Line 10 (Figure 5.6). The lines furthest from Line 10 (12 and 13A) were slightly less variable, although anomalies were located over the same features identified on other lines. These results highlight the uniformity of the BSR along the ridge.

6.2.2 Developing Thermal Conductivity Profiles

A major consideration with calculating accurate heat flow measurements based on seismic data is the issue of how to map the thermal conductivity of the region. In most previous studies using similar techniques, cores have been used to obtain laboratory based thermal conductivity measurements, which can then be used to produce an accurate thermal conductivity profile. For this survey, there has been no nearby coring of sedimentary units and as a result there are no thermal conductivities other than those measured at the surface

during the heat flow probe measurements. While the surface thermal conductivities are more accurate than assuming a constant thermal conductivity, these surface measurements have significant errors associated with them due to the measurements not being taken from a depth that correlates to the geothermal gradients. Another option was to link or match corresponding seafloor structures such as peaks and valleys from Line 10 with each of the other seismic profiles, then rescale and overlay the thermal conductivities on to the new lines. This method creates more accurate thermal conductivity profiles for the majority of the lines due to their parallel nature, meaning that variability between lines is limited. However, line specific features, in either Line 10 or the other lines, would most likely result in the application of inaccurate thermal conductivities.

The best option was to explore both thermal conductivity estimation methods and create two heat flow profiles: one using the interpolated surface measurements, and one using the thermal conductivities calculated based on Line 10.

Table 6.12 Matching CDPs as interpreted for each line, with each row corresponding to one significant feature. This allowed the geothermal gradients of Line 10 to be applied and scaled to the new lines.

Line 9	Line 10	Line 11	Line 12	Line 13A
533	747	1669	1599	2242
812	1066	1318	1344	1862
973	1197	1144	1222	1679
1138	1346	1083	1177	1612
1202	1430	1036	1092	1575
1377	1544	958	1018	1534
1476	1680	826	867	1423
1727	1964	453	455	971
1864	2092	389	241	880

The correlation method used the MATLAB ‘interp1’ function as described in the script (Appendix 9.2). To allow this to work, nine features were matched across all five lines. (Table 6.12). The CDPs at each of the features where then matched and due to differing CDP numbers separating the features, the targeted line was given new CDP numbers which

matched the CDPs from Line 10. The thermal conductivities were then matched to these new CDPs. This new set of CDPs with the thermal conductivities could then be rerun through the 'interp1' function and the thermal conductivities matching the original CDPs were found. This method was used for both the calculated thermal conductivities and the heat probe measured thermal conductivities.

6.2.3 **Calculation of Heat Flow**

geothermal gradients and produce a heat flow value. Just as for Line 10, the heat flow values were calculated for each CDP assuming only vertical heat transfer. 176°30'

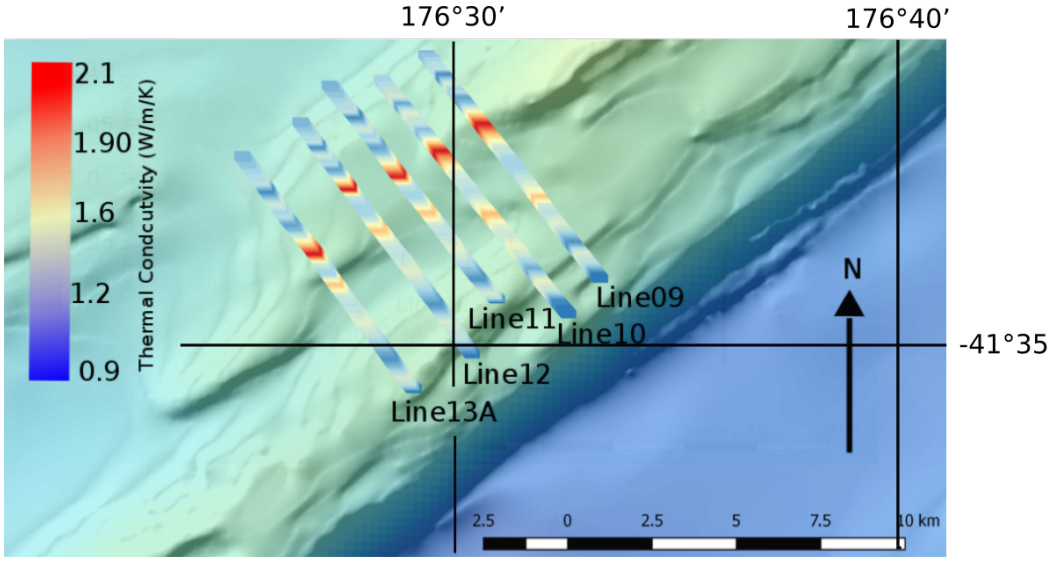

Figure 6.1. The thermal conductivity profile for each line calculated using the thermal conductivities calculated from the heat flow values of line 10.

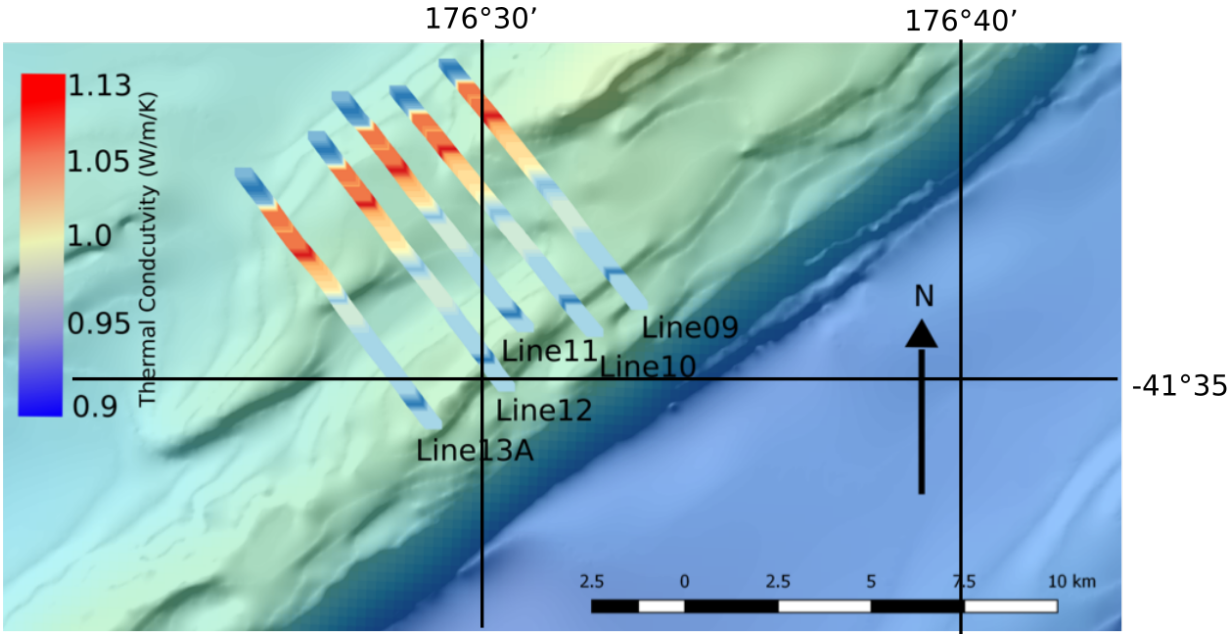

Figure 6.2. The thermal conductivity profile for each line calculated based of the thermal conductivities measured by the heat flow probe

6.3 Results

6.3.1 **Lines 9, 11, 12, 13A**

The results calculated from the geothermal gradient profiles show two distinct trends between the different thermal conductivities (Figures 6.3 to 6.6) . The heat flow trends calculated using the heat flow probe measurements (Figure 6.2) all strongly follow the same trend as the geothermal gradients. There are several sections, such as between CDPs 667 and 1203 in Line 9 (Figure 6.3), where the heat flow deviates from the gradients but the deviations are uniform and the trends remain the same. The heat flow values produced using the thermal conductivities calculated from Line 10 (Figure 6.1) show a completely different trend. While the trends are not exactly the same as the thermal conductivity profile used, significant peaks in the heat flow appear in the thermal conductivity profiles also, such as the peak in heat flow at 1150 CDP in Line 11 (Figure 6.4). As a result, the heat flow profiles for all lines are erratic and highly variable with very few sections of stable heat flow readings.

There is a peak, at CDP 1806 in Line 9 (Figure 6.3), which is the second highest along the line. The corresponding thermal conductivity high is only the fourth highest peak along the line. This indicates an increased thermal gradient is resulting in the high heat flow.

The trends at the western ends of the profiles are almost identical in all of the lines. This is evident in both the calculated heat flow and the geothermal gradients

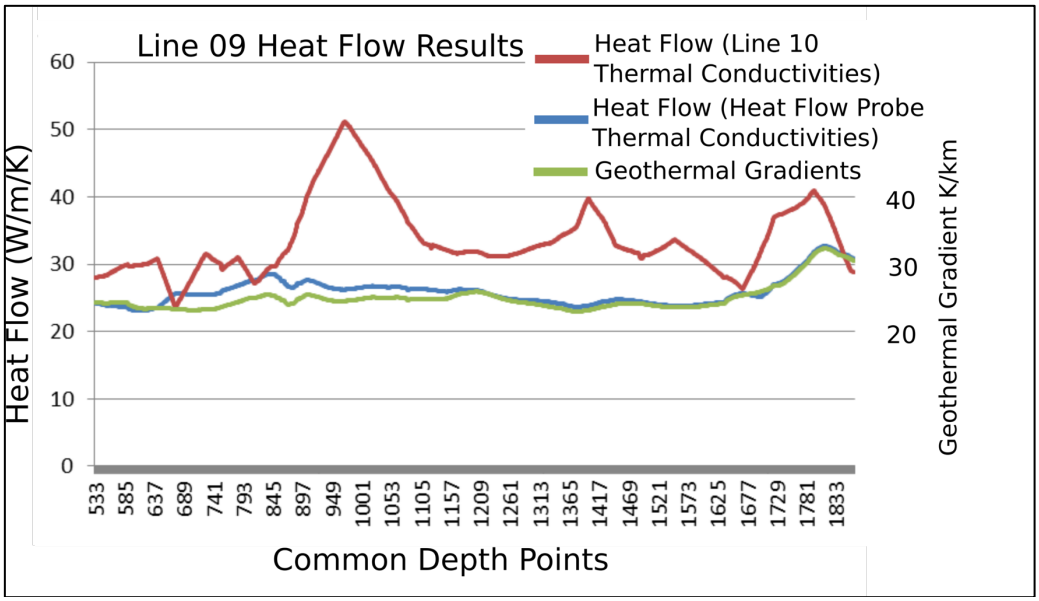

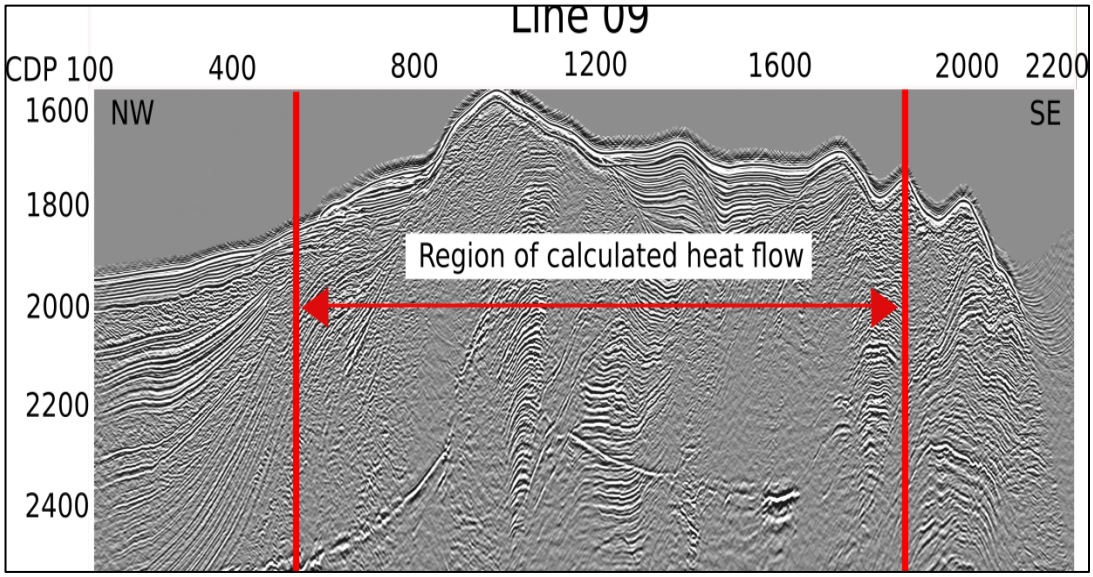

Figure 6.3 Heat flow results from Line 9. In red are the heat flow results calculated using the thermal conductivities determined from Line 10. In blue are the heat flow results calculated using the thermal conductivities measured by the heat flow probe. In green are the geothermal gradients.

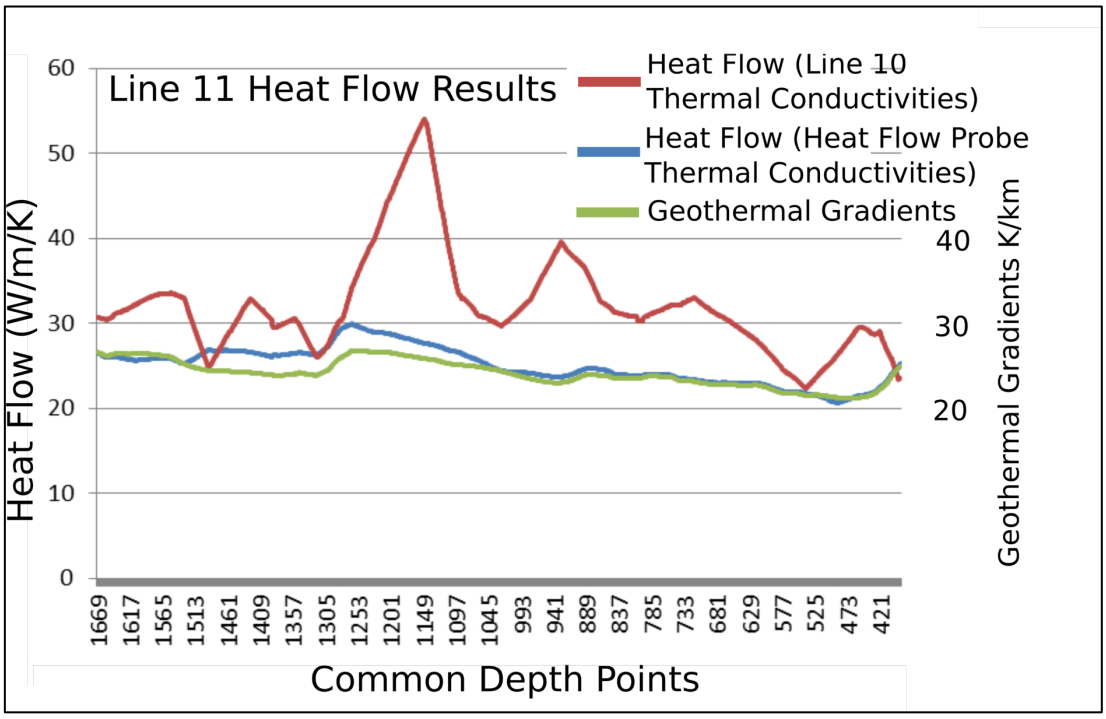

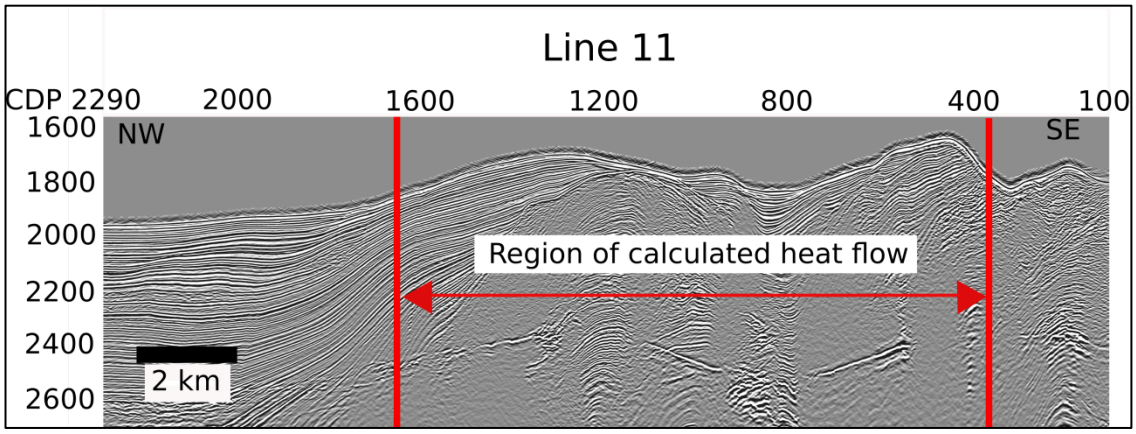

Figure 6.4 Heat flow results from Line 11. In red are the heat flow results calculated using the thermal conductivities determined from Line 10. In blue are the heat flow results calculated using the thermal conductivities measured by the heat flow probe. In green are the geothermal gradients.

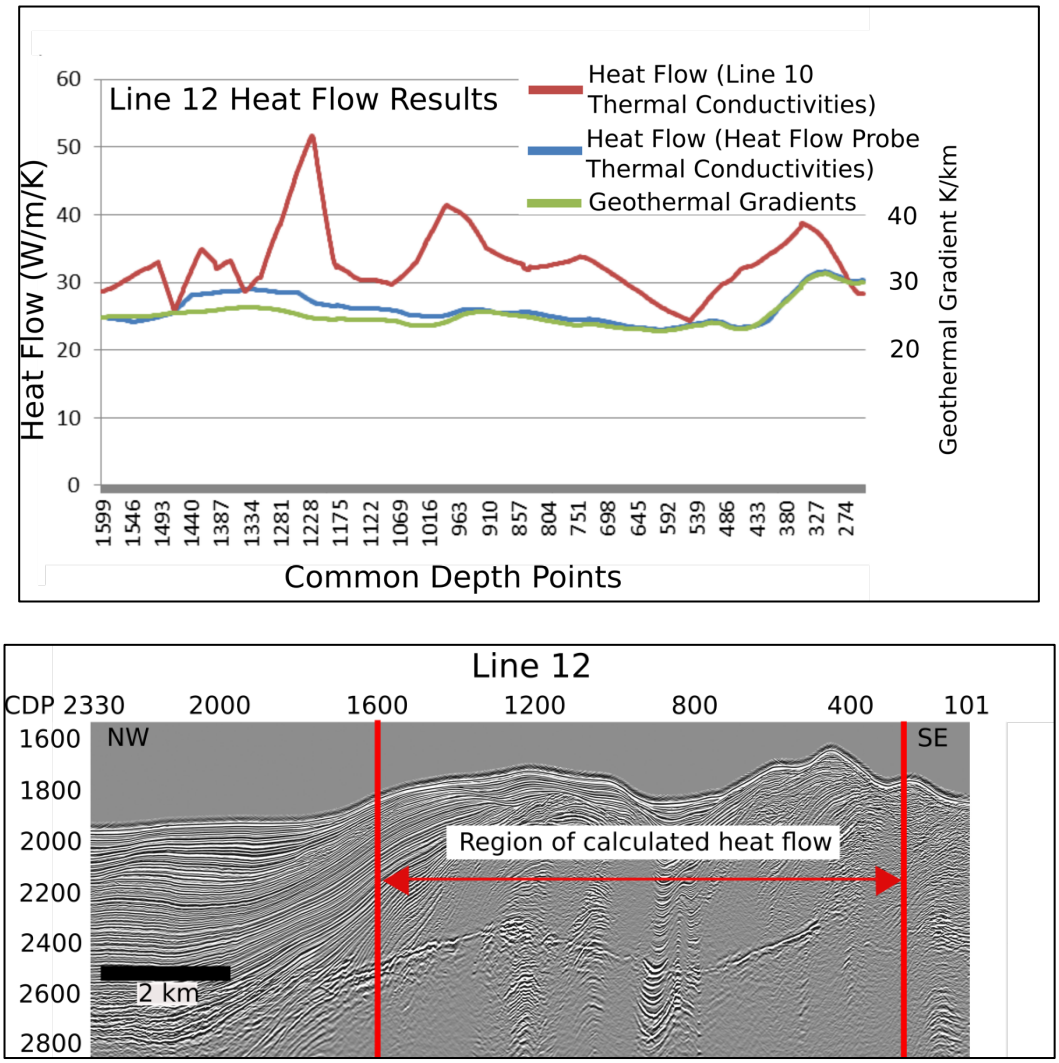

Figure 6.5 Heat flow results from Line 12. In red are the heat flow results calculated using the thermal conductivities determined from Line 10. In blue are the heat flow results calculated using the thermal conductivities measured by the heat flow probe. In green are the geothermal gradients.

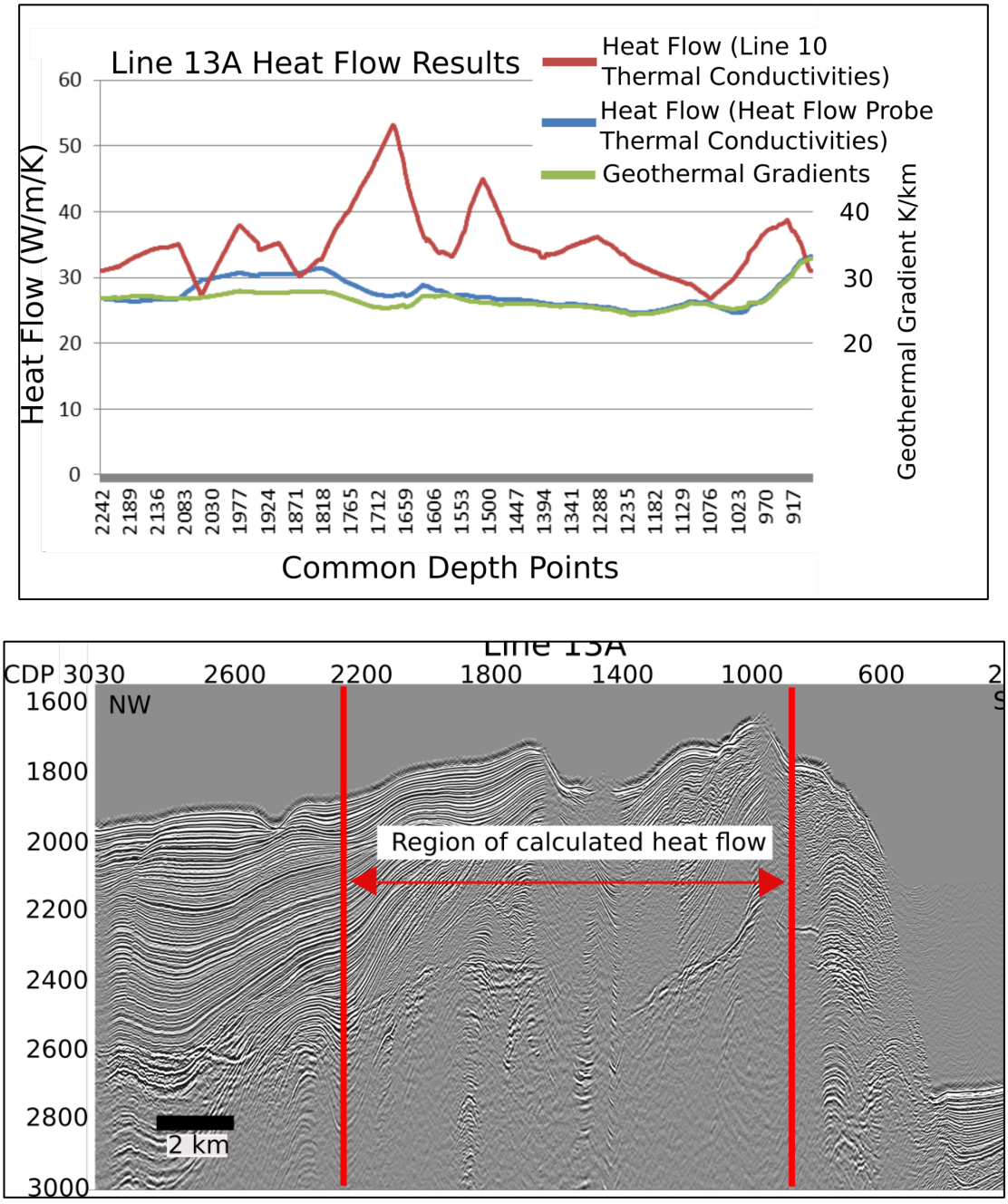

Figure 6.6 Heat flow results from Line 13A. In red are the heat flow results calculated using the thermal conductivities determined from Line 10. In blue are the heat flow results calculated using the thermal conductivities measured by the heat flow probe. In green are the geothermal gradients.

6.4 Discussion

The heat flow results produced using the calculated thermal conductivities appear to be strongly controlled by the conductivities and only large changes in the thermal gradients are visible in the resulting heat flow profiles. The reverse is found when using the surface thermal conductivities extracted from the heat flow probe measurements. This trend is expected as the majority of the thermal conductivities are 1.0 and as a result heat flow will equal the thermal conductivity. In some sections mentioned above, the heat flow is no longer 1:1 with the thermal conductivities due to slight increases in the thermal conductivities.

6.4.1 Calculations Using the Heat Flow Probe Thermal Conductivities

The uncertainties associated with using the thermal conductivities from the heat flow probes are fairly constant throughout all the lines. The thermal conductivities are almost certainly too low and do not allow for an increase in thermal conductivity associated with an increase in pressure. This increase will be relatively uniform and while the trends are probably similar the absolute values of the heat flow readings are most likely low. The stable thermal conductivities also mean any localized thermal variations are not accounted for and as a result are not visible in the heat flow data.

Using a relationship which describes the effect of pressure on thermal conductivities and assuming hydrostatic pressure, we can assume that the average heat flow reading is about 0.088 W/m/K lower than originally calculated, although they could be up to 0.199 W/m/K lower if it is under lithospheric pressure.

6.4.2 Calculations Using Calculated Thermal Conductivities

The uncertainties associated with the calculated thermal conductivities are much more variable and harder to quantify. The errors are as a result of changes in the fluid regime between lines. In certain lines, like Line 12, the proposed fluid flow feature, seen in Line 10 is much less pronounced. If the absence of this feature in Line 12 does indicate a decrease in fluid flow, then the high thermal conductivity used from Line 10 which accounted for this feature, will be incorrect when paired with Line 12 (Figure 6.5) and as a result the corresponding heat flow values will be raised.

As well as variations in the fluid regime of the subsurface, changes in the lithologies between lines can also result in incorrect thermal conductivities being used, leading to possibly incorrect heat flow results. Certain areas, like the north-western edges of the lines, appear constant throughout all of the lines and as a result the heat flow readings produced are accurate. However, the large heat flow anomaly in Line 12 is most likely exaggerated, based on the lack of evidence of fluid flow in the region and a change in the upper lithologies, most likely making the actual thermal conductivities considerably lower (Figure 6.7).

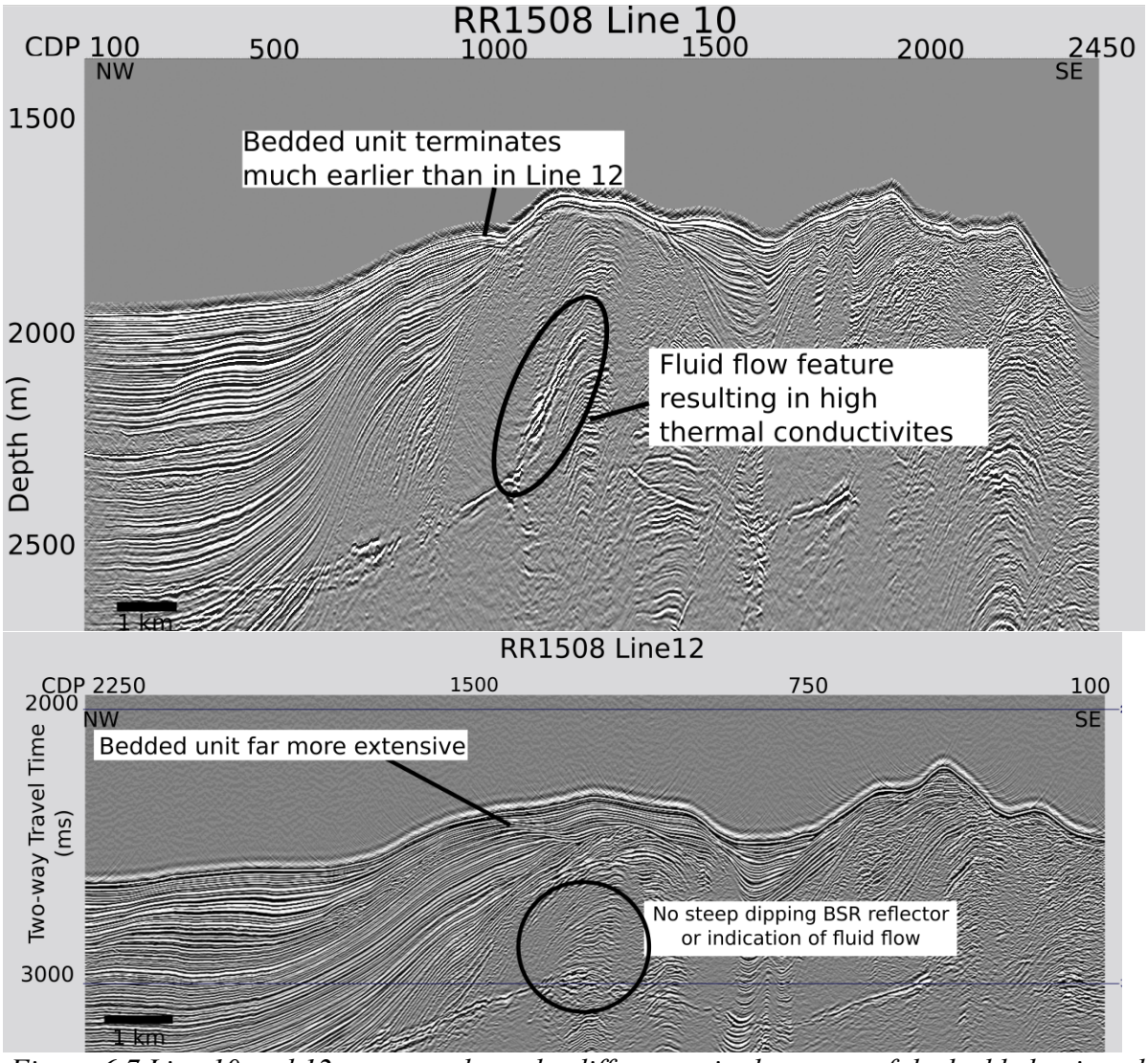

Figure 6.7 Line 10 and 12, annotated are the differences in the extent of the bedded unit and the loss of the fluid flow feature.

6.5 Heat Flow Maps

The estimated heat flow profiles can be combined with the interpolation module 'Nearest Neighbour' using the IHS Kingdom software to create heat flow maps of the region (Figure 6.8. Two maps were created from the calculations; one using the heat flow values that used the calculated thermal conductivities and one using the heat flow values that were determined using the measured thermal conductivities. Along Line 10 the measured heat flow values were used in both maps.

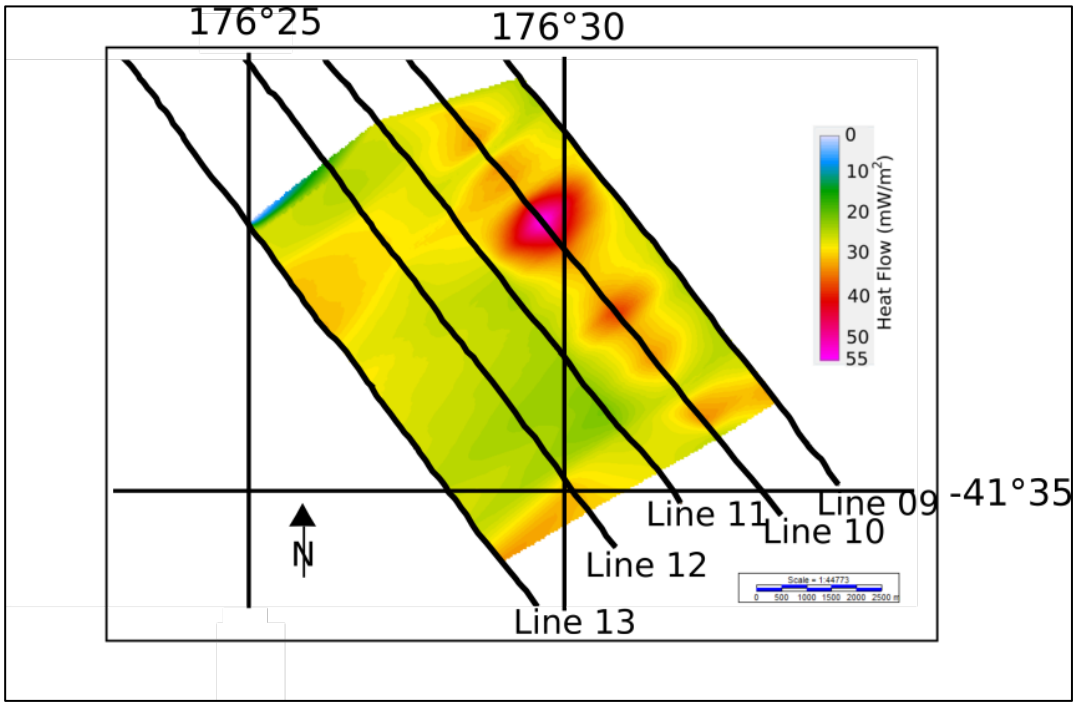

Figure 6.8. Heat flow map produced through interpolation between lines. The heat flow data were calculated using the measured thermal conductivities from the heat flow probe.

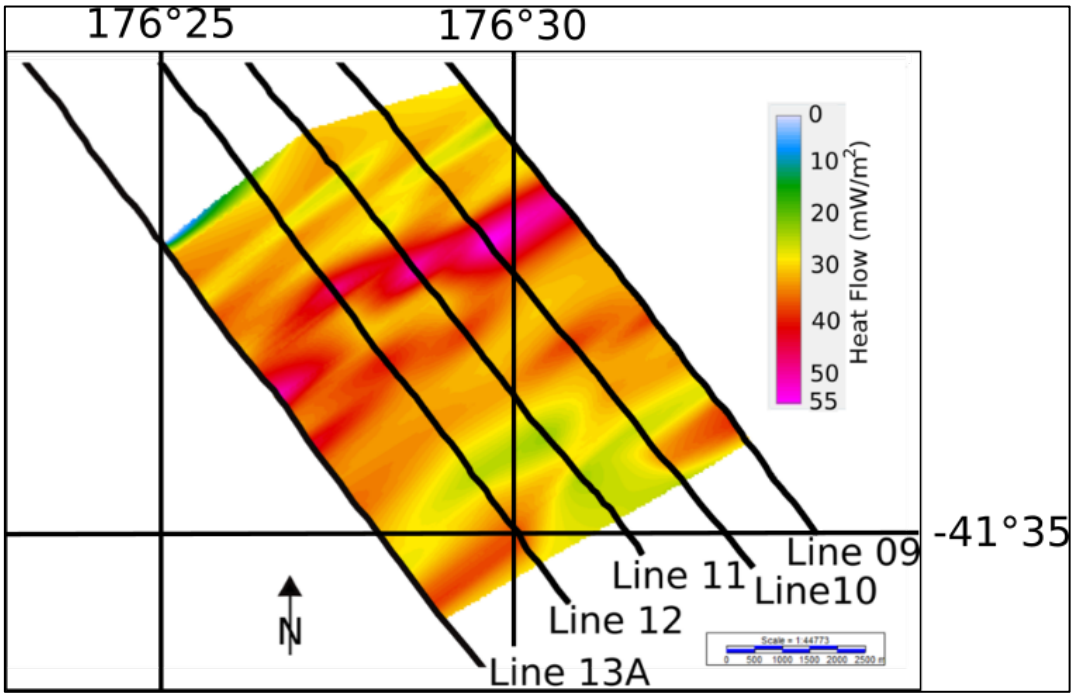

Figure 6.9. Heat flow map produced by interpolation between lines. The heat flow data were determined using the thermal conductivities calculated from the thermal conductivities derived from the heat flow measurements.

The heat flow maps are significantly different, highlighting the importance of the thermal conductivities in the calculations. Figure 6.8 clearly shows that the measured thermal conductivities are much lower than they should be and as a result the heat flow values are also low. The measured heat flow values from Line 10 are much higher than the surrounding lines. Despite this, a slight heat flow high can still be seen in the data following along the ridge line, in line with the recorded heat flow anomaly from Line 10.

In the map derived using the thermal conductivities that were calculated from the heat flow results, several high heat flow features are visible (Figure 6.9). The heat flow map contains several trends which appear to follow topographic features. This is expected as the topographic features were used to correlate the thermal conductivities between lines. This map appears to be strongly controlled by the thermal conductivities and heat flow anomalies that are identified in regions without temperature gradient anomalies.

Heat flow mapping using the measured thermal conductivities probably will be uniformly low across the area, although major heat flow features may still be visible. Heat flow mapping using thermal conductivities that are calculated from heat flow measurements will be accurate in areas with continuous and uniform lithologies. In areas with rapidly changing lithologies or fluid features, there will be an element of uncertainty associated with such a map.

6.6 Summary

While errors are present in the results, a fairly regular stratigraphic and structural setting could allow for efficient and accurate heat flow mapping to be done over a large area based on a single heat flow transect. However, localities with varying lithologies and strata or localised fluid features would only allow for very simple heat flow mapping and produce larger uncertainties in the geothermal interpretations.

7 Conclusions

7.1 Summary

The Hikurangi Margin is a dynamic, active plate margin, that has been widely studied through a variety of geophysical techniques. In this thesis, overlapping high-resolution and commercial seismic data sets were used alongside a single heat flow transect to learn more about the subsurface fluid and heat flow regimes. The dynamic nature of the region, in combination with the wide variety of data types, made this region ideal for developing and evaluating methods to jointly interpret these data sets to assess the fluid and thermal dynamics of the subsurface.

The seismic data sets used provide contrasting results between two distinctly different data types, each with their own specific uses and advantages. The high-resolution data set provided 2-3 m resolution and accurately imaged bedding and fluid flow structures. The detailed intermittent nature of the BSR was evident in the data set and provided much information about the subsurface.

The conventional data set had lower resolution of about 10 m but its penetration was much greater, reaching up to 7.0 s beneath the seafloor. The near surface was imaged in lower detail; however, the reflections were much more continuous and as a result they were easier to identify laterally across the seismic lines.

A comparison of the data sets highlights the significance of good velocity control. The high-resolution data lacked detail in certain localities where NMO and migration processing techniques were less effective. One of the reasons for this poor detail is resulting from the short-offset nature of the data.

Combining BSR depths determined from seismic data with the heat flow probe data was a successful technique which identified thermal conductivity anomalies beneath the surface. These anomalies were also supported by findings in the seismic data further verifying the accuracy of the process.

The attempt to extrapolate the single heat flow transect onto parallel seismic lines was partially successful. However, errors must be taken into account for this process, especially in

regions with varying lithologies and isolated fluid features. While the technique struggled to account for fluid flow, both from the thermal conductivities used and the presence of fluid flow in the line being evaluated, areas with regular stratigraphy and structural settings and uniform lithologies showed realistic heat flow results. These findings suggest that areas with continuous lithologies and without major fluid flow features would be perfect subjects for this technique; however errors quickly arise when the geology changes.

7.2 Future work

While the method and studies provided insight into the subsurface dynamics beneath Pukeroro Ridge, they also led to the development of several questions that will require future work and studies to fully understand. By collecting more physical data on the rock units and fluids of the margin, many of the geophysical calculations can be better assessed and the errors further quantified. By collecting drill cores, more accurate thermal conductivities can be measured which could provide more information around heat flow variations resulting from fluid migration, allowing for more accurate heat flow results. These cores will also improve the constraints on the lithologies and ages of the rock units, allowing for a better understanding of the geological history of the region. Future studies could provide a greater quantity of seismic data and more heat flow transects. These data would allow for improved identification of structural targets and a better idea of the thermal variations along and across structures in the wider region, which in turn could allow for large-scale detailed mapping of the region.

Bibliography

Abdulagatov, I.M., Emirov, S.N., Abdulagatova, Z.Z., Askerov, S.Y., 2006. Effect of Pressure and Temperature on the Thermal Conductivity of Rocks. J. Chem. Eng. Data 51, 22–33. doi:10.1021/je050016a

Adkins, C.J. (Clement J., 1987. An Introduction to Thermal Physics. Cambridge University Press.

Anderson, R., McMechan, G., 1989. Automatic Editing of Noisy Seismic Data. Geophys. Prospect. 37, 875–892.

Andreassen, K., Hart, P.E., Grantz, A., 1995. Seismic Studies of a Bottom Simulating Reflection Related to Gas Hydrate Beneath the Continental Margin of the Beaufort Sea. J. Geophys. Res. 100673, 659–12. doi:10.1029/95JB00961

Baker, D., 2016. Gas hydrate system dynamics in the Uruti Basin, an upper slope basin on New Zealand's Hikurangi Margin. The University of Otago.

Barnes, P.M., de Lépinay, B.M., Collot, J.-Y., Delteil, J., Audru, J.-C., 1998. Strain partitioning in the transition area between oblique subduction and continental collision, Hikurangi margin, New Zealand. Tectonics 17, 534. doi:10.1029/98TC00974

Barnes, P.M., Lamarche, G., Bialas, J., Henrys, S., Pecher, I., Netzeband, G.L., Greinert, J., Mountjoy, J.J., Pedley, K., Crutchley, G., Barnes, P.M., 2010. Tectonic and geological framework for gas hydrates and cold seeps on the Hikurangi subduction margin, New Zealand. Mar. Geol. 272, 26–48. doi:10.1016/j.margeo.2009.03.012

Barry, K.M., Cavers, D.A., Kneale, C. w., 1975. Recommended Standards for Digital Tape Formats. Geophysics 40, 344–352.

Batzle, M., Wang, Z., 1992. Seismic properties of pore fluids 57, 1396–1408.

Beardsmore, G.R. (Graeme R., Cull, J.P. (James P., 2001. Crustal heat flow : a guide to measurement and modelling. Cambridge University Press.

Blackstock, D.T., 2000. Fundamentals of physical acoustics. Wiley.

Blackwell, D.D., Steele, J.L., 1989. Thermal conductivity of sedimentary rocks: measurement and significance, in: Thermal History of Sedimentary Basins. pp. 13–37. doi:10.1007/978-1-4612-3492-0_2

Bland, K.J., Uruski, C.I., Isaac, M.J., 2017. New Zealand Journal of Geology and Geophysics Pegasus Basin, eastern New Zealand: A stratigraphic record of subsidence and subduction, ancient and modern Pegasus Basin, eastern New Zealand: A stratigraphic record of subsidence and subduction, ancient and modern. doi:10.1080/00288306.2015.1076862

Bonneville, A., 2017. Marine Heat Flow Probe [WWW Document]. Paris Inst. Earth Phys. URL http://www.ipgp.jussieu.fr/~bonneville/heat-flow3.html

Cao, Z., 2006. Analysis and application of the Radon transform. of Calgary.

Chapman, R.E., 1983. Chapter 3 Compaction of Sediment and Sedimentary Rocks, and its Consequences. pp. 41–65. doi:10.1016/S0376-7361(08)70087-6

Chi, W.C., Reed, D.L., Liu, C.S., Lundberg, N., 1998. Distribution of the bottom-simulating reflector in the offshore Taiwan collision zone. Terr. Atmos. Ocean. Sci. 9, 779–794.

Childs, J.R., Hart, P., Bruns, T.R., Marlow, M.S., Sliter, R., 2000. High-Resolution Marine Seismic Reflection Data from the San Francisco Bay Area.

Claerbout, J.F., 1986. Imaging the Earth's Interior. Geophys. J. Int. 86, 217–219. doi:10.1111/j.1365-246X.1986.tb01086.x

Cooper, A.K., Hart, P.E., 2003. High-resolution seismic-reflection investigation of the northern Gulf of Mexico gas-hydrate-stability zone. Mar. Pet. Geol. 19, 1275–1293.

Crutchley, G.J., Berndt, C., Geiger, S., Klaeschen, D., Papenberg, C., Klaucke, I., Hornbach, M.J., Bangs, N.L.B., Maier, C., 2013. Drivers of focused fluid flow and methane seepage at south Hydrate Ridge, offshore Oregon, USA. Geology 41, 551–554.

doi:10.1130/G34057.1
Crutchley, G.J., Fraser, D.R.A., Pecher, I.A., Gorman, A.R., Maslen, G., Henrys, S.A., 2015. Gas migration into gas hydrate-bearing sediments on the southern Hikurangi margin of New Zealand. J. Geophys. Res. Solid Earth 120, 725–743. doi:10.1002/2014JB011503
Crutchley, G.J., Maslen, G., Pecher, I.A., Mountjoy, J.J., n.d. High-resolution seismic velocity analysis as a tool for exploring gas hydrate systems: An example from New Zealand's southern Hikurangi margin. doi:10.1190/INT-2015-0042.1
Fader, G.B.J., 1997. The Effects of Shallow Gas on Seismic Reflection Profiles, in: Glaciated Continental Margins. Springer Netherlands, Dordrecht, pp. 29–30. doi:10.1007/978-94-011-5820-6_4
Fletcher, P.T., 2016. The Geological Evolution of Otago Harbour: A High-Resolution Seismic Reflection Study.
Fohrmann, M., Pecher, I.A., 2012. Analysing sand-dominated channel systems for potential gas-hydrate-reservoirs using an AVO seismic inversion technique on the Southern Hikurangi Margin, New Zealand. Mar. Pet. Geol. 38, 19–34. doi:10.1016/j.marpetgeo.2012.08.001
Fraser, D., 2017. Seismic Characterisation of Hydrate and Shallow Gas Systems Associated with Active Margin Sediments in the Pegasus Sub-basin, Hikurangi Margin, New Zealand.
Gadallah, M.R., Fisher, R.L., 2009. Exploration geophysics. Springer.
Harris, R., Tréhu, A., Henrys, S.A., Gormam, A.R., Lauer, R., Phrampus, B., Colella, H., Baker, D., Rocco, N., Ellet, L., Turnbull, J., Hearn, J.O., Haase, P., 2015a. Cruise Report , STINGS Expedition R / V Roger Revelle , RR1508 , 16 May The Thermal Regime of the Hikurangi Subduction Zone and Shallow Slow Slip Events , New Zealand Scientific Participants.
Harris, R., Tréhu, A., Henrys, S.A., Gormam, A.R., Lauer, R., Phrampus, B., Colella, H., Baker, D., Rocco, N., Ellet, L., Turnbull, J., Hearn, J.O., Haase, P., 2015b. Appendix from Cruise Report , STINGS Expedition R / V Roger Revelle , RR1508 , 16 May The Thermal Regime of the Hikurangi Subduction Zone and Shallow Slow Slip Events.
Harrison, S., 2010. Natural Gas Hydrates.
Herron, D.A., Latimer, R.B., 2011. First steps in seismic interpretation. Society of Exploration Geophysicists.
Hunt, J., 1979. Petroleum Geochemistry and Geology.
Hyndman, R.D., Spence, G.D., 1992. A Seismic Study of Methane Hydrate Marine Bottom Simulating Reflectors. J. Geophys. Res. 97, 6683–6698.
Ikelle, L. (Luc), Amundsen, L., 2005. Introduction to Petroleum Seismology. Society of Exploration Geophysicists.
Jovanovich, D.B., Sumner, R.D., Akins-Easterlin, S.L., 1983. Ghosting and Marine Signature Deconvolution: A Prerequisite for Detailed Seismic Interpretation. Geophysics 48, 1468–1485.
Klauda, J.B., Sandler, S.I., 2005. Global Distribution of Methane Hydrate in Ocean Sediment. Energy and Fuels 19, 459–470. doi:10.1021/ef049798o
Knapp, R.W., Anderson, N.L., 1995. Comparison of High-resolution and Conventional-resolution Seismic Data- Applied to Cyclothems. Kansas Geol. Surv. 237, 39–42.
Konno, Y., Fujii, T., Sato, A., Akamine, K., Naiki, M., Masuda, Y., Yamamoto, K., Nagao, J., 2017. Key Findings of the World's First Offshore Methane Hydrate Production Test off the Coast of Japan: Toward Future Commercial Production. Energy & Fuels 31, 2607–2616. doi:10.1021/acs.energyfuels.6b03143
Kroeger, K.F., Plaza-Faverola, A., Barnes, P.M., Pecher, I.A., 2015. Thermal evolution of the New Zealand Hikurangi subduction margin: Impact on natural gas generation and

methane hydrate formation e A model study. Mar. Pet. Geol. 63, 97–114. doi:10.1016/j.marpetgeo.2015.01.020
Kvenvolden, K., 1993. Gas Hydrates - Geological Perspective and Global Change. Am. Geophys. Union 31, 173–187.
Lewis, K., Pantin, H., 2002. Channel-axis, Overbank and Drift Sediment Waves in the Southern Hikurangi Trough, New Zealand. Mar. Geol. 192, 123–151.
Ligtenberg, J.H., 2005. Detection of fluid migration pathways in seismic data: implications for fault seal analysis. Basin Res. 17, 141–153. doi:10.1111/j.1365-2117.2005.00258.x
Lin, W., 2011. Thermal conductivities under high pressure in core samples from IODP NanTroSEIZE drilling site C0001 12, 1–12. doi:10.1029/2010GC003449
Litchfield, N.J., Cox, S.C., Villamor, P., Nodder, S., Little, T., Van, R., Norris, D.R., Berryman, K., Lamarche, G., Pondard, N., Sutherland, R., Beavan, R.J., Stirling, M., Barrell, D.J.A., Mountjoy, J.J., Barnes, P.M., Langridge, R., Nicol, A., Pettinga, J.R., Clark, K., 2013. A model of active faulting in New Zealand: fault zone parameter descriptions.
Liu, C.S., Schnürle, P., Wang, Y., Chung, S.H., Chen, S.C., Hsiuan, T.H., 2006. Distribution and characters of gas hydrate offshore of southwestern Taiwan. Terr. Atmos. Ocean. Sci. 17, 615–644.
Lockmuller, N., Redgrove, Jo., Kubicar, L., 2004. Measurement of Thermal Conductivity with the Needle Probe. High Temp. - High Press. 35, 127–138. doi:10.1068/htjr099
Masters, G., Constable, S., 2017. Chapter 3: Heat Flow and Energetics of Earth [WWW Document]. Scripps Inst. Oceanogr. URL https://igppweb.ucsd.edu/~guy/sio103/classinfo.pdf (accessed 9.4.17).
Mavko, G., 2005. Basic Geophysical Concepts.
Milkov, A. V., Dickens, G.R., Claypool, G.E., Lee, Y.-J., Borowski, W.S., Torres, M.E., Xu, W., Tomaru, H., Tréhu, A.M., Schultheiss, P., 2004. Co-existence of gas hydrate, free gas, and brine within the regional gas hydrate stability zone at Hydrate Ridge (Oregon margin): evidence from prolonged degassing of a pressurized core. Earth Planet. Sci. Lett. 222, 829–843. doi:10.1016/j.epsl.2004.03.028
Morton-Thompson, D., Woods, A.M., 1993. Development Geology Reference Manual. AAPG.
Nanda, N.C., 2016. Seismic Reflection Principles: Basics, in: Seismic Data Interpretation and Evaluation for Hydrocarbon Exploration and Production: A Practitioner's Guide. p. 224. doi:10.1007/978-3-319-26491-2
Parkes, G., Hatton, L., 1986. The Marine Seismic Source. D. Reidel.
Physics Class Room, 2016. Pitch and Frequency [WWW Document]. URL http://www.physicsclassroom.com/class/sound/Lesson-2/Pitch-and-Frequency (accessed 8.3.17).
Pollack, H.N., Hurter, S.J., Johnson, R., 1993. Heat flow from the earth´s interior: analysis of the global data set. Rev. Geophys. 31, 267–280. doi:10.1029/93RG01249
Priyanto, B., Hokstad, K., Zwach, C., Schaack, M. Van, Mjøs, R., Hartadi, E.T., Tasarova, Z.A., Duffaut, K., 2015. Heat Flow Estimation from BSR: An Example from the Aru Region, Offshore West Papua, Eastern Indonesia.
Ravens, J., 1995. Globe Claritas. Seismic Processing Software Manual.
Riedel, M., Willoighby, E., Chopra, S., 2010. Gas Hydrates - Geophysical Exploration Techniques and Methods, in: Geophysical Characterization of Gas Hyrdates. pp. 1–21.
Roberto R. Cardoso and Valiya M. Hamza, 2011. Finite Half-Space Model of the Oceanic Lithosphere. Earth Sci. 5.
RPS Energy Pty Ltd, 2010. Petroleum Report Series PR4158.
Sain, K., 2011. Energy Partitioning of Seismic Waves. Springer Netherlands, pp. 291–294.

doi:10.1007/978-90-481-8702-7_59
Sass, J.H., Beardsmore, G., 2011. Heat Flow Measurements, Continental. Springer Netherlands, pp. 569–573. doi:10.1007/978-90-481-8702-7_72
Scales, J.A., 2017. Theory of Seismic Imaging Theory of Seismic Imaging.
Schultz, P., 1998. The Seismic Velocity Model as an Interpretation Asset. Society of Exploration Geophysicists.
Sclater, J.G., Jaupart, C., Galson, D., 1980. The Heat Flow Through Oceanic and Continetal Crust and the Heat Loss of the Earth. Rev. Geophys. Sp. Phys. 18, 269–311.
Sloan, D., 2003. Fundamental Principles and Applications of Natural Gas Hydrates. Nature 426, 353–359.
Soufi, N., 2009. Pressure Measurements in shale Methods. Norwegian University of Science and Technology.
Stein, C.A., 1995. Heat Flow of the Earth. Glob. Earth Phys. – A Handb. Phys. Constants, AGU Ref. Shelf 1 144–158. doi:10.1112/S0024609301008396
Systems, W.S.P., 2016. WHSC Seismic Profiling systems [WWW Document]. USGS. URL https://woodshole.er.usgs.gov/operations/sfmapping/airgun.htm (accessed 7.25.17).
Tamunobereton-Ari, Ngeri, A.P., Amakiri, A.R.C., 2015. Time-Frequency Attenuation of Swell Noise on Seismic Data from Offshore Central Niger-Delta, Nigeria. IOSR J. Appl. Geol. Geophys. Ver. I 3, 2321–990. doi:10.9790/0990-03513035
Thakur, N.K., Rajput, S., 2011. Exploration of gas hydrates : geophysical techniques. Springer.
Townend, J., 1997. Estimates of conductive heat flow through bottom-simulating reflectors on the Hikurangi and southwest Fiordland continental margins, New Zealand. Mar. Geol. 141, 209–220. doi:10.1016/S0025-3227(97)00073-X
Trabant, P., 1942. Applied High-resolution Geophysical Methods: Offshore Geoengineering Hazards.
Tullos, F., Reid, A., 1969. Seismic Attenuation of Gulf Coast Sediments. Geophysics 34, 516–528.
Vedova, B. Della, Bellani, S., Pellis, G., Squarci, P., 2001. Deep temperatures and surface heat flow distribution, in: Anatomy of an Orogen: The Apennines and Adjacent Mediterranean Basins. Springer Netherlands, Dordrecht, pp. 65–76. doi:10.1007/978-94-015-9829-3_7
Widess, M.B., 1973. How Thin is a Thin Bed? GEOPHYSICS 38, 1176–1180. doi:10.1190/1.1440403
Wood, L., Treitel, S., 1975. Seismic Signal Processing. Proc. Inst. Electr. Electron. Eng. 63, 649–661.
XSGEO, 1999a. Seismic Processing [WWW Document]. URL http://www.xsgeo.com/course/proc.htm (accessed 8.3.16).
XSGEO, 1999b. Velocity Analysis in Practice [WWW Document]. Hess Corp. URL http://www.xsgeo.com/course/velan.htm (accessed 9.25.16).
Yilmaz, O., 2001. Seismic Data Analysis: Processing, Inversion, and Interpretation of Seismic Data, 1st ed, Society of Exploration Geophysicists. Society of Exploration Geophysicists, Tulsa. doi:10.1190/1.9781560801580.fm
Zeng, H., 2013. Frequency-dependent seismic-stratigraphic and facies interpretation. Am. Assoc. Pet. Geol. Bull. 97.

Appendix

Appendix contents
Paper Appendix
MATLAB Script for Estimating Geothermal Gradient from BSR Picks
Thermal Conductivity Extrapolation Script

Digital Appendix
-Globe Claritas Project
-Kingdom Project
-Heat Flow and Thermal Results

MATLAB Script for Estimating Geothermal Gradient from BSR Picks.

```
% Example Matlab script to estimate geothermal gradient from BSR picks

% Gareth Crutchley, June 2017
% Edited by Patrick Fletcher, August 2017

% Using:

% 1. A seismic section from Mountjoy et al. 2014 (doi:
10.1002/2014GC005379) as an example
%    (see Figure 1.png, in this directory)
% 2. Some seafloor and BSR picks from that seismic section (made at 1000 m
increments)
%    (see Figure 2.png and the file SF-BSR-picks.xlsx, in this directory)
% 3. A made up CTD file
%    (see Synthetic-CTD-data.xlsx, in this directory)
% 4. A made up TWT-Vp function for sub-seafloor sediments (in this
directory)
%    (see sub-seafloor-TWT-Vp-function.xlsx, in this directory)
% 5. CH4 hydrate phase boundary from Tishchenko et. al. 2005,
%    Chemical Geology, Volume 219, Issues 1ï¿½4, 37-52,
%    https://doi.org/10.1016/j.chemgeo.2005.02.008.
%    Also in Kossel et al. 2013:
%    The SUGAR Toolbox: a library of numerical algorithms and data for
%    modelling of gas hydrate systems and marine environments.

%%
```

```
clear all

%% Set some constants:

T = (273:0.1:293.5)'; % temperature range for calculating hydrate phase
boundary, K
S = 35; % practical salinity of seawater
rhow = 1035; % desnity of seawater (kg m-3)
Vw = 1500; % velocity of seawater (m s-1)
G = 9.80665; % gravitational acceleration (m s-2)
xinc = 1000; % distance increment between seafloor picks (m). Note: assumed
to be constant, and the same for BSR picks

%% Load seafloor and BSR picks, TWT-Vp function, CTD profile

picksfile                          =                          '\\student.hcs-
p01.otago.ac.nz\geology\UserShare\flepa752\Documents\MATLAB\line13Afullrun\
SF-BSR-picksline13A-all.xls';
SFpicks = xlsread(picksfile,1,'A2:B2927'); % define range of data cells
BSRpicks = xlsread(picksfile,2,'A2:B2927'); % define range of data cells
%sftempfile                        =                          '\\student.hcs-
p01.otago.ac.nz\geology\UserShare\flepa752\Documents\MATLAB\line10fullrun\l
ine10_seafloorlocations_with_temp.xls';
%sftemp = xlsread(sftempfile,1, 'A2:B2352');
BSRdepthfile                       =                          '\\student.hcs-
p01.otago.ac.nz\geology\UserShare\flepa752\Documents\MATLAB\Line13Afullrun\
BSRdepthbsf-line13A_all.xls';
BSRdepth = xlsread(BSRdepthfile,1, 'A2:B2927');

TWTVpfile = '/Matlab-for-Patrick/sub-seafloor-TWT-Vp-function.xlsx'; % Just
a made-up TWT-Vp function!
TWTVp = xlsread(TWTVpfile,1,'A2:B22'); % define range of data cells

CTDfile                            =                          '\\student.hcs-
p01.otago.ac.nz\geology\UserShare\flepa752\Documents\MATLAB\line11fullrun\t
emp_profile.xls'; % Just made up values!
CTDdata = xlsread(CTDfile,1,'A2:C979'); % define range of data cells

%% Calculate CH4 hydrate phase boundary, after Tishchenko et al. 2005 and
Kossel et al. 2013
```

```
lnPdissw = -1.6444866D3 - 0.1374178.*T + 5.4979866D4./T ...
    + 2.64118188D2.*log(T) + S.*1.005 .* (1.1178266D4 ...
    + 7.67420344.*T - 4.515213D-3.*T.^2 - 2.04872879D5./T ...
    - 2.17246046D3.*log(T)) + (S.*1.005).^2 .*(1.70484431D2 ...
    + 0.118594073.*T - 7.0581304D-5.*T.^2 ...
    - 3.09796169D3./T - 33.2031996.*log(T)) ;

pdissw = exp(lnPdissw); % [MPa]
pdissw_Pa = pdissw .* 1e6; % [Pa]
pghsw = pdissw_Pa ./ (rhow*G);% [m H2O]

% Optional plot:
plot(T,-pghsw,'.b');

%% Interpolate seafloor temperature from CTD data and seafloor picks

sfdepth = cat(2, SFpicks(:,1), (SFpicks(:,2))); %(./1000) .* (Vw/2)); %
Depth = (Vwater (m/s) * TWT(s)) / 2
sftemp = cat(2, SFpicks(:,1),
interp1(CTDdata(:,3),CTDdata(:,2),sfdepth(:,2))); % seafloor temperature, K

%% Estimate BSR depth, using TWT-Vp relationship

BSRrange = find(sfdepth(:,1)>=min(BSRpicks(:,1)) &
sfdepth(:,1)<=max(BSRpicks(:,1))); % find the range of seafloor picks for
which there are also BSR picks
%
% sfdepth_at_BSR = sfdepth(BSRrange,2);
% SF2BSRTWT = BSRpicks(:,2) - SFpicks(BSRrange,2);
% SF2BSRZ = zeros(size(SF2BSRTWT));
% for i = 1 : length(SF2BSRZ)
%     Vpmax = interp1(TWTVp(:,1),TWTVp(:,2),SF2BSRTWT(i,1));
%     VpAV = (Vw + Vpmax) / 2;
%     SF2BSRZ(i,1) = VpAV * SF2BSRTWT(i,1)/1000;
% end
% BSRdepth = cat(2, BSRpicks(:,1), sfdepth_at_BSR + SF2BSRZ); % Depth of
the BSR below sealevel
```

```
%% BSR pressure, assuming hydrostatic fluid pressure

BSRpress = rhow .* G .* BSRdepth(:,2); % Pressure at BSR, Pa
BSRpress = cat(2, BSRpicks(:,1), BSRpress);

%% BSR temperature, from phase boundary

BSRtemp = interp1(pdissw_Pa,T,BSRpress(:,2)); % Temperature at the BSR, K
BSRtemp = cat(2, BSRpicks(:,1), BSRtemp);

%% Compile results and write to text file
outdata = NaN(size(sfdepth,1),6); % Make a null matrix to fill with the
data (6 columns, for: <dist> <sfdepth> <sftemp> <BSRdepth> <BSRtemp>
<geotherm> )
outdata(:,1:2) = sfdepth;
outdata(:,3) = sftemp(:,2);
outdata(BSRrange,4) = BSRdepth(:,2);
outdata(BSRrange,5) = BSRtemp(:,2);
outdata(:,6) = 1000 .* ( outdata(:,5) - outdata(:,3) ) ./ ( outdata(:,4) -
outdata(:,2) ) ;

fid = fopen('line13A_all.txt','wt');
fprintf(fid,'<dist>\t<sfz>\t<sfT>\t<BSRz>\t<BSRT>\t<geotherm>\n');
fprintf(fid,'%0.2f\t%0.2f\t%0.2f\t%0.2f\t%0.2f\t%0.2f\n',outdata');
fclose(fid);
```

7.3 Thermal Conductivity Extrapolation Script

```
%% Script for rescale thermal conductivities on to parallel lines

 picksfile = 'D:\Personal Files\Fletcher\TCextrapolation\line10TC.xlsx';
Line10TC = xlsread(picksfile,1,'A2:B1412');
picksfile09 = 'D:\Personal
Files\Fletcher\TCextrapolation\matchedthermalconductivitiesboth.xlsx';
Line09TC = xlsread(picksfile09,4,'C2:D1333');
Line09 = xlsread(picksfile,2,'A2:A2139');
matchingcdps = 'D:\Personal
Files\Fletcher\TCextrapolation\matchingcdps.xlsx';
matchingcdps9 = xlsread(matchingcdps,1,'A2:B10');
line9therms = xlsread(matchingcdps,2,'A2:B10');
fullL9vL10cdpmatch = xlsread(matchingcdps,4,'A2:B1347');
fullL11vL10cdpmatch = xlsread(matchingcdps,4,'G2:H1347');
fullL12vL10cdpmatch = xlsread(matchingcdps,4,'L2:M1347');
fullL13vL10cdpmatch = xlsread(matchingcdps,4,'Q2:R1347');
```

```
Line11 = xlsread(picksfile,3,'A2:B2186');
%Line12 = xlsread(picksfile,4,'A2:B2334');

%Line9therm =  Line09(:,1);
%newTC = cat(2, Line09(:,1),
equivtherm = interp1(Line09TC(:,1),Line09TC(:,2),fullL9vL10cdpmatch(:,2));
line10therm = interp1(fullL9vL10cdpmatch(:,1), equivtherm(:,1), 747:2092);
line10therm = line10therm';


% outdata = NaN(size(newTC,1) ,2);
% %outdata(:,1:2) = Line10TC;
% outdata(:,1) = newTC(:,1);
% outdata(:,2) = newTC(:,2);
% fid = fopen('line09TC.txt','wt');
% fprintf(fid,'<cdp>\t<TC>\n');
```